**Title**
Scanning Tunneling Microscopy and the Atomic Structure of Solid Surfaces



**Authors**
Ogletree, F.
Salmeron, E.M.

**Publication Date**
1991

LBL-30979
Preprint

Center for Advanced Materials

# CAM

To be published as a chapter in *Progress in Solid State Chemistry,* Pergamon Press, Oxford, U.K., 1991

## Scanning Tunneling Microscopy and the Atomic Structure of Solid Surfaces

F. Ogletree and M. Salmeron

June 1991

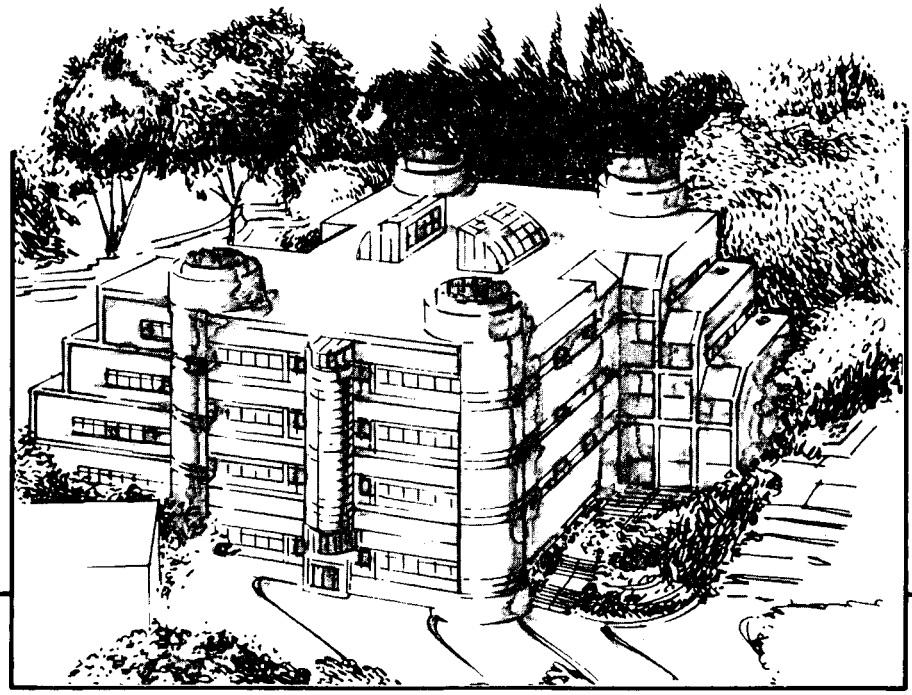

**Materials and Chemical Sciences Division**

**Lawrence Berkeley Laboratory • University of California**

ONE CYCLOTRON ROAD, BERKELEY, CA 94720 • (415) 486-4755

Prepared for the U.S. Department of Energy under Contract DE-AC03-76SF00098

## DISCLAIMER

LBL-30979

# Scanning Tunneling Microscopy and the Atomic Structure of Solid Surfaces

*Frank Ogletree and Miquel Salmeron*

Materials Sciences Division
Center for Advanced Materials
Lawrence Berkeley Laboratory
University of California
Berkeley, CA 94720 U.S.A.

June 25, 1991

ACKNOWLEDGMENT
This work was supported by the Director, Office of Energy Research, Office of Basic Energy Sciences, Material Sciences Division, U.S. Department of Energy under contract No. DE-AC03--76SF00098.

# Scanning Tunneling Microscopy and the Atomic Structure of Solid Surfaces

*Frank Ogletree and Miquel Salmeron*

Center for Advanced Materials
Materials Sciences Division
Lawrence Berkeley Laboratory
1 Cyclotron Road
Berkeley, California 94720

*ABSTRACT*

Experimental scanning tunneling microscopy studies of atomically resolved surface geometry and electronic structure are reviewed for metals, semi-conductors and layered compounds. STM theory as it relates to image interpretation is reviewed. STM techniques and instrumentation are discussed, including performance and noise considerations.

June 25, 1991

# Table of Contents

# Scanning Tunneling Microscopy and the Atomic Structure of Solid Surfaces

*Frank Ogletree and Miquel Salmeron*

Center for Advanced Materials
Materials Sciences Division
Lawrence Berkeley Laboratory
1 Cyclotron Road
Berkeley, California 94720

## 1. INTRODUCTION

Since its introduction by Binnig and Rohrer in 1981-82[1] scanning tunneling microscopy (STM) has become widely adopted and adapted. The STM of Binnig and Rohrer had its predecessor in the Topografiner of R. D. Young.[2] The basic idea is to bring a very sharp tip at close proximity to the surface in such a way that tunneling of electrons through the vacuum gap or field emission takes place. Once this is achieved, the tip is rastered over the surface at constant height by means of piezoelectric transducers, as shown schematically in figure 1. Today STM techniques are used in hundreds of laboratories worldwide to study a wide range of problems, including the atomic structure of surfaces, chemisorption, epitaxy, solid-liquid interfaces, biological molecules, liquid crystals, surface magnetism, superconductivity, and atomic scale mechanical properties.

Tunneling microscopy has come a long way in the last eight or nine years. STM results have led to significant progress in many areas of surface science, including some problems that other available techniques can study only indirectly, if at all. The spatial distribution of surface states within the unit cell and the shape of electronic orbitals have been measured. Great strides have been made in understanding the reconstruction of semiconductor surfaces. The local structure of some atomic steps have been imaged. Nucleation sites for chemical reactions and the mechanisms of epitaxial growth have been observed directly. Surface point defects and atomic diffusion have been studied.

In this paper we will review the use of the STM to study the atomic-level structure of solid surfaces. Our focus will be on experimental results. We will briefly discuss the

theory of STM imaging, STM instrumentation and experimental problems. STM results that are not directly related to atomic-scale structure, such as superconductivity studies and most biological results, are outside the scope of this review.

Several reviews of the STM literature have been published, including those of Golovchenko,[3] Hansma and Tersoff,[4] Binnig and Rohrer[5] and Demuth *et al.*,[6] but new results are appearing at an accelerating pace. There are now a large number of experienced STM groups and increasingly reliable commercial STM equipment has become available. For the last few years the focus of STM work has been on problem solving rather than on developing the techniques of STM. Today we are seeing the fruits of these efforts.

We will concentrate on STM results, since most other scanning probe microscopes do not have sufficient resolution to study atomic structure. The atomic force microscope[7] (AFM) certainly has this potential, and atomic resolution images have been obtained on graphite,[7] boron nitride,[8] mica[9] and other substrates.[10] However, most of these initial AFM studies have been demonstrations of the concept, and few real atomic structure problems have been solved to date. We expect that this situation will change rapidly over the next few years.

In the body of this review we will describe some results on STM theory, discuss STM contrast mechanisms and spectroscopic techniques, and a few points on instrumentation and tip effects. Tip-surface interactions and their effect upon STM imaging will be discussed in more depth. We will then survey STM results on the widely studied and somewhat peculiar graphite surface, including adsorbates on graphite. Semiconductor surfaces will be reviewed next, including reconstructed, epitaxial and adsorbate covered surfaces. Finally we will discuss metal surfaces, both clean and with chemisorbed overlayers.

## 2. STM THEORY

Tunneling[11] and tunneling spectroscopy[12] have long been familiar in solid state physics. Although vacuum tunneling was described in the early days of quantum mechanics, the difficulty of maintaining a vacuum gap delayed its observation until the work of Young *et al.* in the late 1960's.[2]

A realistic theoretical description of STM imaging is extraordinarily complicated. It is only within the last decade or so that theorists have been able to carry out sufficiently accurate total energy calculations to make useful predictions of ordered surface structures and reconstructions. Surface features with reduced symmetry such as steps and point defects are even more complicated. In the case of tunneling microscopy two surfaces are involved, including a tip that is often poorly characterized, with no symmetry to simplify the problem. Furthermore, tunnel currents depend on the overlap and interaction of tip and sample electronic wave functions, and it is generally more difficult to calculate accurate wave functions than accurate total energies. Finally, under some conditions the tip and surface interact strongly, and must be treated as one system rather than separate weakly coupled systems.

In many cases a qualitative understanding of surface structures can be obtained by inspection of STM images. Sulfur atoms adsorbed on metal surfaces, for example, appear as "bumps" in STM images, and can be directly interpreted in terms of adsorption geometry. Although electronic structure plays a greater role, STM images of aluminum or indium atoms adsorbed on Si(111) at low coverages can also be understood as geometric images. However, while "bumps" also appear for boron adsorption, theoretical calculations showed these features were due to sub-surface boron atoms directly under surface silicon atoms. In the case of silver adsorbed on silicon, even after several studies there is no general agreement on the interpretation of STM image features. Likewise for higher coverages of indium on Si(111), clear periodic STM images have been obtained but no one has come up with a structural model to explain the STM images. *Qualitative* interpretation of STM images can be a significant help in understanding surface atomic structure, but it should be done with caution, and in the context of all

available theoretical and other experimental information.

Even with a full STM theory and a completely characterized tip it would not in general be possible to determine the *quantitative* surface geometry in terms of exact atomic coordinates and bond lengths by working back from a series of STM images. Subsurface structure and bonding modify the surface electronic structure and therefore the STM images, but STM gives no direct information on the subsurface structure or registry. With the best STM theory, the structure problem would be similar to that of electron diffraction (LEED) or ion scattering (MEIS), where experimental data is compared to theoretical simulations of the experiment for a series of reasonable model structures. Each structure is optimized to give the best fit between the simulated data and the experimental data. If the match with the best structure is sufficiently close, the structure is considered "solved".

With an appreciation of the difficulties involved, we will now discuss some of the theoretical results that have been obtained for STM imaging.

### 2.1. Square well tunneling

The simplest model for the tunneling microscope is the scattering of plane waves by a one dimensional barrier. The transmission for a plane wave of energy $E$ through a square barrier of width $d$ and height $\phi > E$ is[13]

$$T = \frac{4E(\phi - E)}{4E(\phi - E) + \phi^2 \sinh^2[\frac{d}{\hbar}\sqrt{2m(\phi - E)}]} \tag{1}$$

In the limit of $E << \phi$ where $T$ is small this reduces to

$$T = \frac{E}{\phi}\, e^{-2d\sqrt{2m\phi}/\hbar} \approx e^{-Ad\sqrt{\phi}} \tag{2}$$

With $d$ in angstroms and $\phi$ in electron-volts $A = 1.025$ so the barrier transmission $T \approx e^{-d\sqrt{\phi}}$

STM tunneling takes place between a sharp tip and a conductive surface. The tip and sample may have different work functions, and the sample is biased at a voltage $V$ relative to the tip (figure 2). Now tunneling takes place through a trapezoidal barrier. It can be shown that the barrier height $\phi$ in the tunneling probability $T$ can be replaced by the average barrier height[14] given by

$$\bar{\phi} = \tfrac{1}{2}[\phi_{tip} + \phi_{sample} - |eV|] \tag{3}$$

where $V$ is the bias voltage, assuming $eV < \phi_{sample}, \phi_{tip}$. At large bias voltages the expression for tunneling must be replaced by a modified expression allowing for field emission.

The above expressions (Eq. 1-3) describe tunneling through a one dimensional barrier. A formal expression for the tunneling current can be written by assuming weak coupling between the two surfaces

$$I = \frac{2\pi e}{\hbar} \int_{\mu,\nu} d\mathbf{k}_\mu d\mathbf{k}_\nu \, \rho_{tip}(\mathbf{k}_\mu) \, \rho_{sample}(\mathbf{k}_\nu) \, [f(E_\mu) - f(E_\nu + eV)] |M_{\mu\nu}|^2 \, \delta(E_\mu - E_\nu) \tag{4}$$

where $\rho(\mathbf{k})$ is the density of states, $f(E)$ is the Fermi function and $M_{\mu\nu}$ is the matrix element linking tip and sample states.

The Fermi function $f(E)$ terms insure that electrons will tunnel from occupied states to empty states. To date most STM experiments have been done at or below room temperature. The Fermi function is constant, either 1 or 0, except for a small range $\sim 2k_BT$ or $\sim 0.05$ eV around $E_F$. Since the surface density of states does not vary significantly over this energy range the Fermi function term just defines the limits of the integral over states to those between $E_F$ and $E_F - eV_{bias}$.

The square of the matrix element $|M_{\mu\nu}|^2$ corresponds to the tunneling probability through the tip-sample barrier. A first approximation for the matrix element $M_{\mu\nu}$ can be made using the expression for the transmission through a one dimensional barrier in Eq. 1. For the case of three dimensional tunneling of a state with energy $E$ the average barrier height $\bar{\phi}$ is replaced by $[\bar{\phi} - (E - E_F) + \frac{\hbar^2 k_\parallel^2}{2m}]$. The term including $k_\parallel$ means

that electrons with momentum **k** perpendicular to the gap will have the highest transmission probability, while those moving across the tunneling gap at an angle will cross a wider "effective" gap and will have a reduced tunneling probability.

The tip is usually not well characterized in STM. For the purpose of this first approximation the density of tip states can be assumed constant and featureless. With these assumptions the tunnel current is proportional to

$$\int_{E_F-eV}^{E_F} d\mathbf{k}\ \rho_{sample}(\mathbf{k},E) e^{-d[\bar{\phi} - (E - E_F) + \frac{\hbar^2 k_{\parallel}^2}{2m}]^{1/2}} \tag{5}$$

The term in the exponential can be rewritten as $e^{-2\kappa d}$ where $\kappa$ is the inverse decay length of the wave functions in the gap.

For tunneling to metal surfaces at small bias voltages the current is proportional to $Ve^{-d\bar{\phi}^{1/2}}$. It is the exponential dependence of $I$ on the distance $d$ that is responsible for the high vertical resolution of the STM. For example, with a work function of 4 eV, $\kappa \sim 1$ Å$^{-1}$ and a change in $d$ of 1 Å changes $I$ by an order of magnitude.

For semiconductors the situation may be more complex. In the case of Si(100) which has a surface band gap, the band minimum of the surface Brillouin zone is near the $\overline{K}$ point with a large $k_{\parallel}$ component. Stroscio *et al.*[15] observed a voltage-dependent change in the inverse decay length $\kappa$. As the bias voltage increased, states with smaller $k_{\parallel}$ were able to contribute to the tunnel current causing a decrease in $\kappa$.

The above theory is a useful guide to designing and operating microscopes, but it cannot answer any of the interesting questions, such as what are the fundamental limits of STM resolution, or how surface atomic structure, ordering, steps, and defects will influence images, or can different types of atoms be distinguished in STM images. A better theory is required to tackle these questions.

## 2.2. The s-wave tip

To get more realistic results an STM theory must explicitly take into account the electronic structure of both the tip and the substrate. The filled density of states for the negative electrode and the empty density of states for the positive electrode are directly involved in the tunneling process. This is a fundamental aspect of the operation of the STM that determines the nature and the meaning of the images obtained. Tersoff and Hamann[16,17] approach this problem by considering an "ideal" tip represented by a $\delta$-function $\delta(\mathbf{r}_o)$ at a small bias voltage. Putting this "tip" in the perturbation expression of Eq. 4 above gives a tunnel current proportional to

$$\sum_{\nu} |\psi_\nu(\mathbf{r}_o)|^2 \, \delta(E_\nu - E_F) \equiv \rho(\mathbf{r}_o, E_F) \tag{6}$$

where the $\psi_\nu$ are states of the surface. This expression is equivalent to the total charge density at $\mathbf{r}_o$ contributed by the states near the Fermi energy that take part in tunneling. This sum can be defined as $\rho(\mathbf{r},E_F)$, the "local density of states at the Fermi energy".

Using the $\delta$-function tip as a guide, Tersoff and Hamann then consider the next simplest tip model, a locally spherical tip of radius $R$ described by a spherically symmetric $s$-wave function. The matrix element linking tip and sample states is evaluated using Bardeen's theory for metal-insulator-metal tunnel junctions. Bardeen showed that when a region exists between the interacting conductors where the potentials vanish, then the matrix element can be calculated by integrating a "current-like" operator over any surface between the conductors,

$$M_{\mu\nu} = \frac{\hbar^2}{2m} \int d\mathbf{S} \cdot (\psi_\mu^* \nabla \psi_\nu - \psi_\nu \nabla \psi_\mu^*) \tag{7}$$

Given the assumption that the tip can be represented by an $s$-wave function Tersoff and Hamann show that the tunneling current depends only on the local density of states evaluated at the center of curvature $\mathbf{r}_o$ of the tip. The current is then

$$I = (32\pi^3 e^2/\hbar)(V\phi^2 \rho_{tip}(E_F) R^2/\kappa^4) \, e^{2\kappa R} \, \rho(\mathbf{r}_o, E_F) \tag{8}$$

Choosing reasonable physical parameters for a metallic tip, Tersoff and Hamman arrive at an expression for the tunneling gap conductivity $\sigma$ in $\Omega^{-1}$

$$\sigma \approx 0.4 R^2 e^{2\kappa R} \rho(\mathbf{r}_o, E_F) \tag{9}$$

where $\kappa$ is the inverse decay length of Eq. 5, distances are in Å and $\rho$ in $eV^{-1}$. As a result of the assumption of an $s$-wave tip, the surface states enter only through the local density of states evaluated at the center of the spherical tip, just as in the $\delta$ function case.

With the results of Eqs. 7 and 8 a number of useful calculations can be made. In particular the ability of the STM to resolve periodic surface structures can be estimated. The density of states at the Fermi energy has the same period as the lattice, so $\rho$ can be expanded in terms of Bloch functions at the surface,

$$\rho(\mathbf{r}_o, E_F) = \sum_{\mathbf{G}} \rho_{\mathbf{G}}(z) e^{i\mathbf{G}\cdot\mathbf{r}_o} \tag{10}$$

where the $\{\mathbf{G}\}$ are surface lattice vectors. Away from the surface

$$\rho_{\mathbf{G}}(z) = \rho_{\mathbf{G}} e^{-2z\sqrt{\kappa^2 + \mathbf{G}^2}} \tag{11}$$

Terms with large values of $\mathbf{G}$ are attenuated much faster than the $\mathbf{G} = 0$ term so as the gap $d$ increases the STM images become smoother and details are lost. A surface corrugation described by $\mathbf{G}$ will be attenuated as

$$\Delta_{\mathbf{G}} = \Delta_o e^{-2[(\mathbf{G}^2 + \kappa^2)^{1/2} - \kappa](R + d)} \tag{12}$$

in the limit of large gap widths $d$, where $\Delta_o$ is the corrugation in the plane of the surface and $R$ is the tip radius.

Eq. 12 predicts the limits of resolution for the STM. Even with a single atom tip $R + d$ cannot be reduced below $\sim$ 4 Å since metallic bonds are $\sim$ 2.5 to 3 Å. With present instruments it is quite difficult to resolve corrugations in STM images below $\sim$ 0.01 Å. The corrugation in the total density of states in the surface plane can be estimated to be $\leq 0.5$ Å from a hard-sphere model of the surface. For a surface feature with period $a$, $\mathbf{G} \sim 2\pi/a$ so for $\kappa \sim 1$ Å$^{-1}$ any corrugation with a period less than $\sim$ 6 Å will be attenuated by a factor of at least 50. This places a rough limit of 6 Å on the scale of features that can be resolved with the STM in the absence of electronic effects that enhance resolution. Experimental STM images of metals, semiconductors, and layered compounds have resolved surface corrugations and atomic features with sizes as

small as 1.5-2.5 Å, showing a basic disagreement with the predictions of the *s*-wave theory.

Tersoff points out special cases where smaller distances can be clearly resolved even at relatively large tunneling gaps due to electronic effects.[18,19] Graphite is a primary example. The surface band structure of graphite at the Fermi energy collapses to just one point at the corner of the surface Brillouin zone. This means that at small bias voltages the STM image is dominated by a single electronic state, or more precisely by a set of states of the same $|\mathbf{G}|$ related by symmetry. In the normal case states with $|\mathbf{G}| \neq 0$ are attenuated more quickly than the states with $\mathbf{G} = 0$, so the STM image becomes more uniform with increasing gap widths. In the case of graphite, all states contributing to the density of states at $E_F$ have the same $k_{||}$ so there is no loss of resolution with distance even though the period of the graphite unit cell is only 2.46 Å. Tersoff describes this type of STM experiment as imaging a single state, and gives other examples such as the charge density waves observed by STM on transition metal di-chalcogenides like $TaS_2$.

Tersoff and Hamann's theory can also be used to simulate images. For periodic surfaces with unit cells that are not too large, the local density of states at $E_F$, or even a voltage-dependent local density of states $\rho(\mathbf{r},E_F - eV)$ can be calculated explicitly. They make such a calculation for the reconstructed gold (110) surface[16,17] studied by Binnig *et al.*[1] and get reasonable agreement with the STM data.

Finally, Tersoff and Hamann suggest an approximation for the local density of states where calculations are not practical because of complicated or disordered surfaces. At least for metals, the local density of states at the Fermi energy is quite similar to the local charge density from all states. This approximation cannot be expected to work for semiconductor surfaces since the STM images of these surfaces are dominated by the surface electronic structure, but it is useful for metal surfaces.

### 2.3. Jellium theories

Norton Lang has taken a different approach to create a more realistic STM theory. He has concentrated on understanding chemisorption problems, such as the dependence of STM images on the identity of the tip and surface atoms, gap widths and bias voltages. In order to get a model simple enough to calculate numerical results, Lang models the surface as a single atom adsorbed on a jellium surface. Likewise, his tip is an atom on a second jellium surface. The tip wave function is not restricted to *s*-states.

The jellium approximation leaves out any details due to lattice structure, but it is realistic in modeling the interaction of the atom with the surface. Atomic states are broadened into resonances by interactions with the surface electron states, charge transfer takes place between the atom and the surface, and the "adsorption bond length" and electronic structure of the atom above the surface is determined self-consistently.[20,21]

Lang first considered the tunneling current density between a metal surface with a single "tip" atom and another surface. Using the perturbation approach, wave functions are first calculated separately for the two surfaces, and the tunnel current is calculated from the overlap of the wave functions. Lang modified the Bardeen tunneling theory to calculate the current distribution, not just the total current, between the "tip" and "sample" surfaces.[22] When the metal surfaces where placed 8.5 Å apart, the current contribution from a sodium atom, which adsorbs $\sim$ 1.5 Å above the jellium surface, corresponds to $R_{gap} = 0.33$ GΩ, a physically reasonable value. When a cesium atom was substituted for the sodium atom the current increased by a factor of $\sim 4$. Cesium and sodium have the same surface-atom bond length, but the density of states at $E_F$ is about 4 times higher for cesium. Lang found that most of the current is due to states with $m = 0$ (angular momentum around the surface normal, the axis of cylindrical symmetry). The next step in the calculation was to model the "tip" by an atom on the jellium surface and the sample by a similar atom on the "sample" side.[23] By sliding the tip atom past the surface atom and adjusting the tip-surface spacing to maintain a constant current Lang obtained the shape of the STM images of different adsorbate atoms. In this model the STM image of an adsorbed sodium atom was found to be about four

times bigger than a sulfur atom, while a helium atom appears as a depression. These results clearly demonstrate the importance of electronic contributions to STM images.

For the case of the tip atom directly over the surface atom, where the symmetry simplifies the calculation, Lang determined the apparent height of the adsorbed atom as a function of tip-sample voltage $V$ for sulfur, sodium and also for molybdenum, a $d$-band transition metal.[23] Again, the height varies as the $m = 0$ density of states at $E_F + eV$ except that the Mo $4d$ derived states have almost no effect on the tunnel current, although the $5s$ derived states are clearly seen. Lang attributes this to the small orbital radius of the $d$ electrons compared to the $s$ electrons.

We have seen (Eq. 11) how the observed corrugation in STM images of periodic surfaces should drop off exponentially with increasing gap width. Lang points out that the $z$ dependence of the apparent height of an isolated adsorbate atom is quite different. For a single adatom the observed STM height $\Delta z$ will decay logarithmically with increasing gap width, as $\ln \kappa d$ where $\kappa$ is the inverse decay length.[23]

This same type of voltage-dependent calculation can be used to determine the $I$—$V$ spectrum for a tip over an adsorbate atom.[24] Lang shows that the quantity $\frac{V}{I}\frac{\partial I}{\partial V}$ does indeed resemble a superposition of the tip and surface local densities of $m = 0$ states, as Stroscio *et al.* predicted based on their experimental observations on the Si(111) (2x1) surface.[15] Lang also shows that peak positions in the density of states can be determined more accurately from normalized $\frac{V}{I}\frac{\partial I}{\partial V}$ data than from the $\frac{\partial I}{\partial V}$ curves alone.

One of Lang's more recent results is a calculation of the dependence of the barrier height $\phi$ on tip-sample separation.[25] This is a complex calculation since the interaction between the tip and surface wave functions can not be treated as a perturbation for small gaps. For this calculation Lang again modeled the tip as a jellium surface with an adsorbed atom, and the surface as a bare jelluim surface. He then treated the tip and sample as a single quantum system. The bond length of the tip atom was held constant as the tip approached the surface. Starting at a gap of about 6 Å the barrier started to

drop below the bulk work function and decreased approximately linearly with gap until $\sim 2.5$ Å where $\phi \sim 0$. Even a complete collapse of the tunneling barrier over a small radius will not give an unrestricted current flow. The uncertainty relation $\Delta x \Delta k \sim 1$ requires that an electron passing through a hole in the barrier of radius $r$ have a transverse momentum $k_{\parallel} \sim 1/r$, which acts as an effective barrier.[25]

### 2.4. Theory and structure

The theories described above are primarily concerned with simulating or describing the process of STM imaging, usually with simplified or model systems. While comparison of STM data with theoretical models has often been used to choose between different surface models for reconstruction or chemisorption,[26,27] to our knowledge there is only one case where a theoretical analysis of STM data has been used to directly determine the bond lengths and angles. This case is the analysis of GaAs(110) surface buckling performed by Feenstra, Stroscio, Tersoff and Fein.[28]

STM images of the GaAs(110) surface show a single maxima in each unit cell. Feenstra *et al.* used the STM to measure the lateral shift of this maxima between occupied and unoccupied state images of the surface. Theoretical calculations showed that the occupied state density should be localized near the As atoms while the unoccupied states were near the Ga atom. The (110) surface is believed to reconstruct by twisting the surface Ga-As bonds while conserving bond length, producing a buckled surface with As atoms buckled outward and Ga atoms buckled inward. Calculations of the density of states at different buckling angles gave different lateral positions for the dangling bonds. Comparison of the STM images with these calculations gave a buckling angle of $\sim 30\,^{\circ}$.

This analysis shows a novel approach to surface structure determination. The STM was used to measure the voltage dependent lateral shifts of maxima within the unit cell, a quantity that can be measured unambiguously. Theoretical modeling then related this result to vertical shifts of the Ga and As atoms, quantities that cannot be clearly measured with the STM due to the interaction of electronic and geometric structure and the effects of tip-surface forces.

Although the number of direct STM calculations is still quite small, there has been a strong interaction between the theory of surfaces and experimental STM work. Before the advent of the STM, most quantitative data on surface structure came from electron diffraction (LEED), with additional results from SEXAFS and related techniques, medium energy ion scattering, and high resolution TEM.[29] These techniques are all sensitive to the average positions of ion cores, so they provide data on equilibrium geometry but not on electronic structure or local order. Results on surface electronic structure were mainly from angle-resolved photoemission. The STM changed all this by providing direct information on the relation between geometry and electronic structure and on local order as well as equilibrium geometry. This rich source of new data has stimulated surface theory and provided quick and accurate checks of experimental predictions.[30]

## 2.5. Tip states and STM resolution

Tersoff and Hamann's *s*-wave theory puts clear limits on the power of the STM to resolve atomic features on surfaces (Eq. 11). There is now a substantial body of experimental results where atomic features of 2 to 4 Å spacing are clearly resolved, in contradiction to the predictions of Eq. 11. Examples include atomic resolution on close packed gold[31] and aluminum,[32] atomic adsorbates on metal surfaces such as hydrogen[33] and sulfur[34,35,36] and (1x1) structures on silicon (111).[37]

Chen[38,39] has analyzed these observations in detail, and explains atomic resolution in terms of the contributions of tip states with $l,m \neq 0$. Chen states his basic argument in terms of a "reciprocity principle" -- the STM image should be unaffected by an exchange of tip and sample states. High resolution has been obtained on many semiconductor surfaces because of surface dangling bonds. The local density of states for the Au(111) and Al(111) surfaces can be described as a superposition of atomic orbitals following Tersoff and Hamann,[17] so the experimentally observed resolution must be due to dangling bond orbitals on the tip.[38]

Chen has worked out the matrix elements for non-spherical tip states. He considers a parabolic tip, with a single atom at the apex coupled to the body of the tip. Working in cylindrical coordinates defined by the axis of the tip, he has obtained a general solution for the matrix element of an arbitrary surface state and tip states described in spherical or cylindrical functions.[40] He describes a tip wave function as

$$\chi = \sum_{l,m} \beta_{l,m} k_l(\kappa r)\ Y_{lm}(\theta,\phi) \tag{13}$$

where $k_l$ is a spherical modified Bessel function. He finds that the matrix element $M_{l,m}$ between a surface wave function $\psi_\nu$ and the tip wave function $lm$ term is proportional to

$$\frac{\hbar^2}{2m\kappa} \frac{\partial^l \psi_\nu(\mathbf{r}_o)}{\partial z^{l-|m|} \partial x_\pm^{|m|}} \tag{14}$$

with $x_\pm \equiv (x \pm iy)/2$ where the sign is given by the sign of $m$.

Chen's results show that the STM image will no longer be proportional to the local density of states at $E_F$ when tip states with $l,m \neq 0$ contribute to the tunneling current. He describes the results of Eq. 14 as the "derivative rule" for the matrix elements coupling the tip and sample wave functions.[40] This sensitivity not only to the density of states at the Fermi energy but also to its derivatives parallel and perpendicular to the surface allows for much higher spatial resolution than the $s$-wave theory.

Tip states with higher angular momentum quantum numbers will drop of faster with distance than $s$-wave components, so these terms are most important for small values of the tunneling gap. These are just the conditions where high resolution STM images have been acquired. Chen has used his theory to analyze the STM images of the Al(111) surface.[38] He assumes that the tip has a $d_{z^2}$ state since cluster calculations have found such states near $E_F$ for $W_4$ and $W_5$ clusters. The surface density of states can be modeled by a term with $k_{||} = 0$ describing the uniform charge background and a fundamental corrugation term with $k_{||} = 4\pi/3a$ where $a$ is the nearest neighbor distance on the Al(111) surface. From Eq. 11 the density of states outside the surface should go as

$$\rho(\mathbf{r}) \approx C_o e^{-2\kappa z} + C_1 e^{-2\kappa_1 z} \phi(k_{||} z) \tag{15}$$

where $\phi(k_{||} z)$ is a two dimensional superposition of cosine terms that equals unity at the

atomic positions and vanishes in three-fold hollow sites, and $\kappa_1 = [\kappa^2 + k_{\parallel}^2]^{1/2}$.

For a tip $d_{z^2}$ state the matrix element should be proportional to $|\partial^2\psi/\partial^2 z|_{z_o}$. The tunneling current $I(z)$ can be found from Eq. 15 as

$$\rho(\mathbf{r}) \approx C_o\kappa^4 e^{-2\kappa z} + C_1\kappa_1^4 e^{-2\kappa_1 z}\phi(k_{\parallel} z) \tag{16}$$

The observed STM image corrugation will then be similar to the $s$-wave corrugation given by Eq. 12 but enhanced by the factor $(\kappa_1/\kappa)^4$. For the Al(111) surface this is $(1.72/0.93)^4 = 11.7$ or an order of magnitude greater than predicted by the $s$-wave theory. The corrugation decays with distance as $e^{-2(\kappa_1-\kappa)z}$ in both models, so the $d_{z^2}$ tip corrugation will be the same as that measured by the $s$ tip 1.6 Å closer to the surface.

According to Chen's analysis atomic resolution on metal surfaces will be very sensitive to the tip condition. This is consistent with the results for aluminum (111) obtained by Wintterlin *et al.*.[32] They report atomic resolution at small gap distances only after applying voltage pulses to the tip. This high resolution is somewhat unstable, and there can be an abrupt loss of tip resolution. This is reasonable if atomic resolution depends on certain precise tip configurations.

### 2.6. Tip surface interactions

In most of the preceding discussions, we have always assumed the original model of tunneling through a vacuum gap. There are strong experimental indications however that in some instances, actual tip contact with the surface is taking place. As long as the repulsive forces during contact remain below the bond breaking values, the integrity of both tip and surface can be maintained, particularly if there is little chemical affinity between the atoms in the tip and those at the surface. For typical bond energies in the range of a few eV, these forces are $\sim 10^{-8}$ N. Contact forces below this value can thus result in elastic deformation of the tip or the surface. Atomic resolution can still be obtained if the area of contact is restricted to one or two atoms. Sharvin has described the relation of resistance to contact area for quantum contacts.[41,42] This resistance has a much smaller dependence on distance than in the tunneling case. The limiting value of the Sharvin resistance is $\sim \frac{e}{\hbar^2}$ or 13 kΩ.[43] Experimental values for STM tip contacts on

metals surfaces are close to this value.[44]

### 2.6.1. Theoretical calculations

Ciraci and Batra and collaborators have made a series of theoretical calculations of cases where tip-surface interactions have significant effects on STM imaging mechanisms. They performed tight-binding and pseudopotential calculations with the surface represented by one or more layers of graphite and the tip by a single carbon atom. The tip atom was repeated on a 2x2 lattice to allow for periodic boundary conditions.[45,46,47]

Based on their results the authors describe three different regimes of tip-sample interactions. At separations greater than $\sim$ 4 Å the tip and sample wave functions are not significantly changed, and the Bardeen weak-coupling formalism is a good description of the tunneling process. At distances less than $\sim$ 2 Å chemical bonds start to form and the conduction mechanism shifts from tunneling to conduction through point contacts. In the intermediate regime, the surface electronic states are strongly affected by the presence of the tip atom, $\mathbf{k}_{||}$ is no longer a good quantum number and the Bardeen approximation is no longer valid. The authors describe the effects on the STM contrast in terms of "tip induced localized states (TILS)". The nature of the TILS depend strongly on the position of the tip within the surface unit cell. At a tip-surface separation of 2 Å, for example, the TILS model predicts a five-fold increase in tunnel current over top sites and no change over hollow sites compared to the equivalent calculation for unperturbed tip and surface states.[46] The calculations also predict tip-sample forces $\sim 10^{-8}$ N, sufficient to significantly deform the surface structure [however these calculations assumed a rigid surface plane].

Later calculations by Ciraci *et al.*[48] treated interactions of one and four atom aluminum tips with the graphite surface plane. Self-consistent pseudopotential calculations were used to investigate the effect of tip-sample electronic interactions on STM and AFM contrast. The results were similar to the carbon atom tip case, modified by the stronger chemical iterations with a metallic tip. The authors concluded that the electronic interactions are the dominant factor in AFM contrast even for inert surfaces such

as graphite. The calculated tip-substrate bond energies were 0.33 eV at top sites and 0.61 eV at hollow sites.

### 2.6.2. Experimental observations

Tip-surface interactions manifest themselves experimentally in a very clear way for graphite, giving rise to a multitude of effects. Graphite was the first material where so called "giant corrugations" were reported. These appear as large vertical displacements of the tip as it scans over the surface unit cell. In some cases this corrugation has been observed to reach values of several tens of Angstroms. The expected corrugation due to the electronic charge density profile can be estimated to be a few tenths of an Å based on He scattering results.[49] Tersoff does point out that there is an electronic component to these large corrugations (due to the singularity in the conductance in the center of the hexagon),[18] however it has become increasingly clear that elastic deformations of the tip and surface play a dominant role. Soler *et al.* proposed local elastic displacements of the surface atoms, to explain these corrugations[50] Later, Pethica proposed a large area of "contact" between tip and surface that would distribute the force and prevent the induced strains from exceeding the lattice maxima and produce inelastic effects.[51] Lateral resolution would be preserved by the periodic registry between two layers of graphite, one as a small flake attached to the tip and the other of course being the surface. An additional factor, again peculiar to graphite, is the fact that the electronic states contributing the tunneling electrons have all large values of their momentum parallel to the surface, $k_{||} = 2\pi/a$. The effect of this is to decrease the decay length, as shown in Eq. 5 above. The equivalent barrier height is 12 eV for a work function value of 4 eV. This forces the tip to be closer to the surface than for most other materials with $k_{||} = 0$ states near the Fermi level.

The force exerted by a W tip on graphite under typical conditions for tunneling experiments has been directly measured by Yamada *et al.*,[52] and Mate *et al.*[53] using an Atomic Force Microscope. By measuring the tunnel current between tip and surface simultaneously with the force, they showed that at tunneling currents of 1 to 10 nA and several tens of mV bias, compressive forces in the range of $10^{-6}$ to $10^{-7}$ N are generated, implying a relatively large tip-surface contact area.

Non-destructive tip-surface contacts can (and are likely to) occur whenever the formation of strong chemical bonds between the tip and the surface is prevented. Under these conditions, the integrity of the tip and surface can be maintained while the tip scans, provided that the forces exerted do not exceed the elastic limit of the materials. The chemical inertness of graphite, and the high probability that the outermost tip atoms are chemisorbed impurities that passivate its surface, at least in non-UHV environments, explains why the tip does not adhere to the graphite surface. Mamin *et al.* have shown how a layer of contamination between tip and surface can mediate the transmission of the deformation force, by performing experiments in air and in UHV with increasingly cleaner tips and samples.[54] As we will see below, another consequence of the existence of tip- surface forces and the resulting elastic deformations, is the observation of very low tunneling barrier heights.

Another manifestation of compressive tip-surface forces is the appearance of shear or frictional forces strong enough to cause horizontal displacement of adsorbed material. In figure 3 we show an example of these horizontal force components. The small flake of graphite in the right hand side of the image (a) is displaced as a result of scanning the tip to the left as shown in the next image (b). Figure 4 shows the highly distorted graphite unit cell that was obtained when the tip imaged the center part of a small (200 Å) flake of graphite. The tip drags the flake as it scans. The different distortion observed in the $x$ and $y$ directions indicates that frictional forces depend on the sliding direction of the flake relative to the basal plane. A more extended discussion of the experimental effects of tip-surface interactions in STM images can be found in recent papers by the authors.[55]

## 3. STM TECHNIQUE

In principle the STM can be used to determine the tunneling current in the neighborhood of a surface as a function of position and bias, $I(x,y,z,V)$. This tunnel current signal contains information on geometric and electronic structure of the surface, influenced to some degree by the geometry and electronic structure of the tunneling tip. In most experiments a subset of this data is collected to form an image of a surface $C(x,y)$ where $C$ is some contrast signal.

### 3.1. STM imaging and contrast

STM images can be generated in a number of ways. The most common mode is the constant current, also called "constant height" or topographic mode. Images of the changing tunneling current, local barrier height and conductance are also used. More exotic imaging techniques have been used in special cases, such as conductance parameter imaging on superconducting surfaces,[56] zero bias "gap noise" imaging,[57] or imaging using the photons emitted as "hot" tunneling electrons come to equilibrium.[58]

#### 3.1.1. Constant current images

The original and most common STM imaging mode is to adjust the feedback loop to maintain a constant tunneling current $I_o$ at a fixed bias $V$ during an $xy$ scan. The contrast signal is just the tip $z$ position, proportional to the voltage driving the $z$ piezo. The image $z(x,y)$ at constant $V$, $I_o$ is called a "constant current" or sometimes "topographic" image.

In the limit of a small, spherical tip not too close to the surface, Tersoff and Hamann[17] predict the constant current surface $z(x,y)|_{V,I_o}$ will correspond to a contour of the local density of states at the Fermi energy $\rho(\mathbf{r},E_F)$. Tersoff and Hamann have proposed approximating the density of states at the Fermi energy by scaling the total charge density $\rho(\mathbf{r})$. For the purposes of quick and rough calculation of an STM image, the charge density can be estimated as the superposition of the individual spherical charge distributions of the free atoms $\rho(\mathbf{r}) = \sum_i \phi_i(\mathbf{r}-\mathbf{r}_i)$.[17] For a metal surface with a fairly constant density of states in the vicinity of the Fermi energy and non-directional bonds, this approximation predicts that an STM constant height image will correspond to a smoothed representation of the surface topography, and that the image will be mostly unaffected by changes in the tip-sample bias voltage. The width of the tunneling gap will be proportional to the log of the gap resistance $R_{gap} = V/I_o$. Imaging at smaller gap resistances brings the tip closer to the surface which will increase resolution.

The interpretation of constant current images is much more complex for semiconductor surfaces. The bulk density of states changes substantially in the vicinity of the Fermi energy, and localized surface states may make a significant contribution to the tunneling current. Strong directional covalent semiconductor bonds make the approximation of a spherical atomic charge density $\phi(\mathbf{r}_i)$ unrealistic.

The well known silicon (111) (7x7) reconstruction is an obvious example of the problems of interpreting constant height images. With a positive sample bias electrons tunnel into empty surface states, and the faulted half of the unit cell appears $\sim 0.2$ Å lower that the unfaulted half, while an image of the filled surface states taken with negative bias has an apparently symmetrical unit cell.[59,60,61]

The situation is even worse in the case of the (2x1) reconstruction observed on cleaved Si(111). For silicon (7x7) adatom dangling bonds dominate the STM image. These bonds are half filled, so the same bonds are imaged at both positive and negative biases. In the case of the (2x1) reconstruction there are completely filled binding orbitals and empty anti-bonding orbitals. Positive sample bias images show only the empty states, while negative bias images show only filled states. This results in a relative shift of the image maxima in the $[0\bar{1}1]$ direction by 1.9 Å, half of the unit cell size, when the bias is reversed.[15]

In fact, Becker *et al.*[62] argue that virtually all of the $\sim 0.5$ to 1.5 Å corrugation observed on reconstructed silicon surfaces is due to "electronic" effects rather that geometry. They point out that silicon is typically imaged with a relatively large gap resistance of around 1 GΩ corresponding to a tunneling gap of 8 - 10 Å. With the predicted exponential decrease of observed corrugation with tunneling gap, an ad-atom in the 7x7 unit cell should give a "geometrical" corrugation of only 0.01 to 0.02 Å.

### 3.1.2. Current or constant height images

A second imaging mode uses the tunneling current $I(x,y)$ as a contrast signal.[63] The tip scan velocity or the feedback loop time constant is increased so that the tip position cannot respond on the scale of atomic corrugations. The feedback loop is still able to follow the general contours of the surface so that the average tunnel current is maintained at the setpoint, $<I(x,y)> = I_o$.

Interpretation of current images in terms of surface geometry is if anything less straightforward than for constant height images. It is very difficult to draw conclusions about structure in the $z$ direction, however variations in $I(x,y)$ across the atomic unit cell are related to variations in the electronic or geometric structure. In our laboratory we have observed that constant height and constant current images of the same surfaces generally show similar features, sometimes with higher resolution in the constant height images.

The constant height mode is most useful for atomically flat surfaces. Tip collisions are a problem on faceted or rough surfaces. High scan rates are a major advantage of the constant height mode, and atomic resolution can be obtained at horizontal scan rates over 250 Hz.[63] Such high scan rates minimize problems of thermal drift and improve the signal to noise ratio by shifting data acquisition to higher frequencies, which reduces the contribution from $1/f$ noise.[57]

### 3.1.3. Barrier height images

In the simple one-dimensional vacuum barrier model the tunneling current $I$ is proportional to $e^{-d\sqrt{\phi}}$ where $d$ is the width of the barrier and $\phi$ is the barrier height. The different functional dependence of tunnel current on barrier width and barrier height means that the STM can measure a "local barrier height" as proposed by Binnig[64] where $\phi(x,y)$ is proportional to $[\ \frac{1}{I}\frac{\partial I}{\partial z}(x,y)\ ]^2$. Experimentally the local barrier height can be measured by modulating the tip $z$ position at a frequency $\omega$ higher than the feedback loop roll-off and using a lock-in amplifier to measure $I(\omega)$, which is proportional to $\frac{\partial I}{\partial z}$. This signal can be used to generate a local barrier height image of the surface.

Topographic and local barrier height data can be acquired simultaneously to distinguish geometric changes in the surface and changes in the local barrier height related to changes in surface chemistry.[34,37,65]

Two factors complicate the interpretation of local barrier height data. First, surface topography influences the $\frac{\partial I}{\partial z}$ signal, since a vertical tip displacement changes the tunneling gap by $\Delta z \cos\alpha$ where $\alpha$ is the angle of inclination of the surface relative to the tip axis. For atomic resolution images this correction is usually negligible. The second difficulty is of a more fundamental nature. It is often found that the experimental values of $\phi$, particularly in measurements made in air, are substantially smaller than expected for the work function ( $\sim$ 4 eV). Values from 1 eV to as low as 0.001 eV have been found.

For large gap widths and small bias voltages, the barrier height should approach the work function. (Barrier height images are sometimes improperly called "work function" images. The work function is a global property of the surface at distances large compared to the atomic lattice spacing, while the barrier height is a local property measured at the short distances used in tunneling). As the tip approachs the surface and the barrier width decreases, the barrier height should also decrease, ultimately vanishing as an actual ohmic contact is made. For very small gap widths, the barrier will collapse completely. The tunneling currents are then described by the theories of metallic point contacts, where the currents depend on the density of states that can propagate through a small aperture. Gimzewski and Möller have observed this decrease in barrier height and the onset of metallic conduction by making direct measurements of $I(z)$.[44] Lang made theoretical calculations with a jellium model for the tip and sample and achieved excellent agreement with the results of Gimzewski and Möller.[66] For gaps larger than $\sim$ 6 Å, Lang predicts that the barrier height should approach the surface work function. Feenstra *et al.*[67] and Weimer *et al.*[68] have discussed modifications to the apparent barrier height resulting from band bending when tunneling to semiconductor surfaces with unpinned bands.

This variation of tunnel barrier with gap width cannot explain all of the observations of low barrier heights. Low barrier heights can also result from forces acting between tip and surface causing deformations of the tip or the substrate, so that the actual change in the tunneling gap $\Delta z_{gap}$ is less than the change in the piezo length $\Delta z_{piezo}$. Calculations of the barrier height based on $\Delta z_{piezo}$ rather than $\Delta z_{gap}$ will give values of $\phi$ lower than expected, since $\Delta z_{gap} < \Delta z_{piezo}$ when there is compression or deformation of the tip, surface or microscope structure. The example of figure 5 displays the variation of the measured value of $\phi$ (from modulation experiments) versus the gap resistance for a PtRh alloy tip and a Rh(111) crystal surface in UHV.[55] Barrier height is plotted against gap resistance $R_{gap}$ instead of tip-sample separation since this is the directly measurable quantity. The apparent barrier height increases from a very small value of 0.1 eV for $R_{gap} < 100$ MΩ up to several eV for $R_{gap} > 3$ GΩ. It is possible that for this particular system and tip, the compressive elastic forces are already sufficiently large to cause appreciable deformation of the gap below 3 GΩ. It is quite likely that the tip is contaminated by C or other common impurities that prevent tip-surface adhesion.

## 3.2. Tunneling spectroscopy and spectroscopic imaging

### 3.2.1. Electronic structure

Spatially resolved electron spectroscopy is one of the truly unique capabilities of the STM. No other surface technique can map the spatial variation of the density of states with atomic resolution. STM and scanning tunneling spectroscopy (STS) are providing data on surface electronic structure with a precision that would have been inconceivable just a few years ago.

Complete characterization of a surface with STM/STS would require measuring $I(x,y,z,V)$ over a reasonable range of each parameter, which could result in $\sim 10^7$ or more data points, an unwieldy number in most cases. A number of practical methods have been developed to obtain useful information from more specific experiments. Kuk[69] points out that some spectroscopic measurements are best performed with a blunt tip, since sharp tips localize the tunneling electrons to such a degree that the momentum

resolution is limited by the uncertainty relation $\Delta k \Delta x \sim 1$, making it more difficult to resolve fine details in the surface density of states. The tip electronic structure may also make a larger contribution to the measured $I-V$ curves for sharp tips. Since the exact tip geometry is not well characterized and is difficult to control, this will further complicate the interpretation of spectroscopic data.

Becker *et al.*[70] and Binnig *et al.*[71] performed some of the first tunneling spectroscopy measurements on semiconductors by ramping and modulating the bias voltage. The feedback loop was active during a voltage scan so the tunnel current was maintained at a constant value. In this way $z(I_o,V)$ and $\frac{\partial I}{\partial V}|_{I_o}$ were obtained simultaneously. As the bias voltage exceeds the local barrier height, tunneling is replaced by field emission from the tip. Electron standing wave resonances were observed in the gap as a function of gap width and bias voltage which were used to calculate the absolute gap width.[70]

Kaiser and Jaklevic[72] have performed spectroscopic measurements on metal surfaces. They modulated the bias voltage and used a lock-in amplifier to acquire the $\frac{\partial I}{\partial V}$ signal. A spectrum was acquired at constant gap resistance by sweeping the bias voltage and the current setpoint simultaneously with the feedback loop turned on. The resulting spectrum is proportional to the normalized differential conductance $\frac{V}{I}\frac{\partial I}{\partial V}$ signal. They correlated their STS spectra with photoemission results for Au(111) and Pd(111).

Later Becker *et al.*[60] acquired simultaneous topographic and conductance $(\frac{\partial I}{\partial V})$ images of the empty states of the reconstructed Si(111) (7x7) surface. They were able to show clear differences in conductance for the faulted and unfaulted halves of the (7x7) unit cell. By positioning the tip first over the faulted then the unfaulted half of the cell they measured the changes in electronic structure due to the reconstruction.

Hamers, Tromp and Demuth[61] introduced a more refined technique, current image tunneling spectroscopy or CITS. In CITS imaging, a normal topographic image is

acquired at fixed $I_0$ and $V_0$. At each point in the image the feedback loop is interrupted and the bias voltage is set to a series of voltages $V_i$ and the tunneling current $I_i$ recorded. The voltage is then returned to $V_0$ and the feedback loop is turned back on. Each $I-V$ spectra can be acquired in a few milliseconds so there is no appreciable drift in the tip position. This procedure generates a complete current image $I_i(x,y)$ at each voltage $V_i$ in addition to the topographic image $z(x,y)|_{V_0,I_0}$. CITS data can be displayed as $I-V$ curves recorded at fixed $x$, $y$ and $z$.

CITS data can be used to calculate a current difference image $\Delta I_{V_i,V_j}(x,y)$ where $V_i$ and $V_j$ bracket a particular surface state, producing an atomically resolved, real space image of a surface state. Hamers *et al.* used this technique to image the filled adatom state at -0.35 V (sample bias), the dangling bond state at -0.8 V and the silicon back-bond state at -1.7 V for the silicon (7x7) reconstruction. They also compared complete $I(V)$ curves for different points in the surface unit cell[61] To reduce the amount of CITS data that must be processed, a high resolution topographic image may be recorded and CITS $I-V$ curves recorded at a subset of points, such as a 16 x 16 or 32 x 32 point grid. By examining the topographic image, I-V spectra that correspond to interesting points in the unit cell may be selected.[73]

Stroscio, Feenstra and Fein[15] used a somewhat different approach. They opened the feedback loop and recorded $I-V$ curves for gap widths between 7.8 and 19.5 Å and calculated $I(z)$ and $\frac{\partial I}{\partial V}$ from these data. They showed that the normalized differential conductivity $\frac{V}{I}\frac{\partial I}{\partial V}$ for the (2x1) reconstruction of cleaved silicon (111) and for evaporated nickel films were essentially independent of $z$, and that the nickel differential conductivity curves were almost featureless compared to the silicon data. From this they concluded that the states of the tungsten tip did not significantly alter the spectral data for the Si(111) (2x1) surface.

Stroscio *et al.* also used the $I(z)$ data to calculate the inverse decay length $\kappa = [2m\bar{\phi}/\hbar^2 + k_{\parallel}^2]^{1/2}$ as a function of bias voltage. At low bias voltages only states near the silicon $\bar{K}$ surface band edge, the band minimum, contribute to the tunneling current.

These states have $k_{||} \sim 1$ Å$^{-1}$ and a decay length of $\sim 3$ Å$^{-1}$. As the magnitude of the bias voltage increases, the inverse decay length drops as states with smaller $k_{||}$ contribute to the tunneling current. Once states with $k_{||} = 0$ start to contribute at a bias of $\sim 1$ V there is no further change in the decay length.

Stroscio *et al.* introduced another useful spectroscopic imaging technique by recording constant height images with alternating scan lines acquired at different bias voltages. The result is a set of constant height images for different voltages in exact registry since the scan lines were interlaced during data acquisition. Relative shifts of image features within the unit cell can be accurately determined without complications from thermal drift or piezo creep. This approach is different from CITS imaging since all data is acquired under feedback control.

Stroscio and Feenstra[74] warn of a potential pitfall of CITS imaging. They argue that this method mixes the $z$ and $V$ dependence of spectroscopic data and can introduce spurious features since the appearance of the current images is a strong function of the $z$ stablization conditions. They acquired CITS data for Si(111) (2x1) with the loop stabilized at a sample bias of +1.5 V. A current image at +0.6 V shows a shift of the dimer image maxima by a significant fraction of the unit cell. The calculated differential conductance $\frac{\partial I}{\partial V}$ image at +0.6 V showed a similar shift, but the normalized differential conductivity image $\frac{V}{I}\frac{\partial I}{\partial V}$ had maxima at the same location as in the topographic stabilization image. In detailed studies of the silicon 7x7 reconstruction Berghaus *et al.*[75,76] analyze the effects of the stablization voltages on CITS spectra.

### 3.2.2. Vibrational spectroscopy

Most STM spectroscopic studies to date have focused on the electronic structure of surfaces and adsorbates. The electronic features are on the order of eV in width and can cause substantial changes in the tunneling conductance. In principle the STM should be able to detect spatially resolved surface vibrational features as well.[4] Vibrational structure is much weaker than electronic structure. Vibrational peaks are on the order of a

few meV in width and cause changes in the tunneling conductance of $10^{-3}$ or less. Molecular vibrational spectra have been successfully measured without spatial resolution by incorporating molecules into metal-oxide-metal tunnel junctions.[12]

Vibrational spectroscopy measurements with the STM would be very valuable. This would give a direct way to identify different chemical species in STM images. Vibrational spectroscopy poses a substantial technical challenge, however. Measurements must be made at cryogenic temperatures since the energy distribution of tunneling electrons is thermally broadened, and the variations in the tunneling gap due to external mechanical vibrations or electrical noise in the STM power supplies must be reduced to $\sim$ 0.001 Å or less. In addition, the mobility of surface species at room temperature is large and should therefore be quenched in order to maintain the tip on top of the adsorbed molecule during data acquisition. Several groups are working to develop experiments with sufficient sensitivity to detect vibrational spectra, but to date there are no unambiguous results.

### 3.2.3. Gap variation

One final spectroscopic technique involves the measurement of $I(z)$ spectra. This technique is related to local barrier height imaging described above. The tunneling feedback loop is opened and current is recorded as the tip is advanced toward the surface. Gimzewski and Möller[44] used this method to study the $z$ dependence of the tunneling barrier. They also showed that on metallic surfaces the tip $I-V$ characteristic could be used as a test of tip contamination.[55]

## 3.3. Image interpretation

### 3.3.1. Registry

There are a couple of generally useful techniques for interpreting STM images that deserve mention. One problem in interpreting STM data is the lack of direct

information on subsurface structure or registry. Wilson and Chiang[77] have stressed the value of observing registry changes across steps and domain boundaries and between islands of different structures. For example, by observing the boundary between silver ($\sqrt{3}$x$\sqrt{3}$)R30° overlayer islands and reconstructed (7x7) domains on silicon (111) they were able to show that the "honeycomb" model they had proposed for the silver overlayer based on their previous STM observations[78] was consistent with the observed registry, while the "embedded trimer" model proposed by van Loenen *et al.*[79] would predict a different registry.

Observations of the registry between different domains have also been used to distinguish between $T_4$ and $H_3$ overlayer sites for group III ($\sqrt{3}$x$\sqrt{3}$)R30° overlayers on Si(111)[80] and to study the structure of benzene molecules adsorbed on Rh(111).[81]

### 3.3.2. Fourier methods

Fourier methods provide another useful tool for STM image analysis. The use of Fourier filtering for image enhancement is often met with skepticism, since excessive filtering can produce the desired result from ambiguous data. However Fourier methods can be a powerful analytical tool for images with incommensurate structures or structures with different distance scales. Thomson *et al.*[82] used Fourier transforms to analyze images of incommensurate charge density waves on 1T-$TaS_2$. They identified the fundamental substrate peaks in their transformed images to make accurate corrections for drift, piezo coupling and calibration. Once a scale correction was applied to the data, comparison of substrate and CDW peaks in the transformed image gave an accurate determination of the angle between the CDW and substrate lattices, an important quantity for the theoretically analysis of the CDW system.

Demuth *et al.*[83] used Fourier methods to analyze the incommensurate "5x5" overlayer of copper on silicon 5x5. STM images of this overlayer show no long-range order, and small domains with different types of local order. The Fourier transform of these images permitted a direct comparison of the STM data with LEED observations on the same system. The transformed data showed a number of spots that could be associated

with three wave vectors, one corresponding to the 1x1 period of the silicon substrate, and two additional mutually incommensurate structures. Selectively back-transforming the regions of Fourier space corresponding to the different periodic components gave a real-space image of the spatial distribution of these different regions. This type of analysis is possible since numerical transforms of the STM images maintain both amplitude and phase information, while diffraction-based techniques like LEED give only the amplitude of the Fourier transform. Without the Fourier analysis it would have been difficult to determine if the STM images of the copper "5x5" structure represented two or more unrelated local structures or different aspects of one structure.

Demuth *et al.*[84] have also used Fourier transforms to separate features of different length scales in images of the Si(100)-(2x1) surface. Here a low-pass filtering and back-transform of the image shows just the step geometry, while a high-pass filtered back transform shows the atomic order with the step structure. Back-transforms of the half-order spots emphasize the dimers, while back-transforms of the integral-order spots highlight point defects in the overlayer.

### 3.3.3. Statistical analysis

Demuth has warned against "tunnel vision",[6] of focusing attention only on STM images of small, ideally ordered regions of the surface and neglecting defects and disordered regions. In addition to observing equilibrium structure, the STM can also provide important information on kinetic processes at surfaces through statistical analysis of surface features. One example of this is in the study of epitaxial growth on silicon (100). Lagally *et al.*[85] have analyzed this system. During epitaxial deposition of silicon on Si(100) long narrow islands of dimers are formed, with length to width ratios of ten or more. Several explanations have been given for this behavior -- that this is the equilibrium shape of the islands, or that silicon adatoms have anisotropic diffusion rates the dimerized (100) surface, or that the "sticking coefficient" is higher for adatoms on the ends than on the sides of islands. By careful statistical analysis of island growth and coarsening at various temperatures, Lagally *et al.* were able to show that the equilibrium length to width ratios for islands is no more than three to two and may be isotropic, that diffusion rates do not determine island shape, and that the non-equilibrium

shape of islands during epitaxy is due an anisotropic "sticking" probability for incorporation of atoms into the island. Other examples of statistical analysis of kinetic processes including overlayer nucleation and oxidation reactions are discussed below.

## 4. STM INSTRUMENTATION

Since the initial introduction of the STM by Binnig and Rohrer a wide variety of STM instruments have been designed. Specialized STM designs have been developed for particular applications, such as low temperature high magnetic field imaging,[86] variable temperature imaging,[87] and imaging in active electrochemical solutions.[88]

In addition, a whole array of new "scanning probe microscopes" have been developed, such as the atomic force microscope (AFM),[7] the scanning thermal conductance microscope,[89] and the scanning near field optical microscope.[90] Kuk and Silverman have recently reviewed the state of STM instrumentation.[69]

The common feature of all of these microscopes is that the spatial resolution depends on the probe size and the range of the surface-probe interaction. Images are acquired by mechanically scanning the probe over a surface and adjusting the probe-surface spacing using some kind of feedback mechanism. Probe scanners using piezoelectric translation elements and mechanical vibration isolation based on damped springs can now be constructed that can position a probe tip with an accuracy of $\sim$ 0.02 Å within a volume of several cubic microns. Some of these designs are quite stiff, with resonant frequencies of at least several kHz.

### 4.1. Instrument design

The basic elements of the STM instrument are the tunneling tip itself, a scanner mechanism that positions the tip with sub-angstrom resolution within a volume of a few cubic microns, a coarse approach mechanism that brings the tip and sample within scanner range, one or more stages of vibration isolation to protect the STM from ambient vibrations, a pre-amplifier circuit to measure tunneling currents, and control

electronics to operate the scanner. The STM electronics are usually connected to a computer data system for data acquisition and storage, image processing and display. The tunneling tip is critical to STM imaging, although it is not well characterized in most cases.

Virtually all STM designs use piezo electric elements for the scanner mechanism. The main experimental problems associated with piezo scanners are hysteresis and "creep", specially for large displacements. These properties have been analyzed by Pohl[91] and Nishikawa.[92] Thermal drift can also be a problem, although thermally compensated designs can minimize this effect.[87]

The coarse approach mechanism brings the tip within scanner range without "crashing" the tip. The biggest difference between STM designs is usually found in the coarse approach.

Vibration isolation is an important but straight forward part of STM design. Good results have been obtained with metal springs with magnetic eddy current damping and with elastic suspensions, which do not require external damping. Metal springs are normally used for vacuum STM designs, while elastic suspension is simpler in non-vacuum STM's. Pohl[91] and Kuk and Silverman[69] have analyzed the relation between vibration isolation, microscope stiffness and resolution, while Okano *et al.* have studied vibration isolation systems in detail.[93]

STM control and data acquisition can be accomplished using standard electronic techniques. The performance of the overall STM system generally is not limited by the performance of the scanning control electronics or data acquisition system. Both analog and digital feedback loops have been successfully used for STM control. For high resolution operation careful attention must be paid to electrical noise -- if the piezo drive has a response of 25 Å/volt then 0.01 Å spatial resolution requires voltage noise less that 500 $\mu$volts over the preamp bandwidth.

## 4.2. Noise

The ultimate resolution of the STM experiment is limited by noise sources. There are several classes of experimental noise -- fundamental physical processes associated with the tunneling processes, electrical noise in the current transducer or preamplifier, and the effect of external influences on the tunnel current such as mechanical vibrations and capacitive coupling to external voltages.

Möller *et al.* have made a careful experimental study of fundamental noise in the STM process.[57] Using a clean tip and sample in ultra-high vacuum, they found three main noise components, shot noise associated with statistically independent electrons that make up the tunnel current, thermal noise similar to Johnson noise associated with the gap resistance, and a $1/f$ noise component that increased with bias voltage and vanished in the limit of zero bias.

The shot noise density contributes an rms current of $\sqrt{2eI\Delta f}$ where $I$ is the average tunnel current and $\Delta f$ the noise bandwidth. This term is negligible in most experiments -- the signal to noise ratio for a 10 fA tunnel current in a 1 kHz bandwidth is 5.6.

The Johnson current noise density contributes an rms current of $\sqrt{4k_BT\Delta f/R_{gap}}$ or 129 pA $\sqrt{\Delta f/R_{gap}}$ at room temperature with bandwidth in Hz and gap resistance in $\Omega$. Möller *et al.* measured this value within experimental error using an evaporated silver surface and a tungsten tip in ultra-high vacuum.

The main source of electrical noise in the STM electronics is from the preamp or current transducer. The main noise contribution is from Johnson noise in the preamp feedback resistor. For large bandwidth preamps the combination of preamp voltage noise and input capacitance can be significant. FET input op-amps are available which reduce the input bias current and noise below 100 fA, so this is not a major problem. In addition to the fundamental preamp noise components, there can be additional excess noise from capacitive coupling of the STM preamp to other voltages, noise from ground currents induced by magnetic fields generated by computer monitors, ground loops and similar experimental problems.

### 4.3. Tunneling tips

The tunneling tip is often the most uncontrolled part of the STM experiment. The tip sharpness and composition can have a strong effect on both image resolution and contrast. Kuk *et al.*[94] and Hashizume *et al.*[95] have performed UHV STM experiments where the tunneling tip could be characterized by field ion microscopy before and after imaging. In this way a direct correlation could be made between STM resolution and tip geometry. In the large majority of cases, however, the tip geometry cannot be characterized independently. Many UHV experiments use tungsten tips electrochemically etched in sodium hydroxide, in some cases made from single crystal wire. These tips are often further processed in vacuum to clean or condition them for imaging. Various methods have been used, including annealing, ion sputtering, field emission from the tip at $\mu$A currents, voltage pulsing while in range on a ns to ms time scale, intentional contact with a surface, etc.

Tungsten tips are less satisfactory in air since a surface oxide can form which can interfere with imaging and even damage the sample,[55] so platinum tips are used instead. The platinum is usually alloyed with other noble metals like iridium or rhodium to increase its hardness. These tips are chemically inert compared to tungsten and do not form bulk oxides. Etching platinum group metals is more difficult than tungsten, but is possible using cyanide solutions or chloride salt solutions like NaCL/KCl. Good results are often obtained simply by mechanically cutting platinum alloy wires.

There are some indications that some STM images with exceptional spatial resolution have been obtained when a foreign atom is picked up on the end of the tunneling tip. Such imaging conditions are often unstable, and there may be sudden irreversible changes in image quality, consistent with the gain or loss of a particular atomic configuration on the end of the tip.

## 5. GRAPHITE AND LAYERED COMPOUNDS

More STM studies have been done of graphite mostly in its Highly Oriented Pyrolitic form (HOPG) than any other material, with the possible exception of silicon. The main reason for this is the easy of its preparation, by cleavage, and its chemical inertness that makes it ideal for imaging in air. Graphite is used as a standard for the initial testing and calibration of STM instruments and as a substrate for supporting other specimens. Many studies have been devoted to it, in order to understand basic aspects of the operation of the STM instrument. The results obtained by many different authors were unexpected in many cases. They illustrate many poorly known aspects of the operation of the STM and in particular the intimate interaction that exists between the tip and the surface. Graphite is used also very frequently as a substrate to deposit a variety of adsorbates, including metal clusters, polymers, and large organic molecules including liquid crystals and DNA.

The appearance of the graphite images is the result of the interplay between electronic and structural effects and of the strong mechanical interaction between tip and surface. In the following, we discuss the influence of the electronic structure of graphite on image contrast.

### 5.1. The Surface Unit Cell

The first remarkable feature of the images obtained from graphite, is the different types of structures obtained. These go from the "expected" honeycomb pattern of atoms to hexagonal arrangements where only half of the C atoms are prominent, to stripes, triangles etc.

This diversity of structures can be understood by considering first the peculiar electronic properties of the carbon atoms in their periodic arrangement and then the contribution arising from the structure of the tip. Many theoretical studies have been devoted to understand the most common appearance of the graphite unit cell. A simple geometric image of graphite would show two surface carbon atoms per unit cell, while many STM images show only one maxima or two inequivalent maxima. The first

theoretical model due to Tersoff was proposed to explain both the observation of anomalously large corrugations and the hexagonal arrangement of atoms with the 2.46 Å periodicity.[18] The tip is modeled by an *s*-wave function, and use is made of the peculiar property of graphite with a Fermi sphere that touches the Brillouin zone in six points (*H* points), allowing the surface states that contribute most to the tunneling to be represented by six plane waves along the surface with exponentially decaying amplitudes in the *Z* direction. Tersoff showed that the STM image should consists of a series of large dips spaced by 2.46 Å, the lattice spacing. One consequence of this model is that the images do not contain information on the position of the individual atoms in the unit cell. As mentioned above, Chen[40] proposes to include tip functions with higher components of the angular momentum quantum number in addition to the *s* symmetry functions to explain the high resolution observed in many of the graphite images.

Both the treatments of Batra *et al.*[96] and Tomanek *et al.*[97] explicitly include the fact that the two C atoms in the unit cell are inequivalent on account of the second layer of atoms. The "*A*" sites having a neighboring C atom directly underneath in the second layer, will have different electronic properties than the "*B*" site atoms with no neighbors in the second layer. The weak interaction between *A* atoms in the two layers will result in the build up of charge in the interlayer and the decrease of charge above the surface. Since the STM images are actually charge density profiles at the Fermi energy, Batra shows that the two types of atoms will appear with different electronic corrugation. In the treatment of Tomanek *et al.* the interaction between *A* atoms in the adjacent layers is taken into account to calculate the dispersion in **k** space of the bands arising from orbitals in the *A* and *B* type atoms. The dispersion splits the bands derived from *A* atom orbitals by 1.2 eV at the edge of the Brillouin zone, where the Fermi level is located. Since most of the tunnel current arises from states near the Fermi edge, the *B* atoms will contribute most of the current.

While in these models the tip is assumed to be ideal, i.e., either a structureless geometrical shape or even a delta function, real tips are not only more complex with one or more atoms participating in the tunneling process but also their shape and composition can change with time. Several models have been proposed that take tip effects into account in order to explain the changing appearance of the HOPG unit cell.

Colton *et al.* calculated the graphite images produced by a model tip consisting of a trigonal arrangement of C atoms, a four atom tip and a dimer. With this model tips most of the observed images could be generated.[98]

Another model was proposed by Mizes *et al.*[99] to explain the graphite images involves the simultaneous operation of several tips. Starting from the basic structure with only half of the C atoms visible (hexagonal type), the authors have shown that a suitable superposition of images generated by the various tips (one or two) with the appropriate amplitude and phase shift can reproduce the different types of structures observed. Support to this model comes from the fact that graphite can be deformed by the mechanical pressure exerted by the tip and the resulting elastic deformation helps to bring secondary tips into tunneling range.

### 5.2. Adsorbates on Graphite

Apart from its intrinsic interest, graphite is extensively used as a substrate where a variety of adsorbates can be studied. Metal clusters, liquid crystals, polymers and biological molecules are some examples of the type of adsorbates that are being studied.

Clusters of Au, Ag and Al were studied by Ganz *et al.*,[100] by evaporation in UHV. The clusters formed at coverages of roughly 0.1% of a monolayer, consisted of monomers, dimers and two dimensional islands. The islands showed a coexistence of phases, with an ordered but incommensurate interior, and disordered edges. Images of the edges of Au islands showed that some atoms formed a buckled chain arrangement, with the entire island rotated 4 ° relative to the substrate. Grain boundaries between two different regions in Ag islands were also observed. These results show that the STM is an excellent tool to study deposited clusters. Such a study is important in catalysis since it provides a way to model metal clusters and allows to obtain information of their structure in real space.

Other studies using graphite as a substrate include semiconductor clusters of $PbI_2$ and $BiI_3$ deposited from colloidal suspensions as reported by Sarid *et al.*,[101] and

phosphotungstic acid and rhenium carbonil complexes and organic molecules like acetone as reported by Lyding *et al.*.[87] Recently, Foster *et al.*[102] reported on the observation of di(2-ethylhexyl)phtalate molecules pinned to the graphite surface by the application of a 100 nsec, 3.7 V pulse to the tip that is immersed in the solution containing the molecules. According to these authors the effect of the voltage pulse was to bond the molecule to the surface. The pinned molecule can be removed from the surface with another pulse as the tip passed over the adsorbed molecule. Another important result obtained by these same authors[103,104] is the imaging of the interface between a solution of smectic and nematic liquid crystals and graphite. Ordered arrays of sorbic acid were observed on graphite at liquid helium temperatures by Smith *et al.*,[105] who also performed vibrational measurements.

Graphite is used extensively as a substrate in biological applications. This is a field of increasing activity in STM to study the structure of biomolecules. From the first results by Baro *et al.* in 1985,[106] till the recent reports on DNA imaging[107,108,109] more than 20 papers have been devoted to this effort. In spite of the promise of high resolution and simplicity of operation however, researches are still exploring the conditions in which STM can be applied to biology. This is because the interaction of the instrument and the biological material, in particular the force exerted by the tip against the surface, is not negligible as explained in the last section. The interested reader is referred to a recent paper by the present authors that discusses extensively the problems of electrical conductivity of the biomolecules, their fixation to the substrate and their identification.[110] Extensive discussion of biological applications can also be found in reviews by Gluckenberger *et al.*[111] and Stemmer and Engel.[112]

### 5.3. Charge density waves

The STM has been successfully utilized to study the electronic corrugation of layered compound surfaces, especially the metal di-chalcogenides, that results from the appearance of charge density waves (CDW). These two-dimensional waves have periodicities that can be commensurate or incommensurate with the substrate atomic periodicity and appear when the crystal is cooled below the transition temperature.[82] By adjusting the bias voltage, both the CDW and the substrate periodicities have been

observed. This area is one of the first to receive attention from the laboratories developing STM instruments. This subject has been recently discussed in detail by Coleman *et al.*.[113,114]

## 6. RECONSTRUCTED SEMICONDUCTOR SURFACES

Surface reconstructions on semiconductors have been investigated both theoretically and experimentally throughout the entire history of surface physics. Semiconductor surfaces reconstruct strongly due to the localized nature of semiconductor bonds, with most semiconductors undergoing a complete rearrangement of the local bonding geometry and changes in the translational symmetry at the surface, often extending two or more layers deep into the crystal. Some surfaces have a series of metastable reconstructions that can be observed in addition to the equilibrium geometry. In contrast, most metal surfaces do not reconstruct, showing only a relaxation of the interlayer spacings in the outer layers and some charge redistribution, without major rearrangement of the positions of the ion cores.

Before the advent of the STM, reconstructed semiconductor surfaces had been subjected to intense investigation using low energy electron diffraction, medium energy ion scattering, transmission electron microscopy and angle-resolved photoemission. In spite of substantial efforts, there was no general agreement on the nature of important reconstructions like the 7x7 surface of silicon (111) or the c(2x8) surface of germanium (111). Tunneling microscopy has transformed this situation in just a few years. Atomic resolution, real space images of the surface geometric and electronic structure, in conjunction with previous experimental and theoretical efforts, now provides a fairly complete picture of the surface reconstructions on the low index planes of silicon, germanium and gallium arsenide, although there are still some loose ends, such as the structure of the various reported reconstructions on the silicon (110) surface. Today the focus has shifted to investigating more complex problems, such as step structure, the kinetics of epitaxial growth, the study of metal-semiconductor interfaces and silicon surface chemistry.

More STM studies have been done on semiconductor surfaces that on any other system, with the possible exception of graphite. Semiconductors have great technological importance as well as complex and fascinating surface reconstructions. Atomic resolution STM images are easier to obtain on semiconductors than on other materials due to the large unit cells of the reconstructed surfaces and the localized nature of surface dangling bonds. Finally, much ground breaking research in tunneling microscopy has been done at IBM's labs in Zurich, Yorktown Heights and Almaden and also at Bell Labs, where there is a strong institutional interest in semiconductor surfaces.

### 6.1. Silicon (111) 7x7

From LEED studies annealed silicon (111) is known to form a 7x7 reconstruction at room temperature, while the silicon (111) cleavage plane showed a 2x1 reconstruction. Laser annealed, rapidly cooled silicon shows a "1x1" LEED pattern. LEED measurements on germanium (111) show a c(8x2) reconstruction. This picture is further complicated by the observation that the small lattice strain caused by growing germanium epitaxially on silicon (111) causes the germanium surface to adopt a 7x7 reconstruction.[115]

The driving force for the reconstruction of group IV semiconductor surfaces seems to be to minimize the surface dangling bond energy. All of the known reconstructions on these surfaces substantially reduce the number of dangling bonds.[30] Takayanagi *et al.*[116] first proposed the "dimer-adatom-stacking fault" or DAS model for the silicon 7x7 reconstruction based on their transmission electron microscopy results. The DAS model took into account the initial STM results on the 7x7 surface obtained by Binnig *et al.*[59] which retired the previous generation of models for the 7x7 reconstruction.

The DAS model involves silicon "adatoms" in a 2x2-like array on top of the silicon double layer in $T_4$ sites (see part b of figure 6). These are three-fold hollow sites, directly above silicon atoms in the bottom of the surface double layer. A 2x2 overlayer of adatoms alone would halve the number of dangling bonds. This is the basis for the Ge(111) reconstruction. The number of dangling bonds on silicon (111) is further reduced when atoms in the lower half of the surface double layer form dimer rows along the edges of

the unit cell, creating vacancies in the top half of the double layer. As a consequence of dimerization, a stacking fault is created, where half of the 7x7 cell is rotated 180°. Large features are created where the dimer rows meet called "corner holes". These holes through the top double layer expose the second double layer. The 7x7 reconstruction has created its own jargon, and the six remaining atoms in the top double layer not bonded to adatoms are called "rest" atoms. The 7x7 reconstruction reduces the 49 dangling bonds of the bulk-terminated 1x1 surface to 19 in the equilibrium surface.

Silicon images show rather large corrugations, typically a 1.0 Å variation in $z$ along the long diagonal. Sometimes after prolonged imaging the apparent resolution will increase temporarily, with corrugations as large as 1.5 to 1.75 Å. The high resolution may be due to the adsorption of foreign atoms, possibly small silicon clusters, on the end of the tip.[6]

Figure 7 shows more detailed STM images of the filled and empty surface states (sample biased positive and negative with respect to the tip) of the silicon 7x7 reconstruction obtained by Avouris and Wolkow.[73] These images immediately show the intimate connection between surface geometry and electronic structure. In the filled state image the difference between the faulted and unfaulted half cells are clear, as observed originally by Binnig *et al.*.[59] Becker *et al.*[60] identified the faulted half cell as the higher or brighter side in these images, while Demuth *et al* found the unfaulted half cell higher in empty state images. There is no way to separate geometric and electronic effects in the absence of detailed theoretical models of the 7x7 reconstruction.

Becker *et al.* have conducted a through review of the process of STM imaging of the silicon and germanium (111) reconstructions.[62] They conclude that the atomic-like features on these surfaces correspond to images of the dangling bonds. The dangling bonds on the twelve ad-atoms of the 7x7 unit cell dominate the STM images, with some additional intensity derived from the dangling bonds of the rest atoms. These are half-filled metallic-like dangling bond states, so they have a similar appearance in filled and empty state images.

This general model of the 7x7 surface has been tested by observations of similar reconstructions. The basic dimer-adatom-stacking fault model can be extended to any $(2n+1)$x$(2n+1)$ reconstruction. Becker, Golovchenko and Schwartzentruber have studied the 7x7 reconstruction of epitaxial germanium (111) grown on silicon (111)[115] and the 5x5 reconstruction on germanium-silicon (111) alloy surfaces.[117] Regions of 5x5 and occasional 9x9 unit cells can also be observed on pure silicon prepared by non-equilibrium methods like laser annealing[118] and low temperature epitaxial growth of silicon on silicon.[119] All of these studies can be understood in terms of the dangling bond analysis of the images.[62]

### 6.2. Germanium (111)

The germanium (111) surface shows some significant differences from silicon. Images of the reconstructed Ge surface show considerably more long range disorder, as seen in figure 8 obtained by Becker *et al.*.[62] The image shows interspersed regions of c(2x8), p(2x2) and c(4x2) local symmetry. The smaller unit cells had not been detected in LEED studies since the c(2x8) translational symmetry is a subset of the p(2x2) and c(4x2) structures and so the diffraction patterns of the smaller unit cells are subsets of the c(2x8) diffraction pattern. This is another example of a surface phenomena that is easily observed with the STM and difficult to detect by any other method.

Becker *et al.*[115,62] have analyzed the germanium STM images in terms of adatoms in a 2x2 lattice on top of the germanium double layer. The c(4x2) unit cell is the same as a 2x2 lattice with every other row of adatoms shifted one lattice spacing along the row direction. Likewise, the c(2x8) unit cell can be described as alternating strips of 2x2 and c(4x2) unit cells. They assign all of the adatoms to $T_4$ sites, three-fold hollows located over atoms in the bottom of the top double-layer, rather than to the open $H_3$ sites. This assignment is based on comparisons with the silicon (111). Small areas of 2x2 and c(4x2) symmetry can be observed on laser annealed silicon (111) along with 7x7 cells, and the registry shows all the silicon adatoms occupy $T_4$ sites as in the 7x7 lattice.[118] Theoretical calculations by Northrup[120] have shown the $T_4$ site is clearly favored over the $H_3$ site on a (hypothetical) silicon (111) $(\sqrt{3}\text{x}\sqrt{3})\text{R}30^\circ$ adatom lattice.

This model for the germanium reconstruction has more dangling bonds per atom than the silicon 7x7 reconstruction but no major sub-surface reconstruction, which presumably reduces the germanium surface strain. The close balance between minimizing surface strain and minimizing dangling bonds is shown by the observation of the 5x5 reconstruction in silicon-germanium alloys and the 7x7 reconstruction observed on Ge(111) when $\sim$ 30% Sn atoms are incorporated into the germanium surface.[121] The Sn atoms (identified by coverage) appear to be $\sim$ 0.4 Å "lower" than the Ge atoms in empty-state images.

The 2x2 adatom model for the germanium surface leads to significant differences in the electronic structure near the Fermi energy. In a 2x2, c(4x2) or c(2x8) adatom lattice there are equal numbers of rest atom and adatom dangling bonds. Becker *et al.* suggest that the result is a completely filled rest atom dangling bond state imaged only with a negative sample bias, and an empty adatom dangling bond state imaged only with positive bias. This is in contrast to the silicon 7x7 surface, where rest atoms outnumber adatoms, leading to a filled rest atom band and a partly filled adatom dangling bond band that is the dominant feature in STM images at both biases. They support this interpretation with a beautiful series of dual polarity STM images[62] on germanium and laser-annealed silicon that show voltage dependent shifts in the positions of the STM image maxima for 2x2, c(4x2) and germanium c(2x8) regions and no voltage-dependent shifts in silicon 7x7, 5x5 and 9x9 regions. Voltage dependent shifts are also seen for small areas of $\sqrt{3}$ ordering observed on both surfaces. Local $\sqrt{3}$ order on roughened silicon (111) was previously reported by Berghaus *et al.*.[122]

### 6.3. Silicon (111) 2x1

Silicon crystals cleave along (111) planes. The exposed surface shows a metastable 2x1 reconstruction instead of the equilibrium 7x7 reconstruction. Pandey[123] proposed the generally accepted model for this surface, the "$\pi$-bonded chain". The top double-layer of the surface reconstructs into alternating 5 and 7 member rings in the $[\bar{2}11]$ direction. The topmost atoms $\pi$ bond together to form a zig-zag chain along the $[0\bar{1}1]$ direction. These chains give rise to a completely filled $\pi$ bonding band and an empty $\pi^*$ anti-bonding band with a 0.45 eV surface band gap. This is in contrast to the

7x7 reconstruction with partly filled dangling bond states and no surface band gap.

STM images obtained by Feenstra *et al*[124,125] clearly show the corrugations between chains. They also observed that surface defects appearing as bumps or protrusions at the surface seemed to influence or be propagated along the chains. As the absolute value of the bias voltage is reduced below $\sim 0.2$ volts the structures due to lattice defects become prominent while the corrugation of the chains in the $[\bar{2}11]$ is attenuated. This indicates that the defects give rise to localized states in the band gap.

Under the proper conditions corrugations were also observed along the $\pi$ bonded chains in the $[0\bar{1}1]$ direction. The maximum corrugations were observed for small bias voltages, near the band edges.[15,74,126] Although there are two top-layer atoms per unit cell, only one maxima is seen. This can be explained using Tersoff's theory of "anomalous corrugation".[18,127] The major contribution to the STM images comes from the $\pi$ bonded electrons. At small voltages only states very close to the band edge, where $k_{||}$ corresponds to the Brillouin zone edge, contribute to the tunneling current. Since the state has the period of the lattice only one maxima per unit cell will be observed. When the bias is switched the maxima shift by half a unit cell in the $[0\bar{1}1]$ direction since the charge density in the bonding and anti-bonding states is out of phase by 180°, as measured by Stroscio *et al.*[74]

Pashley *et al.*[128] succeeded in forming regions of the 2x1 reconstruction on a silicon (111) crystal by annealing at 920° C then cooling at $>$ 150° C/min. They recorded topographs very similar to the images obtained by Feenstra *et al.* on cleaved silicon, although with lower defect concentrations. They also observed an extended ($>$ 150 Å) region of a 2x2 reconstruction on a rapidly cooled silicon crystal. Based on the observation of a dimer reconstruction on rapidly cooled crystals, they suggest that the high temperature silicon may be an ordered 1x1 phase rather than a disordered 7x7 adatom structure.

## 6.4. Silicon and germanium (100)

The (100) surfaces of silicon and germanium are both reconstructed with 2x1 symmetry, although 2x2, c(4x2) and 2x8 symmetries have occasionally been observed on silicon with LEED and atom diffraction. Both surfaces are thought to form dimers to reduce the number of dangling bonds, although the experimental and theoretical details of the dimer structure have been actively debated.

Tromp, Hamers and Demuth[129,130] have obtained filled state images of the dimerized silicon (100) surface showing both symmetric and buckled dimers. The "bean shaped" maxima observed in these images interpreted as the occupied dimer $\pi$-bonding orbital. They associate the bucked dimers with surface defects such as dimer vacancies. Near vacancies the dimer rows show large zig-zags due to dimers buckled in alternate directions. The amplitude of the dimer buckling decreases away from defects. When adjacent dimer rows are buckled in phase the local symmetry is 2x2, and out of phase dimer rows give local c(4x2) symmetry. Dimers appear symmetric in the absence of defects. Hamers, Avouris and Boszo report empty state images of the silicon (100) dimers.[131] There is a striking difference between the filled and empty state images. The empty state images show two round maxima per unit cell in place of the single bean-shaped maxima of the filled state image. These maxima are interpreted as the $\pi^*$-antibonding orbital. The antibonding state is anti-symmetric when reflected across the (011) plane through the center of the dimer bond, so the STM image shows a deep minima here, even deeper than that between dimer rows.

Hamers and Köhler have conducted a detailed study of defects on the (100) 2x1 surface and their electronic structure.[132] Two common defects are tentatively assigned as single and paired missing dimers. These defects appear as symmetrical depressions in both filled and empty state images, and I-V measurements show the local band gap is very close to the surface band gap measured in perfect regions of the 2x1 reconstruction. The third and most common defect type has a more complicated structure. In the filled state images one end of a pair of adjacent dimers appear to be missing, while in the empty state images the other end of the defected dimers appear to protrude well above the un-defected dimers. This asymmetric defect induces substantial buckling in nearby

dimers. Hamers and Köhler suggest one possible model for this defect is a 90° rotation of a dimer next to a dimer vacancy, but they stress that the local structure cannot be determined from the STM images due to the interaction of geometrical and electrical effects and that sub-surface changes in bonding may be involved.

I-V measurements show metallic behavior within $\sim$ 10 Å of the complex defects, as reported previously by Niehus *et al.*.[133] Since the defect density in the 2x1 reconstructed surface is at least several percent, Hamers and Köhler suggest that the observed surface Fermi level pinning is due to these complex defects.

LEED studies have reported reconstructions on Si(100) with 2x$n$ unit cells with n $\sim$ 6-10. Martin *et al.*[134] proposed a statistical model for these "reconstructions" based on a distribution of missing dimers. An STM study by Niehus *et al.*[133] basically confirmed this model, although they demonstrated that this type of ordering results from contamination of the surface by $\sim$ 1% of a monolayer of nickel atoms. They propose models for nickel-induced missing dimer defect formation.

The germanium (100) surface, studied by Kubby *et al.*,[135] has the same basic reconstruction as the silicon (100) surface with differences in detail. The germanium defect density is significantly lower, and defects do not seem to correlate with surface structure. The germanium dimers are asymmetric and the STM images are consistent with theoretical calculations indicating charge transfer from the "down" side to the "up" side of the dimers. The authors make careful comparisons between their I-V data and other surface sensitive spectroscopies. As in the silicon case, correlations between buckled dimer rows can create regions of p(2x2) and c(4x2) symmetry.

### 6.5. High index silicon surfaces

Although most STM efforts on silicon have focused on the (100) and (111) surfaces, a few studies have been made of higher index surfaces such as (110), (223) and (112). Neddermeyer and Tosch have studied all of these surfaces with their collaborators. The first of these results were obtained on the (112) surface.[122] This surface can be described

as two unit cell wide (111) terraces alternating with single height (001) oriented steps. The STM images could not be explained in terms of a uniform reconstruction with long range order. Instead terraces of varying widths with edges in the $[\bar{1}10]$ direction are seen, along with occasional larger (111) terraces. The $[\bar{1}10]$ edges showed a periodicity of 3.8 Å corresponding to the bulk lattice spacing. In between the well defined edges various features could be resolved, including "2x1"-type features, but these did not fit into any long range order.

The same group has reported similar results on the (223) surface, which is like the (112) surface with the width of the (111) terraces doubled.[136] As in the (112) case, rows of silicon atoms with the bulk periodicity are seen aligned in the $[\bar{1}10]$ direction. Various atomic-scale features are observed between these rows, but again with no apparent long range order.

The silicon (110) face has also been investigated by STM. A long list of reconstructions have been reported on this surface based on LEED and RHEED observations. The interpretation is complicated by reports that surface contamination by small ($\sim$ 1%) amounts of metals like nickel and copper can dramatically change the surface structure.

Hoeven *et al.*[137] and by van Loenen *et al.*.[138] report complex large scale structures consisting of areas of $\begin{pmatrix} 1 & 17 \\ 2 & 2 \end{pmatrix}$ and $\begin{pmatrix} -1 & 17 \\ -2 & 2 \end{pmatrix}$ reconstructions, sometimes referred to as "2x16", alternating with (15 17 1) and (15 17 3) facets. The reconstruction consists of a large unit cell with a pair of $\sim$ 25 Å wide strips stepped up and down by one (110) layer spacing (1.9 Å) running along either the $[1\bar{1}2]$ or the $[1\bar{1}\bar{2}]$ directions. The faceted surfaces show similar alternating strips but with a net gain or loss in the [110] direction. They plan to report details of the atomic structure of the reconstruction in a future publication.

Van Loenen *et al.*[138] also present images they attribute to nickel stablized reconstructions, including a 5x1 structure with 0.7% of a monolayer of nickel and a 2x5/4x5 structure with 25% of a monolayer of nickel. The nickel concentration was determined with XPS. The 5x1 structure is similar to one reported by Becker *et al.*[121] These

structures were formed without deliberate exposure to nickel, and great pains were required to avoid nickel contamination. In one case nickel atoms apparently diffused over the sample manipulator for a distance of $\sim$ 10 mm to reach the silicon sample.[138]

Neddermeyer and Tosch have also studied the silicon (110) surface reconstruction.[139,140] They made efforts to avoid nickel contamination, but could not directly detect trace amounts on the silicon surface. Their LEED observations show a 4x5 reconstruction with strong 2x1 beams. The STM images show rows of a basic 2x5 unit cell consisting of two "V" shaped maxima with apparent $c_2$ symmetry. Alignment of adjacent rows gives rise to the 4x5 symmetry, and there are a number of surface defects such as missing rows and breaks along the rows. There is no direct relation between the bulk structure and the two large and four smaller maxima seen in the 2x5 units, so the authors conclude that at least one subsurface layer is involved in the reconstruction. The 2x5 units on the (110) surface are associated with nickel contamination by van Loenen *et al.*,[138] who made direct measurements of the average nickel concentration with XPS and Rutherford back scattering.

### 6.6. Gallium Arsenide

Feenstra, Stroscio and collaborators have made a series of studies of the GaAs(110) surface, both clean and with various adsorbates (which will be discussed below). The (110) surface is the GaAs cleavage plane. The terminated bulk structure of this surface consists of zig-zag chains of alternating Ga and As atoms. STM images of this surface show a single maxima per unit cell.[141] Theoretical calculations predict charge transfer from the Ga dangling bond to the As dangling bond, resulting in a filled dangling bond orbital near the As atom and an empty dangling bond orbital near the Ga atom. A bond length conserving buckling of the Ga-As surface layer is predicted which moves the As atoms outward from the surface relative to the Ga atoms. Feenstra *et al.*[28] obtained voltage dependent images of the (110) surface consistent with this model. Filled state and empty state images each show one maxima per unit cell, with a shift of half a lattice constant along the $[1\bar{1}0]$ direction and by 2.1$\pm$0.37 Å in the [001] direction when the tunneling polarity is reversed. By comparing theoretical charge density calculations with the experimentally observed shift in the [001] direction (as

discussed above) the buckling angle was calculated to be $\sim 30^\circ$.

Feenstra and Stroscio have also made careful measurements of the GaAs surface band gap.[67] The defect free GaAs(110) surface has no states in the gap, so the Fermi level is not pinned. I-V curves for $n$ and $p$ type GaAs show a shift in the conduction and valence band edges of $\sim$ 1.5 volts corresponding to the bulk band gap. Dopant induced states appear in the I-V curves near the appropriate band edge.

Since the Fermi level is not pinned at the GaAs surface, band bending would be expected to influence the STM I-V characteristics. The authors analyze this case in detail, and conclude that neither the flat-band picture nor the simple band bending picture is consistent with the STM observations.[67] They then calculate the combined effects of tunneling through the tip-surface gap and tunneling through the depletion region inside the GaAs surface resulting from band bending. This last model is generally in agreement with the experimental I-V curves. Tunneling through the depletion region made a significant contribution to the STM tunnel current for band bending up to $\sim 0.2$ eV (with dopant concentrations of $1 \cdot 10^{18}$ cm$^{-3}$). This analysis implies that at certain voltages the STM tip would actually image the depletion layer interface several atomic layers *below* the geometrical surface of the crystal, although in fact the feedback loop was so unstable that topographic images could not be acquired in this voltage range. Tip induced band bending has also been analyzed by Weimer *et al.*,[68] including the effects of band bending on $\frac{\partial I}{\partial z}$ measurements.

Pashley *et al.* have studied the GaAs(001) surface as grown by molecular beam epitaxy.[142,143] In the (001) direction the crystal consists of alternating planes gallium and arsenic atoms, and MBE growth normally starts and ends with the arsenic terminated surface. The surface symmetry as determined by LEED and RHEED is either 2x4 or c(2x8). The surface As atoms are expected to reduce the number of dangling bonds by forming dimers in the $[\bar{1}10]$ or 2x direction. The longer period in the [110] direction has been attributed to dimer buckling or to missing dimers. The STM observations of Pashley *et al.* clearly support the missing dimer model, which is favored according to Chadi's total energy calculations.

The basic unit of the GaAs(001) surface is a group of three parallel dimers followed by a missing dimer. The filled state STM images show strips of As dimer triplets separated by narrow grooves due to the missing dimers. If every other strip is shifted one substrate lattice spacing in the 2x direction the surface has c(2x8) symmetry, while aligned strips have 2x4 symmetry. The authors report that empty state images were unstable, which they explain in terms of calculations that predict a higher empty state density around the sub-surface Ga atoms and a low density of empty states at the surface. The 2x4 structural unit seems quite stable, and islands or holes in the surface usually consist of one or more 2x4 units lined up in the 2x direction. Steps are $\sim$ 2.8 Å high, corresponding to the spacing between As planes in the [001] direction.

### 6.7. Steps on semiconductor surfaces

Step structure on low index surfaces can be a major factor controlling surface reactivity, but before the development of the STM little direct information was available on step structure. Steps are thought to provide the active sites for many gas-solid chemical reactions. Adsorbate structures may nucleate at step edges, and steps are important in epitaxial crystal growth. Information on step structure is difficult to extract from diffraction, ion scattering and photoemission experiments, the main techniques used for surface structural studies. High resolution transmission electron microscopy can give information on some step structures.

Recent STM results on semiconductor surfaces give direct structural information on several types of the simpler step structures. Becker *et al.* reported some of the first results on step structure for silicon (111) 7x7.[144] They showed that the 7x7 reconstruction persists right up to the step edge, and that many steps were aligned with the 7x7 unit cell. The most commonly observed steps have straight edges and run in the $[11\bar{2}]$ and $[\bar{1}\bar{1}2]$ directions cutting through the 7x7 corner holes at both top and bottom (111) terraces. TEM and later STM studies show that the $[11\bar{2}]$ steps are more stable than the $[\bar{1}\bar{1}2]$ steps.[119] This is probably related to the effects of the DAS stacking faults. Another commonly observed step structure is not straight. Instead the step follows a radius around the 7x7 corner hole so that the step edge is just outside the second ring of adatoms.[119]

Feenstra and Stroscio have analyzed one step structure on the cleaved silicon 111-2x1 surface.[145] Many steps on this surface were oriented in the $[2\overline{11}]$ directions with straight edges. There did not seem to be a direct coupling between the step structure and the surface reconstruction, as was seen for the 7x7 case.

The case where the 2x1 dimer rows are parallel to the top edge of the $[2\overline{11}]$ step was analyzed in detail. Here the dimer reconstruction persists up to and through the double-layer step edge. The sharp step edge transition takes place in 4/3 of a 2x1 unit cell, or 8.9 Å, the minimum possible distance consistent with the stacking of the silicon layers. The structure along the step edge has the substrate periodicity of 3.84 Å. The STM images of the steps show voltage dependent atomically resolved features which the authors associate with surface dangling bonds.

The first conclusion is that the step edges are "rebonded". A terminated dimer step structure would have three dangling bonds per unit cell. The rebonded geometry distorts the lattice, replacing a normal six member ring of silicon atoms with a five member ring and one dangling bond at the step edge. The authors then try to determine which of three possible ring models describes the rebonded step edge geometry. They assume that the each dangling bond is localized at an atom and that the atomic position is within $\sim$ 1.5 Å of the bond maxima in the STM image. Two step geometries are observed, one where the maxima are separated by $\sim$ 0.5 Å and a second where the separation is $\sim$ 4.5 Å. The first geometry is consistent only one model, a $\pi$-bonded step geometry consisting of alternating five and seven member rings of silicon atoms. The second observed geometry is consistent could not be assigned with certainty.[145]

Step structure has been investigated in greater detail on the Si(001) and Ge(001) surfaces where many steps are oriented in the [110] direction. Here there is an additional interaction between the 2x1 dimer orientation and the step edges. Steps are classified as type *A* when the dimer rows at the top of the step are parallel to the step edge, and type *B* when they are perpendicular. On the 100 surface the dimer direction rotates 90° when a monatomic step is crossed. Hamers, Tromp and Demuth[130] described the step geometry on this surface. For type *A* steps the dimers were strongly buckled. (On flat

terraces buckled dimers are associated with defects.) The center of the dimer rows on the lower terrace were always aligned adjacent to an upper terrace dimer with the "up" atom nearest the step edge. For type $B$ steps the dimer row at the bottom of the step can include the first row of atoms or start with the second row. Both geometries were observed. Kubby *et al.* observed the identical behavior for [110] steps on germanium (001).[135]

Wierenga *et al.*[146] and Griffith *et al.*[121] examined the structure of steps on silicon and germanium cut $\sim 4^\circ$ of the (001) plane toward the [110] direction in greater detail. They obtained results consistent with total energy calculations of Chadi, who predicts that double height $B$ steps ($D_B$) will have lower energy than a pair of single steps ($S_A$ and $S_B$), while double height $A$ steps ($D_A$) are energetically unfavorable. Most of the steps on both silicon and germanium were $D_B$ steps. At kink sites $D_B$ steps usually split into a pair of single steps. This avoids the unfavorable $D_A$ geometry which was not observed on the (001) surfaces.[130,146,121]

Schwartzentruber *et al.*[147] have studied the equilibrium and non-equilibrium step behavior on silicon. They found that $D_B$ type steps were predominant on surfaces cut a few degrees away from [001], but for small vicinal angles ($\sim 1^\circ$) single steps were the majority and they observed no tendency to form double steps even with prolonged annealing. The kink density in step edges also showed no sign of decreasing during annealing, and surfaces dominated by double steps always showed some concentration of single steps at kink sites.

### 6.8. Epitaxial growth of semiconductors.

Kinetic processes like epitaxial growth are another class of problems that the STM can study directly on the atomic level while other techniques allow only indirect conclusions based on statistical evidence. To date the studies of epitaxy have focused on the technologically important silicon (001) and (111) planes. Köhler, Demuth and Hamers[119,148] have studied temperature dependent silicon on silicon (111) epitaxy between room temperature and 500 ° C. At room temperature silicon atoms first adsorb

on top of rest atoms in each 7x7 half cell. These "extra" adatoms serve as nuclei for the growth of amorphous silicon islands. As the temperature increases to $\sim 250^\circ$ C the mobility of the deposited Si atoms increases and fewer islands are nucleated. Around $300^\circ$ C growth becomes epitaxial. Even small islands show elements of the 7x7 order such as a corner hole feature surrounded by a few adatoms. This suggests the 7x7 structure is stablized by local order more than long range effects. No islands are observed within $\sim$ 100 Å of a step edge, which gives an estimate of the surface diffusion mean free path.

As the substrate temperature increases fewer but faster growing islands are nucleated. The island 7x7 structure is often in registry with the substrate 7x7 lattice. Islands nucleate preferentially at defects like domain boundaries, and the islands themselves often have some local order reflecting other periodicities including 5x5, 9x9, 3x3, 2x2 or $\sqrt{3}$x$\sqrt{3}$. One striking feature is the growth of islands on top of islands (figure 9). This implies that silicon atoms initially adsorbed on the substrate terraces diffuse up onto an island to nucleate and grow a third layer. The authors suggest this is related to a higher defect density on islands which produces more favorable sites for nucleation.[119] At substrate temperatures above $\sim 500^\circ$ C almost all silicon atoms were incorporated at step edges, which implied that the mean diffusion path length was larger than the typical terrace width of $\sim$ 500 Å.

Epitaxial growth has also been investigated on the silicon (001) surface. There is particular interest in growing epitaxial surfaces with only one domain (only 2x1 or only 1x2) since such a surface is an ideal substrate for the epitaxial growth of III-V semiconductor layers. Epitaxial growth at moderate substrate temperatures ($\sim 450^\circ$ C) has been observed to produce preferential growth at type *B* step edges, which tends to cover up the type *A* steps.[149] This phenomena is related to the formation of highly anisotropic islands on the dimerized (001) surface. These islands typically have long rows of parallel dimers, with aspect ratios of 20:1 or more.[149,148,150,85]

Various explanations have been given for this anisotropic growth including anisotropic binding energy at step edges[149] and anisotropic diffusion rates across the 2x1

surface.[148] Lagally *et al.* have demonstrated that this phenomena is not caused by diffusion or by energetics but by another kinetic process. The accommodation probability or "surface sticking coefficient" is higher at the ends of parallel dimer rows and therefore at type $B$ steps than at the ends of dimers or type $A$ steps.[85,150] They find the equilibrium shape of islands on the (001) surface closer to 3:2 than 20:1.

## 7. CHEMISORBTION ON SEMICONDUCTOR SURFACES

### 7.1. III-V adsorbates on silicon

The STM has been used to study chemisorption of four group three elements on silicon -- boron, aluminum, gallium and indium. All of these elements can produce an ordered $(\sqrt{3}x\sqrt{3})R30^\circ$ overlayer on silicon (111). The three metals also produce a range of different ordered structures at higher coverages. Comparison of these results can contribute to a general understanding of silicon chemisorption.

#### 7.1.1. Group III $\sqrt{3}$ overlayers on silicon (111)

STM images of the $\sqrt{3}$ overlayers are basically similar for all of the group III adsorbates. In each case both filled and empty state images show a single maxima per unit cell with no voltage dependent shift in the position of the maxima. The simplest model for the trivalent group III adsorbates involves atoms adsorbed in a three-fold site on top of the silicon double layer. This geometry satisfies all of the silicon dangling bonds at the surface. There are two types of three-fold sites available, the $T_4$ site located above a silicon atom in the lower half of the surface double layer, and the $H_3$ site where there is no sub-surface silicon atom.

Total energy calculations by Northrup *et al.*[151,120,152] indicate that the adsorption energy in the $T_4$ site is $\sim$ 0.2 eV lower than the $H_3$ site for aluminum, gallium and indium when surface relaxations are taken into account.

Nogami, Park and Quate have studied indium[153,80] and gallium adsorbed on silicon (111).[154,155] A complete $\sqrt{3}$ overlayer corresponds to a metal coverage of 0.33. STM observations at lower coverages show islands of the $\sqrt{3}$ structure as well as regions of the silicon 7x7 structure. Comparing the adatom registry between different $\sqrt{3}$ islands and 7x7 regions shows that the metal overlayers involve only one type of adsorption site, the $T_4$ site. Hamers and Demuth[156,157,158] compared the registry of different $\sqrt{3}$ islands of aluminum and also found only one adsorption site for all islands, which they provisionally assign as the $T_4$ site after comparing STM $I-V$ curves to theoretical calculations.

Zegenhagen *et al.*[159] have also investigated gallium on silicon (111). They also observed island registry consistent with $T_4$ gallium adsorption sites. They then directly determined the silicon-gallium spacing as 1.49±0.03 Å using x-ray standing wave resonance fluorescence, in reasonably good agreement with the prediction of 1.33 Å from total energy calculations. This measurement gives an independent confirmation of the $T_4$ site since the standing wave height measurement is closer to the calculated $T_4$ value than to the calculated $H_3$ value.

Two types of defects have been observed in the $\sqrt{3}$ overlayers. One type of defect is an adatom site that appears lower in filled state images and higher in empty state images. Hamers assigns this defect to silicon adatoms substituted for aluminum atoms in the overlayer[157] by observing the increase in the defect density as the aluminum coverage is decreased. Nogami *et al.* observe similar defects in gallium[154] and indium[80] overlayers which they also attribute to substituted silicon. Electronic structure calculations for the group III metal atoms in three-fold sites predict an empty $p_z$ orbital above the metal atom, while three-fold silicon adatoms will have a partly filled dangling bond. This is consistent with a silicon adatom that is more prominent in filled state images and less prominent in empty state images.

The second type of defect observed in aluminum overlayers appears as a $\sim$ 2 Å deep depression in both filled and empty state images. Hamers attributes this defect to a true overlayer vacancy.[157]

At indium or gallium coverages below 0.33 the $\sqrt{3}$ overlayer is not formed, instead metal atoms substitute for silicon adatoms within the ordered 7x7 regions. These substituted metal atoms appear higher than silicon adatoms in empty state images and lower in filled state images, just as in the $\sqrt{3}$ case. Metal atoms appear at least six time more likely to substitute for one of the "edge" adatoms than for the silicon adatoms adjacent to the corner holes in the 7x7 overlayer, but there is no clear preference for the faulted or unfaulted half of the unit cell.[80,154]

Hamers and Demuth have carefully analyzed the electronic structure of the substitutional silicon adatoms in the $\sqrt{3}$ aluminum overlayer.[160,157] STM $I-V$ curves over the defect free $\sqrt{3}$ overlayer show a well defined band gap, while $I-V$ curves acquired over substituted silicon adatoms show a state at -0.4 eV corresponding to the silicon dangling bond. Since this state is below $E_F$, the dangling bond state should be occupied by two electrons and be negatively charged, causing local surface band bending. In fact band bending is not observed for substituted silicon atoms, although band bending is observed for other types of defects, such as those at island edges, with the expected $\sim$ 15 Å screening length. This observation implies that the defect is not charged, even though the state is below $E_F$.

Hamers and Demuth resolve this apparent contradiction by considering multi-electron effects. The substituted silicon atom is a localized point defect, since $I-V$ curves acquired over aluminum adatoms adjacent to defects are identical to those for atoms far removed from the defect sites. For localized sites the one-electron picture is inadequate and Coulomb repulsion must be considered. This means that the energy of the state depends on its occupation, and the $I-V$ peak at -0.4 eV corresponds to a singly occupied dangling bond, while the doubly occupied state has an energy above $E_F$. Hamers and Demuth conclude that this substitutional silicon adatom state is responsible for Fermi level pining on the $\sqrt{3}$ aluminum surface.

The interpretation of the $\sqrt{3}$ boron overlayer differs from that of the aluminum, gallium and indium overlayers. Thibaudau *et al.*[161,162] first imaged the boron-induced $\sqrt{3}$ overlayer with the STM. The overlayer was produced by surface segregation after

annealing boron-doped silicon wafers for many hours. The STM topographs showed a clear asymmetry along a line connecting adjacent $\sqrt{3}$ maxima, which is inconsistent with the simple adatom model for the overlayer. The authors proposed a new model for the boron induced overlayer with silicon atoms in $T_4$ adatoms sites and substituted boron atoms in one of the three silicon sites in the bottom half of the silicon surface double layer.

Bedrossian *et al.*[26] and Lyo *et al.*[27] later and simultaneously reported independently obtained results on the boron-induced $\sqrt{3}$ overlayer. Neither group observed the asymmetry in the STM topographs reported by Thibaudau *et al.*. Both groups conclude on the basis of their respective total energy calculations that the boron atom substitutes for the silicon atom located below the silicon $T_4$ adatom site, finding this lower in energy by 0.93 and 1.00 eV relative to boron in the $T_4$ site. Lyo *et al.* also reports low energy ion scattering results that rule out surface boron. Both groups observed a certain percentage of $\sqrt{3}$ adatoms appeared higher in both filled and empty state images. STM $I$—$V$ curves for the raised atoms showed an increased density of states and a reduced band gap. The raised atoms were attributed to silicon $T_4$ adatoms without sub-surface boron atoms.

The difference between the boron structure and the other group III adsorbates was explained in terms of the reduced covalent radius of boron relative to Al, Ga and In. A shorter B-Si bond length significantly reduces the strain energy associated with the $T_4$ geometry when the boron atom is located below the $T_4$ adatom.

### 7.1.2. Other group III structures on silicon (111)

Aluminum, indium and gallium each produce different ordered structures at coverages above 0.33, which corresponds to the complete $\sqrt{3}$ overlayer. For aluminum on silicon (111) Hamers[157] reports a ($\sqrt{7}$x7)R19.1 ° structure at a coverage of 3/7 monolayer and a 7x7 structure at $\sim$ 1-2 monolayers. Filled state images of the $\sqrt{7}$ surface show a single maxima per unit cell, and registry comparisons with adjacent $\sqrt{3}$ domains place the maxima above a silicon surface atoms. Empty state images show three

equivalent maxima. STM $I-V$ measurements show a surface band gap for the $\sqrt{7}$ structure. Hamers proposes a model for the surface consisting of three aluminum adatoms per unit cell, with each adatom bridging two top-layer silicon atoms. The empty state maxima correspond to unoccupied $p_z$ orbitals located above the aluminum adatoms. This model leaves one top layer silicon atom with a dangling bond surrounded by silicon atoms bound to aluminum. Hamers proposes that charge transfer from the aluminum-silicon complexs fills the dangling bond state, leading to a surface band gap and a single maxima in the filled state images. He points out that this model, while consistent with the available data, has not verified by electronic structure calculations.[157]

An aluminum induced 7x7 structure is observed at still higher coverages. This structure shows poorly resolved, partly disordered protrusions in each half of the 7x7 unit cell. Filled and empty state images are similar, with no evidence for stacking faults. Hamers suggests this structure is unrelated to the DAS structure, and that it may be the result of strain in quasi-epitaxial growth of aluminum on silicon.[157] Nogami *et al.* have observed a $\sqrt{31}$x$\sqrt{31}$, a $\sqrt{7}$x$\sqrt{3}$ and a 4x1 indium overlayer as well as flat islands.[80,155] Figure 10 shows a filled state image of the indium $\sqrt{31}$x$\sqrt{31}$ overlayer (in matrix notation $\begin{pmatrix} 5 & 1 \\ -1 & 6 \end{pmatrix}$) corresponding to a coverage of $\sim$ 0.6 monolayers along with one possible model structure. The maxima in the triangular sub-units have a 1x1 space rather than the 2x2 adatom spacing of clean silicon 7x7. As coverage increases a 4x1 structure is observed. A cross section in the 4x direction shows a single broad maxima in the filled state images and two maxima in empty state images. The authors do not propose a model for this structure except to point out that the 4x spacing is fundamental to the structure -- it is not due to correlated dimer rows. They also observe a "$\sqrt{3}$x$\sqrt{7}$" structure consisting of rows rotated by 30° relative to the rows of the 4x1 structure which is always associated with the 4x1 structure.

As indium coverage increases more and more islands with no detectable corrugations are observed. The authors attribute these features to close-packed indium metal islands.

The only high coverage structure for gallium on silicon (111) observed in diffraction experiments is a "$\sqrt{6.3}$x$\sqrt{6.3}$" overlayer seen by RHEED. Park, Nogami and Quate[155] have observed an STM structure composed of triangular units with edges oriented along $[\bar{1}10]$ directions. The structure lacks long range order, and a Fourier transform of the image gives a period of 5±0.5 silicon lattice spacings. The internal structure of the triangular units involves honeycomb-like features.

### 7.1.3. Arsenic on silicon (111)

Arsenic adsorption on the (111) face of silicon or germanium produces a passivated surface by substituting for silicon in the top half of the surface double layer. Each surface arsenic atom forms three bonds to the underlying silicon surface, completely eliminating surface dangling bonds. Becker *et al.*[163] have performed electronic structure calculations and obtained STM images and $I-V$ curves that support this model. STM images of the Si(111)-As surface show a 1x1 periodicity with 0.05 to 0.30 Å corrugation in empty state images and a weaker corrugation in filled state images. Electronic structure calculations show the maxima in the STM images correspond to empty state density localized over the silicon atoms in the bottom of the surface double layer, while filled state maxima are associated with weak $p_z$-like orbitals located at the arsenic atom positions.

This model for the silicon surface is confirmed by x-ray standing wave measurements obtained by Patel *et al.*[164] that locate the arsenic atoms 0.17±0.03 Å above the equilibrium position of silicon atoms in the terminated bulk structure. Copel *et al.*[165] have performed STM and medium energy ion scattering on the same surface, and they locate the arsenic atoms 0.2±0.10 Å above the bulk silicon position. They also note no evidence for substitutional silicon point defects in the arsenic layer, which are commonly observed for group III adsorbates.

Becker, Klitsner and Vickers have studied the defects in arsenic overlayers on the Si(111), Ge(111) and and Si(100) surfaces in more detail.[166] On Ge(111)-As the surface consists of (1x1) terraces of ~ 100 Å separated by "trenches" three lattice spacings wide

running along the [$\bar{1}$10] and equivalent directions. The authors propose the trenches relieve surface strains caused by the $\sim$ 2% mismatch between the Ge-Ge and Ge-As bond lengths. This type of trench is not observed on the Si(111)-As surface which has a larger bond length mismatch, instead a high concentration of point defects or "debris" are observed. Prolonged annealing fails to reduce the defect concentration on flat surfaces, but the defect concentration is significantly lower on stepped surfaces where (111) terrace widths are below $\sim$ 50 Å.

Surface dimers are still observed on the Si(100)-As surface since each surface atom in the terminated bulk structure forms only two bonds to deeper layers. The arsenic surface dimers are symmetrical, unlike the Si(100)-2x1 reconstruction, and missing dimer type defects are not observed.[166] A double height rebonded step geometry is favored on a stepped clean silicon (100) surface. When arsenic is added to the surface the rebonded geometry is no longer required to reduce the number of surface dangling bonds, and instead a tendency to reduce the step density by forming arsenic passivated (111) facets is observed.

### 7.2. Transition metals on silicon

Transition metal-silicide interfaces are technically important for semiconductor devices. STM studies of the initial stages of adsorption on silicon (111) have been carried out for several metals including nickel, copper, silver, gold and palladium. Structures with long range order are observed for silver, gold and nickel, while copper and palladium overlayers show only local order.

Trace amounts of nickel are known to induce significant changes in silicon surface structure. The Si(110)-4x5 and Si(100)-"2x8" cases have been discussed above. Wilson and Chiang[167] have investigated the nickel-induced "$\sqrt{19}$" or $\begin{pmatrix} 3 & 2 \\ -2 & 5 \end{pmatrix}$ structure on Si(111). The most striking features in STM images of both polarities are hexagonal rings of maxima one lattice spacing apart. These rings form the $\sqrt{19}$ lattice with sixteen times the area of the silicon 1x unit cell. The authors present a model for the surface, based on the STM images and SEXAFS results, consisting of a single nickel atom per unit cell

located in a six-fold site inside the silicon surface double layer. A group of six silicon adatoms around the sub-surface nickel satisfy most dangling bonds. The closest packing of these hexagonal silicon-nickel complexes results in the $\sqrt{19}$ lattice. One additional silicon adatom helps satisfy dangling bonds in the remainder of the unit cell. Using this model the authors are able to explain all the features observed in the STM images, including the structures at anti-phase domain boundaries and typical defects.

Dumas *et al.*[168] have studied the deposition of gold on Si(111). Deposition of $\sim 0.6$ monolayers of gold at a substrate temperature of $\sim 700^\circ$ C results in a $\sqrt{3}$ LEED pattern. STM images of this surface also show ordered regions of $\sqrt{3}$ symmetry with one maxima per unit cell. The authors report the maxima have a triangular shape, which would be consistent with a surface overlayer consisting of gold trimers.

Tosch and Neddermeyer have studied the initial stages of silver adsorption on Si(111)-7x7 at room temperature.[169,170] Initial silver adsorption produces triangular silver clusters centered on the inner adatoms in one half of the 7x7 unit cell. Clusters form preferentially on the faulted half of the unit cell. STM $I$—$V$ measurements over cluster sites show that the density of states significantly reduced between $E_F$ - 0.5 eV and $E_F$ + 1.0 eV. The authors conclude that the initial Ag cluster consists of six metal atoms that bind to both the inner adatoms and the rest atoms, satisfying all of the dangling bonds associated with these atoms. Similar Ag islands have been reported by Demuth *et al.*.[171]

As more silver is deposited the initial islands expand to fill half of the unit cell, avoiding the dimerized silicon atoms between corner holes. At still higher coverages flat islands without measurable corrugation are formed which nucleate at the initial clusters. If the flat islands are assumed to consist of silver atoms packed into (111) planes the island area is consistent with the silver coverage.

If the silver covered Si(111) surface is annealed above $\sim 200^\circ$ C a 3x1 ordered surface is formed at a silver coverage of 1/3 monolayer and a $\sqrt{3}$ surface at a coverage reported as either 2/3 or 1 monolayer. Wilson and Chiang[78] have obtained STM images

of the 3x1 silver structure showing rows in the [$\bar{1}$10] direction spaced 3 unit cells apart, with a faint 1x corrugation along the rows. They interpret these images in terms of LEED models for this structure, with one Ag atom per unit cell adsorbed in a three fold site on top of the silicon double layer. This model leaves one silicon dangling bond per three surface atoms.

At higher silver coverages a $\sqrt{3}$ structure is observed on the annealed Si(111) surface. This structure has been investigated by Wilson and Chiang[78] and independently by van Loenen, Demuth, Tromp and Hamers.[79,171] Both groups obtained similar STM images, showing two maxima per unit cell arranged in a "honeycomb" pattern. Van Loenen *et al* conducted CITS measurements of the $\sqrt{3}$ Ag overlayer, reporting a surface band gap and three states associated with the Ag overlayer, one each at $\sim E_F \pm 1$ eV and one below $E_F$ - 1.5 eV. They also report a silver coverage of 0.89 $\pm$ 0.04 monolayers determined by ion scattering.[171]

The two groups propose quite different models for the Si(111)-$\sqrt{3}$ Ag overlayer. Wilson and Chiang propose a "honeycomb" model with two silver atoms per unit cell adsorbed in three fold sites on top of a terminated bulk silicon overlayer. The maxima observed in the STM images correspond to the metal atoms.

Van Loenen *et al.* propose instead an "embedded trimer" model with three silver atoms per unit cell. In this model the silicon surface double layer is missing one top layer silicon atom per unit cell, with a silver trimer embedded between the halves of the surface double layer. The observed maxima then correspond to the surface silicon atoms. They support this model with a proposal for the surface electronic structure consistent with the surface band gap and the states observed by CITS. These authors predict that a honeycomb model would give a metallic surface while the embedded trimer model is consistent with the spectroscopic data.

Wilson and Chiang conducted further experiments where they produced a surface with a mixture of $\sqrt{3}$ silver islands and 7x7 silicon regions.[77] The honeycomb model and the embedded trimer model make different predictions about the location of the unit cell

maxima relative to the silicon substrate lattice. The observed registry is consistent with the simple honeycomb model but not with the embedded trimer model or with a "missing top layer" model proposed on the basis of photoemission results. Wilson and Chiang conclude that the honeycomb model is the most likely structure, but they do not rule out more complex variants on the existing model, possibly involving additional silver atoms or more substantial reconstruction of the silicon substrate.

Samsavar *et al.*[172] have investigated silver adsorption on the silicon (100) surface. At low coverages they observe isolated maxima that they attribute to silver atoms adsorbed between dimer rows on the reconstructed surface. They propose each silver atom interacts with one of the dangling bonds on the pair of adjacent dimers. Silver atoms are observed to form short rows much more often than would occur for random site occupation, implying mobility of the silver adatoms on the silver (100) surface. At a silver coverage of 0.05 monolayers two and four atom chains were observed much more often than one, three or five atom chains. Substrate steps and defects did not appear to play a role in silver adsorption.

As the silver coverage is increased beyond a monolayer three dimensional silver crystallites start to form. Samsavar *et al.*[172] report observing Ag(110) grains with the expected 4.1 Å spacing between rows and also Ag(111) grains with a 2.9 Å hexagonal lattice corresponding to an Ag(111) 1x1 surface.

Köhler, Demuth and Hamers[173] have studied the adsorption of palladium on the Si(111)-7x7 surface at room temperature. Unlike silver, palladium does form a stable bulk silicide. When palladium is deposited at room temperature, STM images show amorphous islands with no resolved internal structure and no long range order. These islands nucleate around the silicon adatoms on one half of the unit cell, with at least 95% of the nuclei located on the faulted half of the 7x7 unit cell (see figure 11). The authors carried out a statistical analysis of island growth and volume to area ratio. From this they conclude that a stoichiometric $Pd_2Si$ layer is formed using only the silicon adatoms and top bilayer of the 7x7 surface. Steps or defects on the silicon 7x7 surface do not seem to have any special role in palladium adsorption.

Copper also forms a bulk silicide, $Cu_3Si$, but lacks long range order when adsorbed on Si(111). Tosch and Neddermeyer studied copper condensation on silicon at room temperature.[170,174] As in the case of silver, the initial stage of copper adsorption leads to triangular structures that replace the inner adatoms in the 7x7 unit cell. As the copper coverage increases the islands expand to fill one triangular half of the unit cell, usually the faulted half. A change can also be seen in some individual silicon adatoms, which seem lower in topographs after copper adsorption, unlike the silver case where metal-induced point defects were not observed. At coverages of several monolayers the surface is covered with irregularly shaped three dimensional islands with sizes of $\sim$ 100 Å.

Copper deposited at higher temperatures is known to form an incommensurate 5x5-like LEED pattern. Wilson, Chiang and Salvan[175] studied this phase after depositing a monolayer of copper on a silicon substrate at 650 ° C. They did not find a surface phase with long-range order incommensurate with the substrate, instead they saw several types of locally ordered regions irregularly fitted together. These features included approximately 5x5 arrays of bumps on the surface, strip-like regions extending for larger distances and occasional triangular depressions. Demuth *et al.*[83] investigated this 5x5-like phase in greater detail using Fourier techniques. A 2-D power spectrum of the Fourier transformed topographs showed two sets of periodic components in addition to the substrate periodicity, one at $\mathbf{q} = \mathbf{s}/5.55$ and the other at $\mathbf{t} = 0.814 \pm 0.002\ \mathbf{s}$, where $\mathbf{s}$ is the silicon substrate lattice vector. By selectively back-transforming parts of the power spectrum the irregular 5x5-like unit cells were shown to be commensurate with the silicon substrate lattice periodicity while the other components were associated with depressions and domain walls bounding the 5x5-like elements. The authors propose the strain associated with incorporating copper into the silicon lattice in the 5x5 regions is so large that the depressions and domain wall features are required to relieve these strains.

### 7.3. Non-metals on silicon

Kaiser *et al.* have produced a hydrogen terminated silicon (111) surface by chemically etching silicon in a nitrogen glove box.[176] They were not able to resolve the surface atomic structure, seeing instead flat (111) terraces with occasional steps. Spectroscopic

measurements showed an unpinned surface Fermi level with the bulk bandgap.

Tokumoto *et al.*[177] observed the effects of hydrogen adsorption on silicon (111) in ultra-high vacuum. They prepared a clean silicon (111) surface showing a 7x7 reconstruction. After exposure to the hydrogen background pressure of the vacuum chamber for several hours a (1x1) surface structure was observed in STM topographs. Thermal desorption measurements confirmed the presence of adsorbed hydrogen but showed no other impurities. The authors also report a new structure observed at greater hydrogen exposures. They suggest this may be related to a silicon hydride phase but did not give a details analysis of the structure.

Hamers, Avouris and Bozso studied the chemical reaction of $NH_3$ with the silicon (100) surface.[131] They observed changes in the STM images which they attribute primarily to hydrogen induced changes in the surface electronic structure. Ion scattering indicates sub-surface nitrogen, and comparison of UPS observations for silicon (100) reacted with hydrogen and with $NH_3$ are similar in the vicinity of the Fermi energy -- the nitrogen related states are more than 4 eV below the Fermi energy and have little effect on the STM images.

Clean silicon (100) has a dimerized 2x1 reconstruction. Filled state STM images show a single maxima per dimer corresponding to the $\pi$ bonding state, and empty state images show two maxima per dimer corresponding to the empty $\pi^*$ anti-bonding state. After reaction with $NH_3$ both filled and empty state images show two maxima per dimer. The authors interpret this image in terms of a hydrogen overlayer with one hydrogen per surface atom. The maxima correspond to the Si-H bonding and anti-bonding states. The surface dimer structure is thought to be essentially unchanged since the dimer energy is primarily associated with low lying $\sigma$ states, not with the $\pi$ bonds which are affected by hydrogen adsorption.

Avouris and Wolkow have also investigated $NH_3$ adsorption on the silicon (111) 7x7 surface.[178,73] This system is more interesting because a number of inequivalent surface sites can participate in the chemisorption reaction. Photoemission and electron energy

loss studies show $NH_3$ reacts with the silicon (111) surface to form Si-H and Si-$NH_2$ bonds. STM topographs show clear changes upon $NH_3$ adsorption. In empty state images at +0.8 eV about half the adatoms appear to be missing, and center adatoms are 3.5 times more likely to react than corner adatoms. At +3.0 eV the missing atoms are again visible although dimer than the unreacted atoms, and a similar pattern is seen in filled state images at -2eV. In filled state images at -3.0 eV the reacted adatoms are more prominent than the normal unreacted atoms. Some reacted atoms show stronger filled state maxima. These are tentatively assigned to Si-$NH_2$ bonds, while the weaker maxima are Si-H bonds.

The reaction process has been investigated using atom resolved spectroscopic measurements. Three sites are found to participate in this reaction -- the corner adatoms, adjacent to the corner holes, the remaining center adatoms, and the rest atoms, the top layer silicon atoms not bound to adatoms. The rest atom sites are found to be the most reactive. The authors explain this observation by noting that the silicon adatoms in $T_4$ sites interact to some extent with the silicon atoms in the lower half of the silicon surface double layer in addition to three silicon atoms in the top half of the surface double layer, while the rest atoms are bound only to three silicon atoms, therefore the trivalent sites are more reactive.

The center adatoms sites are found to be $\sim$ four times more reactive than corner adatoms, although less than the rest atoms. In the unreacted silicon 7x7 structure there is charge transfer from the adatoms to the rest atom states. This leads to differences in electronic structure between corner adatoms, with a single neighboring rest atom, and center adatoms with two neighboring rest atoms. However reaction of the rest atoms reverses this charge transfer and there is little spectroscopic difference between corner and center adatoms in the presence of fully reacted rest atoms.[73] The authors suggest the differences in reactivity may be associated with structural factors such as the larger strains associated with corner adatoms.

Wolkow and Avouris have also investigated $CaF_2$ overlayers on silicon (111).[179] This system is of technological interest since $CaF_2$ can form epitaxial insulating layers on

silicon, a necessary property for three dimensional electronic devices. When $CaF_2$ is adsorbed on silicon (111) at temperatures above 700 ° C two ordered structures can be observed with $(\sqrt{3}x\sqrt{3})R30°$ and 2x3 lattices. Annealing above 800 ° C, where fluorine is known to desorb, converts the 2x3 to the $\sqrt{3}$ lattice, so the authors suggest the $\sqrt{3}$ structure may contain less or no fluorine. In empty state images second layer protrusions are also seen. The 2x3 structure has a surface band gap of 2.3 eV.

As multilayers of $CaF_2$ are deposited the surface band gap rapidly approaches the bulk value of 12 eV, neverless the empty surface states can still be imaged with the STM since the conduction band is located 3 eV above the Fermi energy. Filled state imaging is not possible since the valence band is 9 eV below the Fermi energy.

Villarubia and Boland[37] have studied the silicon (111) 7x7 surface after reaction with chlorine. This is an etching reaction, and following exposure to chlorine and annealing at 470 ° C most adatoms have been removed, leaving each top layer silicon atom bound to one chlorine atom. This treatment partly removes the 7x7 structure stacking fault. Extended 1x1 domains can be observed corresponding to bulk terminated silicon, and remaining faulted and unfaulted half cells of the 7x7 overlayer are also observed. Since the adatoms are gone each half cell now shows 21 maxima corresponding to the top layer silicon atoms instead of 6 maxima due to adatoms. The faulted regions are observed to be $\sim$ 0.2Å higher than the unfaulted regions, and the authors suggest this may be a geometrical effect.

Liebsle, Samsavar and Chiang have used the STM to study the initial stages of oxidation on the silicon (111) 7x7 surface.[180] They find that defects are important in oxidation at room temperature. Perfect 7x7 unit cells show few or no changes after exposure to $\sim$ 50 L of $O_2$, while oxygen attacks sites adjacent to point defects. Defects were associated with adatoms that appear dark or missing in grey-scale topographs. When a clean silicon 7x7 surface with a moderate density of missing adatoms was exposed to oxygen at room temperature while being continuously scanned with the STM, a number of additional adatoms disappeared. Over 90% of the newly reacted adatoms were adjacent to defects or previously reacted adatoms. At larger oxygen exposure ($\sim$ 300 L) the

surface was disordered, but large area images still showed hints of 7x7 'tiling', which may indicate that the sub-surface stacking faults are not affected by room temperature oxidation.

### 7.4. Adsorbates on gallium arsenide

The chemisorption of oxygen on GaAs(110) has been studied in detail by Feenstra, Stroscio and collaborators. Chemisorption of antimony, cesium, gold and iron on GaAs(110) have also been investigated.

STM images of oxygen chemisorbed on $n$ and $p$-type GaAs(110) are quite different.[181,182,127,183] On $n$-type GaAs oxygen adsorbed at low ($\sim$ 0.003 ML) coverages produces large maxima in filled state images and large minima in empty state images. Oxygen adsorption does not appear to be associated with surface defects. The oxygen adatom is negatively charged on $n$-type GaAs, which produces a depletion zone of local band bending around each adatom. For a dopant concentration of $10^{18}$ cm$^3$ the Debye screening length is $\sim$ 50 Å, consistent with the observed local band bending. This is clearly an electronic effect since the corrugation due to the substrate lattice is superimposed on the long range band bending contribution. At larger oxygen coverages (0.05 - 0.10 ML) the average separation between adatoms is less than the screening length and localized band bending is replaced by uniform band bending across the surface.

On $p$-type GaAs(110) the STM images appear completely different. Here there is no evidence of band bending, and maxima corresponding to oxygen atoms appear as maxima in both filled and empty state images, although the empty state maxima are more prominent. The lack of band bending suggests that the oxygen adatom creates an unoccupied acceptor state. The oxygen maxima in the STM images are much better localized than in the $n$-type case, and the approximate position of the oxygen adatoms can be determined. The adatoms are located between As rows in the $[1\bar{1}1]$ direction and in As rows in the [001] direction.

Feenstra and Mårtensson investigated the structure of antimony adsorbed on GaAs(110).[184,185,186,187] At low coverages Sb atoms form small clusters on the GaAs surface. Defects do not appear to be involved in cluster nucleation. Around 0.2 ML these clusters start to grow together and form flat terraces. At around 0.7 monolayers the islands start to coalesce. As the coverage increases holes in the Sb layer fill in and some second layer Sb atoms are seen.

LEED results indicate that Sb forms a (1x1) overlayer on GaAs(110) that is basically a continuation of the bulk GaAs lattice. At large negative bias ($<$ -2 V) one maxima per unit cell is seen. Using photoemission results this maxima is assigned to the Sb atom bonded to Ga. At -1V bias two maxima per unit cell are observed, one the Ga bonded Sb atom, the other the As bonded Sb atom. The approximate atomic positions were determined by comparing the registry of the maxima in the Sb overlayer with visible patches of the clean GaAs substrate. The maxima do not directly correspond to atomic positions, however the lateral extent of the dangling bonds is $\sim$ 0.5 - 1.5 Å, so the authors assume the STM maxima are within $\pm$ 0.8 Å of the atomic positions. With this assumption the STM images are consistent with the LEED model, but not with some other models that have been suggested for this surface.

STM $I-V$ measurements show approximately the bulk band gap on both the clean GaAs(110) surface and the 1x1 Sb terraces. Gap states are seen at the edges of Sb terraces and clusters. This indicates that the observed Fermi level pinning at the Sb-GaAs interface is due to defects in the Sb overlayer, and not to the Sb overlayer itself.

Feenstra has also explored the problem of Fermi level pinning for gold adsorbed on GaAs(110).[188] At low coverages isolated gold atoms appear to be adsorbed over Ga atomic sites, appearing midway between the maxima associated with the filled As dangling bonds. Position resolved $I-V$ spectra show a gap state associated with the gold atoms 1 volt above the valence band edge, and a resonance located 0.7 volts below the valence band edge. A model is proposed for the electronic structure where the Ga $sp^3$ dangling bond is hybridized with the Au 6$s$ level, forming a donor state resonance below $E_V$ and and an acceptor state in the band gap.

First *et al.*[189] studied cesium adsorbed on GaAs(110). Cesium forms linear chain structures on GaAs even at low (0.03 ML) coverages. The simplest model of alkali metal adsorption involves charge transfer to the surface, and mutual repulsion between adatoms. This is inconsistent with the formation of linear structures. Close inspection of these features in filled state images show a zig-zag arrangement of maxima located between the As dangling bond maxima. At higher coverages triple chains are observed in addition to the zig-zag structures. The authors conclude that there is a one to one correspondence between Cs atoms and maxima, although the atom locations do not necessarily coincide with the maxima. They point out that the Cs chains may be a good system to study one dimensional atomic scale conduction.

GaAs(110) was also used as a substrate to study the electronic properties of small iron clusters.[190] Molecular beam techniques were used to deposit Fe clusters on GaAs with volumes of $\sim$ 100 to 1000 Å$^3$. $I$—$V$ measurements were made with the STM tip localized over different clusters. Clusters smaller than $\sim$ 150 Å$^3$ or $\sim$ 13 Fe atoms showed a band gap, while larger clusters showed metallic characteristics. This is consistent with an estimate based on quantum size effects that predicts the spacing between energy levels to be $\sim E_F/N$ where $N$ is the number of atoms in the cluster and $E_F$ is the bulk Fermi energy.

Spatially resolved I-V measurements were also used to measure the decay length of the induced gap states as the tip was moved away from a cluster to unperturbed regions of the GaAs(110) surface. The decay length reached a minimum of 3.4 Å at the center of the gap, and diverged at the edges of the gap as predicted for complex wave vectors in the band gap.

## 8. METALS AND OXIDES

### 8.1. Clean Metals

The structure of metal surfaces has received attention from the beginning of STM. The inventors of the technique applied it first to the observation of surfaces of gold to

study the reconstructions that some of the surfaces of this metal undergo. After these and a few other studies STM activity, as reflected in the number of scientific publications, shifted to the study of semiconductor surfaces, Si being the prime candidate due to its importance in microelectronic industry. One fundamental difference between metals and semiconductors, is the different electronic corrugation of the surface unit cell. In metals, the free nature of the electrons in the conduction bands, make the surface electronically smooth. That means that atomic resolution will be harder to obtain in metals than in semiconductors, where the electronic states near the Fermi edge arise from orbitals that form localized, covalent bonds, and give rise to much larger corrugations than in metals. While measured values of this corrugation are in the Angstrom range for Silicon, they are roughly a factor of ten smaller, i.e, tenths of Å, for metals.

There are many important areas of research in metals where the STM can provide unique answers. One of course is the structure of the clean surface. In the large scale that means defects in the form of steps, dislocations, grain boundaries etc. and the study of transport that includes diffusion, faceting and so on. In the microscopic scale, the study of reconstructions, that is small lateral and vertical displacement of surface atoms away from their projected bulk termination. Finally the study of chemisorption of atomic and molecular adsorbates and that of surface reactions is a very important area for catalysis. In the following sections we will briefly address each of these topics separately.

## 8.2. Studies of Clean Surfaces

### 8.2.1. Large Scale Structure

The study of defects on the surface of metals is important in many areas of research like metallurgy, corrosion and catalysis, where the activity of the surface is determined in many cases by the enhanced reactivity of various types of defects. In this section we will describe some of the applications of the STM that demonstrate how steps, dislocations and surface modifications are observed with examples of several authors.

Single crystals have been prepared with well defined crystallographic orientations of their surfaces as model catalysts and to study the influence of the surface structure on their chemisorption and reactivity properties. Before the advent of STM, the tool most commonly used to study the surface structure was Low Energy Electron Diffraction (LEED). However, being a diffraction technique, disorder usually escapes detection or can only be indirectly studied. Steps that are separated by terraces more than about twenty atoms wide are difficult to detect. As a result the LEED patterns of surfaces with a chemically significant number of steps can still be very sharp. The STM image illustrates the variety of step structures formed, with terraces having from a few tens to hundreds or thousands of Å width as shown in figure 12.[191]

While the presence of steps is hardly surprising, even in a carefully prepared crystal, other types of steps are the result of bulk dislocations emerging at the surface. Some of this type of defects can be uniquely observed by STM as shown in figure 13, where a close look at the emergence of a screw dislocation has been obtained.[35] This image shows a two atom height step that is formed at the point of emergence of the dislocation and splits into two monoatomic height steps to the left of the image. Beautiful images showing screw dislocations in gold films on mica were also obtained by Chidsey *et al.*[192] and Trevor *et al.*.[193]

Stepped or vicinal surfaces on metals have scarcely been studied at all up to this date with the STM in spite of the opportunities offered by the technique to study such phenomena as stability, faceting etc that are of vital interest to the understanding of the thermodynamic properties of surfaces. Our present knowledge derives from studies using mostly LEED in combination with other surface characterization techniques.[194] Among the published studies we shall mention those performed in the author's laboratory on a Au(334) surface. This is a (111) vicinal surface with 7 atom wide terraces and (100) oriented steps that were prepared in UHV and characterized by LEED and Auger spectroscopy.[195] The STM images obtained after moving the Au crystal to air revealed the presence of monoatomic steps as expected from the LEED pattern. In addition, other large scale corrugations of the surface were observed that formed large plateaus. When this surface was annealed in air at 900 K, impurities in the form of iron oxides were found on the surface in the amount of one monolayer approximately, as revealed by

Auger spectroscopy analysis. The STM images of the annealed surfaces indicated that faceting had occurred by the development of rounded structures and large (111) terraces (300 Å and more) separated by other terraces of smaller size. Clearly the deposition of a monolayer of oxide impurities on this surface changed the surface free energy to make it unstable against faceting, a phenomenon predicted by thermodynamic studies.[196]

Another vicinal gold surface was studied by Ocal *et al.*[197] These authors observed a constant terrace width (6 atoms wide) structure with variable step height of (100) orientation to accommodate the local macroscopic slope. Change in step height rather than in terrace width to accommodate the changing local slope is an unexpected and interesting observation.

As pointed above, the effect of diffusion can be directly observed by the STM by the time evolution of surface structures. A beautiful example of this is shown in the images obtained by Jacklevic *et al.*.[198] The damage resulting from the tip touching the surface, a circular depression, anneals off by filling the hole with diffusing gold atoms. There is a growing field of applications of the STM where the tip is used as a microtool to purposedly modify the surface. The structures produced can be hills, depressions and a variety of patterns that result from mechanical or electrochemical interactions. This fascinating topic however is outside the scope of the present review.

### 8.2.2. Atomic Scale Structure

The first studies on well defined metal surfaces with atomic scale resolution were performed by Binnig *et al.*[64,199] These authors studied the structure of two well known reconstructed surfaces, the Au(110) and the Au(100).

The Au(110) surface reconstructs into the 1x2 structure by alternate removal of rows of metal atoms along the [110] direction. The valley structure of this surface was demonstrated by the STM images that lend support to the missing row model just described. Other periodicities also observed include the 1x3 that consists of deeper valleys. In spite of the smoothing effect of conduction electrons, the high corrugation of this

surface made it possible to resolve the valley structure. The measured corrugation was 0.45 Å. This value compares favorably with the value of the charge density at the Fermi level calculated by Tersoff.[16,17] The corrugation on the 1x3 areas, where the valley is three layers deep was found to be 1.4 Å, in good agreement also with the calculated value.

The Au(100) surface is known to reconstruct into the 5x1 structure, which is a close packed arrangement of atoms on top of the square symmetry (100) surface. Previous LEED measurements had already confirmed this structure.[200] Because of the smoothing effect of conduction electrons, atomic resolution was not achieved but the periodicity of the reconstruction, which is 5 times the lattice spacing was clearly observed.[199] These Au surfaces were also studied by Kuk *et al.*, confirming the previous observations.[201] These authors measured also the tip radius by FIM before and after the STM experiments.[202] They found that the corrugation of the surface is a strong function of the tip cluster size. On the (110) surface for example, the corrugation was found to vary between 0.1 and 0.7 Å when the cluster size varied form 20 to 2-3 atoms. The effect of annealing and chemisorption on the mass transport that is necessary to change from the 1x1 to the 1x2 structure on this gold surface was also studied. Upon exposure to oxygen, the authors found mainly 1x1 areas with small terraces of 1x2 reconstruction. Upon annealing to 700 K, 10 K below the phase transition to the 1x1 structure, the STM images revealed that 1x2 domains with small size were still present, while the half order spots had already disappeared completely from the LEED pattern.

The Pt(100) reconstructed surface that was studied by Behm *et al.*,[203] exhibits an hexagonal overlayer similar to that present on the Au(100) surface. The measured corrugation of this reconstructed surface was 0.4 Å. The two possible domains, rotated 90 degrees, were observed on different adjacent terraces separated by one atom height. These authors studied also the effect of CO adsorption, since it is known that this process removes the reconstruction and restores the substrate to its bulk square symmetry. Since the hexagonal overlayer requires 20% more Pt atoms that the square substrate, mass transport should occur during the transformation as was indeed demonstrated by the experiments.

The compact (111) surfaces of metals deserve special mention due to recent observations of atomic resolution. The (111) surface of gold films evaporated on mica was studied by STM by Hallmark *et al.*.[31] These authors could resolve the individual gold atoms with a corrugation of 0.3 Å. These authors could also observe a larger unit cell reconstruction with ($\sqrt{3}$x23) periodicity as a small undulation (0.15 Å amplitude) of the surface topography with this periodicity.[204] Other studies of the Au(111) surface confirmed the observation of atomic corrugation.[205] Also recently Al(111)[32] and Cu(111)[206] have been imaged with atomic resolution. The observation of atomic resolution on compact (111) metal surfaces is somewhat of a surprise, in particularly the large values of the observed corrugation of a few tenths of Å. One possibility to understand these observations is the operation of compressive forces by the tip that would magnify the corrugation by elastically deforming the tip-surface system. The possibility that elastic interactions play an important role in determining the value of the corrugations has been pointed out by Winterlin *et al.*,[32] rather than electronic effects such as surface states, as proposed by Hallmark *et al.*.[31]

Epitaxial growth of metals and oxides on metals is also an area that is receiving increased attention. Dovek *et al.*[207] have studied the growth of Ag on Au(111). They observed the layer by layer growth of Ag. At submonolayer coverages they observed the formation of fingerlike rows that were locked to the Au(111) (px$\sqrt{3}$). At one monolayer the surface reconstruction was removed.

Another metallic system studied recently includes the quasicrystal of $Al_{65}Co_{20}Cu15$.[208] The surface of this material forms a decagonal structure with a pentagon-center- decorated pentagonal quasilattice. This along with the amorphous systems described below constitute one good example of opportunities offered by the application of STM to the study of the real space structure of materials.

### 8.3. Metal Oxide Surfaces

The application of STM to studies of oxide surfaces is limited to the cases where the oxide is or can be made conductive. In many cases this is accomplished by the

introduction of defects like oxygen vacancies in the bulk. Alternative routes include the growth of atomically thin films on metallic substrates.

Some of the earliest investigations focused on the surfaces of high temperature superconducting oxides (LaSrCuO). Although in most cases atomic resolution images were not obtained, several authors have used the STM either in tunneling or with the tip in actual contact with the surface to measure the superconducting gap at low temperatures.[209,210] In later studies imaging in air and at room temperature was accomplished by Kirk *et al.*[211] in the $a-b$ planes of $Bi_2(Ca,Sr)_3Cu_2O_{8+x}$ single crystals. A superstructure with a periodicity of 27.2 $\pm$0.7 Å was observed in agreement with findings using TEM. Steps of 16 Å height were also observed that would indicate cleavage between the $Bi_2O_2$ planes. No atomic structures could be resolved however, within the large 27 Å unit cells. Shih *et al.*[212] also performed studies of this crystal plane in UHV and achieved atomic resolution along the perovskite axis with a corrugation close to 0.3 Å. These authors resolved also a lateral sinusoidal modulation consisting of small lateral displacements with an amplitude of 1.1$\pm$0.2 Å from compression to expansion and a periodicity of 4.75 units along the $a$ direction or roughly 23.7 Å. Based on the IPES (inverse photoemission) results the authors suggest that at the low bias voltages used by Kirk *et al.*, mostly the O atoms were imaged, while at the larger bias voltages used in their work Bi-related features were observed. The spectroscopic studies suggests also that the Bi-O surface layer is most likely nonmetallic.

Another HTC superconductor was imaged by Liang *et al.*[213] who studied $(Pb_xBi_{2-x})_2Sr_2CaCu_2O_8$ cleaved in situ in an argon filled glove box. The images exhibit a one-dimensional superstructure for Pb concentrations below 0.3. For x = 0 the periodicity is 24.6 Å. Interestingly a careful analysis indicated a variation of the periodicity between 22.5 and 26.7 Å. At x = 0.3 the periodicity increased to 32.1 Å. The increase is explained by the fewer O atoms required for Pb that has a valency of 2 instead of 3 for Bi. For x = 0.7 no regular superstructure was observed. Atomic resolution images revealed that the addition of Pb causes distortions to the superlattice, with several extra atomic sites visible in the images. The atomic corrugation observed is attributed by the authors to O sites rather than to Bi sites because inverse photoemission data indicate that the states near the Fermi level are predominantly O $2p-\pi$ in origin.

Tungsten bronzes like $Rb_{0.05}WO_3$ were studied by Norton *et al.*[214] These materials are conducting (they have a small band gap) and form layered structures. Structurally they consist of octahedral building blocks of $WO_6$ linked by the corners. The Rb atoms are dopants and occupy sites within hexagonal channels that form chains along the *b* axis. The channel structure was imaged by the authors who found a strong corrugation along the chains of about 2 Å and a spacing of 7 Å. However the double chain that is observed in TEM was not evident in the STM topographs.

$TiO_2$ has received considerable attention in view of its importance in electrochemical studies involving light processes. It has a band gap of 3 eV and when stoichiometric it is quite insulating. However by heating the crystal in hydrogen, oxygen vacancies are introduced that make the crystal conductive enough for STM experiments. The (110) surface was studied by Sakamaki *et al.* in air.[215] These authors measured the band gap using the spectroscopic capabilities of the microscope and found it to be close to 1.6 eV. The lower value is explained by surface states including those due to hydroxide species. A similar study was performed on the (001) surface by Fan *et al.*[216] A high resolution image was obtained by these authors that show the 4.6 Å periodicity over small patches of the surface. The electronic structure of the surface was studied with several features found in the $\frac{dI}{dV}/\frac{I}{V}$ curves that were interpreted as surface states associated with O vacancies. More recently the (110) surface was studied again in UHV by Rohrer *et al.*[217] The defect planes created by the accumulation of O vacancies (*CS* planes) form ordered structures known as Magnelli phases. The images obtained show the presence of rows along the $[\bar{1}11]$ direction with a separation of 8.5 Å and a corrugation of 1 Å. Along the rows a periodicity is observed of 3.4 Å and a corrugation of 0.2 Å. Steps are also observed with heights of 2.2 Å, smaller than the 3.25 Å expected from the distance between (110) planes. Since the images were obtained at positive sample bias, they correspond to empty states that are associated with Ti. The authors explain the observations by assuming that the rows correspond to (121) *CS* planes intersecting the surface. The corrugation of 1 Å is largely associated to Ti states which reduce the geometric corrugation of 1.6 Å.

A recent study of $TiO_2$ mono and multilayers on Rh(111) in UHV was published recently also by Wang *et al.*[218] The authors showed that the growth of the oxide is two dimensional. No atomic resolution however was obtained with corrugation larger than the 0.3 Å experimental noise level. In the monolayer regime, the exposure of the sample to CO removes some of the O and produces $Ti^{+3}$. The empty density of states images revealed a higher corrugation at the perimeter of the 20-30 Å size islands. The authors interpret their observations by considering the high concentration of the reduced Ti species at the island perimeter that provide a higher local conductivity on account of the $Ti^{+3}$ states near the Fermi level.

Other oxides are receiving attention as well including ZnO that has been studied by Rohrer *et al.*[219] The images of polycrystalline ZnO in UHV revealed the presence of monoatomic steps and facets. Tunneling spectroscopy was used to identify individual grain and surface impurities. No atomic resolution was achieved in this study however.

It is clear that the STM and in particular its spectroscopic capabilities can help greatly to understand the geometry and electronic structure of oxide surfaces as these first studies show. This will be of tremendous importance in many areas including catalysis where metal- metal oxide support interactions are often invoked to explain unexpected enhancement of catalytic activity.

## 9. CHEMISORPTION ON METALS

Chemisorption of atoms and molecules on metal surfaces, is an extremely important area in surface chemistry since it provides a basis to understand heterogeneous catalysis, corrosion, friction and adhesion etc. Many different systems have been studied to this date with the STM, including small atomic adsorbates and large organic molecules. The combination of such techniques as STM, LEED and vibration spectroscopies (HREELS and IR) is promising to provide a new impetus to these type of studies. Moreover, the possibility to use the STM in a pressure range that is outside the range of applicability of the other techniques can help bridge the gap between the surface science studies that require UHV and the practical chemical conditions where pressures in excess of one

atmosphere are currently used.

In studies of chemisorption by STM a point that must be kept in mind is the poorly understood meaning of the vertical Z coordinate in the images that determines the appearance of an adsorbed atom in the STM topographs. We have already pointed out that the topographs are in fact contours of equal charge density in the vicinity of the Fermi level. Clearly electron donors and electron acceptor adsorbates might be expected to give different results. If the adsorbate decreases the density of states near the Fermi level, it might appear as a depression instead of a bump, since the tip will have to move closer to the surface to compensate for the loss of total tunneling probability. This problem has been analyzed by Lang, as discussed above in section 2.3. Doyen *et al.*[220] and have calculated the tunneling current over an adsorbed oxygen atom on Al(111) and Ni(100). They found that while there is no dependence of the corrugation of the constant current profile as a function of tip to surface distance in the Al case, on Ni the contour can change sign with oxygen appearing as a hole instead of a bump for small tip distances. With these considerations in mind it is clear that the absolute height of the adsorbate atoms as measured by the tip displacements does not necessarily measure the height of the adsorbate atoms at the position of their nuclei. It should be used therefore with some caution, while the XY distances have a more direct interpretation in terms of projected unit cell distances. In the following we will describe several examples of chemisorbed systems.

### 9.1. Atomic adsorbates

The first study of a chemisorbed systems was performed by Baro *et al.* who studied oxygen on Ni(110).[221] Oxygen forms a 2x1 structure with the same periodicity as the substrate along the [100] direction and with twice its value along the compact [110] direction. They found also that the oxygen form rows in domains separated by 5 lattice spacings and consist of a variable number of rows. The thick domain walls account for the 0.35 coverage value instead of the expected 0.5 if no domain walls were present.

Other O chemisorption studies have been performed recently on Cu(110) by Chua *et al.*.[222] , Phys. Rev. The authors find that O nucleates on terraces forming long isolated chains while Cu atoms diffuse in from step edges and terrace patches to form added rows. Jensen *et al.* studied the dynamics of O induced reconstruction of Cu(100).[223] They found that the $(2\sqrt{2}x2\sqrt{2})R45^\circ$ structure is formed by removal of every fourth [001] row of Cu atoms, resulting in the formation of Cu islands.

Another chemisorbed system studied was H/Ni(110) by Kuk *et al.*.[33] These authors showed that the reconstruction of the Ni surface induced by the adsorption of H can be resolved and appears as tetramers of Ni atoms formed as a result of combined row pairing and missing [001] rows. The structure can be described as a 5x2 structure. In addition numerous antiphase boundaries were observed separating small domains where the local arrangement is 1x2 and explains the reports of streaked LEED patterns. This is an example of a situation where the effects due to the adsorption (displacement of the Ni atoms) are imaged while there is not a direct signature in the images of the location of the adsorbate H atoms. A similar observation of adsorbate induced substrate changes occurs in the case of CO on Pt(001), as mentioned above,[203] and CO on Pt(110) that induces the 1x2 to 1x1 surface structural transformation.[224]

One of the most common chemisorbed species is carbon. It is the most prevalent contaminant found in UHV studies of single crystals surfaces, particularly after heating the samples. It appears as a result of hydrocarbon contamination and decomposition or as a segregation product. It is also the end product of many surface reactions involving adsorbed hydrocarbons and forms graphitic domains that are blamed for the loss of catalytic activity (catalyst deactivation or coking). These surface layers were imaged in the authors laboratory and are illustrated in the image of figure 14. The layer, obtained after heating a Pt(111) crystal in UHV, has an average thickness of one monolayer. Its graphitic structure is clearly shown by the STM. In this current image a honeycomb structure is formed with the higher tunnel current delineating the C chemical bonds in the graphite ring. It is also interesting to notice the asymmetric height of the alternating C atoms that is reminiscent of the situation in bulk HOPG samples. Since the prevalent interpretation of this effect involves the interaction between two carbon layers, it is possible that more than one layer of graphite is present in our Pt(111) substrate.

Sulfur chemisorption on the Mo(001) surface was studied in the authors laboratory in UHV using LEED and Auger spectroscopy.[34] The Mo crystal saturated with one monolayer of S was then moved to an STM operating in air and studied in both the topographic and barrier height modes. The stability of the atomic structure of this S monolayer in one atmosphere of air is a remarkable and unexpected observation. It illustrates dramatically the passivating nature of the S overlayer as a result of the slow kinetic processes of Mo oxidation and provide hope for future studies of the nature of other catalytically important surfaces in reaction conditions of high pressure. In the present case the images show the presence of two domains of 1x2 and 2x1 periodicity. While the significance of the Z scale is unclear both in the topographic and barrier height mode images it is apparent that the compact saturation layer of S has a unit cell where the two S atoms appear as similar. In spite of the slow kinetics of the oxidation processes given enough time large oxidation patches form on the surface, presumably nucleating in S pinholes in the layer. The oxidized condition of the sample was verified by subsequent examination by XPS.[225]

Two more S chemisorption systems have been studied recently. One is S/Cu studied by Rousset *et al.*, and the other the S/Re(0001) studied in the authors laboratory. When S was adsorbed on vicinal Cu(100) surfaces, two structures were observed that interacted with the steps in different ways and caused their restructuring. The 2x2 structure is formed in conjunction with [110] oriented steps while the c(2x4) is formed in conjunction with [130] steps. The S/Re system exhibits similar passivating properties as the S/Mo system and the ordered $2\sqrt{3}x2\sqrt{3}$ R30° saturation structure could be imaged in air at atmospheric pressure or in vacuum. This is an interesting system since it provides an instance of a complex structure that would be difficult to determine by LEED dynamical calculations. Indeed the unit cell contains 12 Re substrate atoms and 6 S adsorbate atoms. The image of figure 15 illustrates the atomic structure of the S monolayer as revealed by the STM. The repeating unit is a ring of 6 sulfur atoms. In the image we can observe a step separating two terraces in the lower left corner. Also, the presence of various types of antiphase domain boundaries is apparent, as indicated by the arrows in the figure. At high magnification the S ring is resolved into its six atoms and shows a threefold symmetry. It is a reflection of the underlying substrate symmetry.

At lower coverages, S forms a variety of structures that depend on the coverage. These structures could not be observed in air since they do not passivate the surface. They were prepared and studied in UHV. At 0.25 monolayers a 2x2 structure was formed. For a coverage between 0.3 and 0.4 a $(3\sqrt{3}x3\sqrt{3})R30^\circ$ pattern is observed. At 0.4 to 0.5 monolayers a $\begin{pmatrix} 3 & 1 \\ 1 & 3 \end{pmatrix}$ structure is formed and finally at saturation, the above mentioned $(2\sqrt{3}x2\sqrt{3})R30^\circ$ pattern is formed. All of these structures could be imaged by the STM either in topographic or current modes. In addition a new structure not observed by LEED previously was observed in small patches on the surface, coexisting with the 2x2. Its unit cell is of $c(\sqrt{3}x5)$Rect symmetry and contains two S atoms. Another surprising result that emerged from these studies, is the observation of coalescence of S atoms into trimers when the local coverage is higher than 0.25. The trimers form in two orientations and when their number saturates, order in the $(3\sqrt{3}x3\sqrt{3})R30^\circ$ structure. This observation shows that three-body forces are in some cases like the present one, important enough to determine the structure of the overlayer. The image in figure 16 shows one of these structures..226,227

The example of S on Re(0001) just discussed is a good illustration of the power of the STM technique. Defects, steps and domain boundaries can be directly observed in a unique way. New minority structures are revealed that might have important roles in catalytic reactions. The very complicated structures formed above 0.25 monolayers would have been very difficult to observe with other structural techniques, including dynamic I-V LEED measurements. The formation of the coalesced structures (trimers, tetramers and hexagons) is a new observation that has gone unsuspected in the previous studies of this system.

Iodine forms passivating monolayers on Pt(111) as S does on Mo and Re. Schardt *et al.*[228] produced several structures of I on a Pt(111) surface in air that could be imaged in air and in an electrochemical cell. The images obtained in air reveal the presence of two structures, a $\sqrt{7}x\sqrt{7}$ at a coverage of 3/7 and a 3x3 at a coverage of 4/9. This last structure appears in two different packing arrangements one forming a symmetric hexagonal arrangement and the other an asymmetric arrangement. The different adsorption sites of the I atoms were revealed by their different apparent height in the STM

topographs.

### 9.2. Molecular adsorption

Molecular adsorbates were first imaged by Ohtani *et al.* These authors studied the coadsorption system of CO and benzene on Rh(111)[81] Previous LEED studies by Van Hove *et al.*[229] had shown that depending on the relative amount of CO, different ordered structures could be formed, while in the absence of CO ordering of the benzene layer was found to be more difficult. The image of figure 17 show the benzene molecules as three-fold symmetric rings, while coadsorbed CO was imaged as very small bumps between the benzene molecules. Site assignment to the adsorbate molecules was then done by extrapolation of a lattice from known points starting at step defects.

Large molecules like copper phthalocyanine have been studied by several authors.[230,206] Lippel *et al.*, succeeded in producing ordered layers of the molecule in Cu single crystal substrates. Isolated molecules could also be imaged and their internal structure analyzed.

## 10. AMORPHOUS MATERIALS

The surfaces of amorphous materials seems one obvious class of systems where real space imaging could contribute in a unique way to our understanding of their structure. In spite of this, very few studies have been performed where atomic scale structural information has been obtained. One possible reason for this is the fact that small random corrugations due to the disordered atoms cannot easely be distinguished from noise, particularly when the amplitude of the corrugation is close to that of the noise. This situation is likely to improve as better instruments become available. One of the first atomic scale studies of an amorphous material was performed in the author's laboratory. Hard coatings of sputtered C on magnetic recording media were studied. These studies revealed that small ( approx. 15 Å) domains exist with a graphitic structure, surrounded by disordered regions where irregular C rings and pentagonal rings were present.[231] Figure 18 shows and example of these structures. In another study also in our laboratory,

the growth of plasma deposited films of hydrogenated amorphous C on graphite and on silicon was performed. The formation of amorphous clusters of C on the ordered graphite substrate was observed. The ordered substrate provided a reference for the disordered structure in the C clusters as shown in figure 19.[232]

## 11. CONCLUSION

It is clear that the field of surface chemistry is in a process of rapid change thanks to the new STM techniques. This change is not only of a quantitative or incremental nature but of a qualitative nature as well. In addition to studies of surface structures in real space, new areas of research open up due to the possibility to study complicated structures, defects, steps and disordered surfaces. Other exciting possibilities arise from the use of STM to study catalyst surfaces in controlled environments of gas composition, pressure and temperature.[233]

Another field in the process of rapid growth that we have left practically untouched in this review is that of solid-liquid interfaces, which the STM can easely explore. This is an exceedingly important area in electrochemistry and important results are already emerging from various laboratories.

Another class of adsorbate/substrate systems that is receiving considerable attention is the study of large organic molecules adsorbed on a variety of substrates. A few of these were mentioned in the section devoted to graphite. It may soon be possible to get atomic scale information on polymer and biomolecular surfaces. These systems are still in a phase of exploration since strong tip-surface interactions are present here that have more profound effects on the weakly bound and poorly conductive layers than in the chemisorbed atomic systems discussed above.

The authors are convinced that in the future, the STM, in combination with other scanning probe microscopy techniques, will foster a new era in surface physics and chemistry.

## 12. ACKNOWLEDGEMENTS

This work was supported by the Director, Office of Energy Research, Basic Energy Science, Materials Division of the US Department of Energy under contract number DE-AC03-76SF00098.

## FIGURE CAPTIONS

1) Schematic drawing of the STM set-up. A cylindrical piezoelectric tube supports a metallic tip, a few Angstroms over the surface of the sample. The outer surface of this tube is divided into four electrodes. Voltages applied to these electrodes cause bending and length changes of the tube that are used to scan the tip over the surface. The tunnel current between the tip and the surface is maintained constant by means of an electronic feedback circuit.

2) Electronic energy diagram in the STM experiment. The tip Fermi level is maintained at an energy eV above that of the sample by means of an applied bias. A net flow of electrons from the tip to the surface is produced by tunneling through the approximately trapezoidal barrier in the vacuum gap region. The barrier height is closely related to the work function of the tip and sample materials.

3) Effect of the tip-surface forces in graphite. The 1000x1000 Å images show a large terrace on the left side and a smaller $\sim$ 150 Å flake on the right in (a), and a second image of the same area (b) showing displacement to the left. The horizontal discontinuities in the image of the flake are due to smaller displacements along the fast scan (horizontal) direction during scanning.

4) Effect of shear forces between tip and surface is illustrated in this atomic scale (20 x 20 Å) image obtained by placing the tip on top of a small (approximately 100 Å size) flake of graphite. The distortion of the hexagonal cell is due to the tip dragging the flake along the x and y directions during scanning.

5) Measured apparent tunneling barrier height between a Pt-Rh tip and a clean Rh(111) surface in UHV as a function of gap resistance. The barrier height was measured by modulating the tip-surface distance and using Eq. 2 in the text. For comparison we show the curve predicted by Lang for a jellium substrate after conversion of the abscissa distance scale into gap resistance.[66]

6) Top view of (5x5), (7x7), and (9x9) structures according to the dimer- adatom-stacking fault model (DAS). From Becker et al.[118]

7) Topographs of the clean Si (7x7). (a) Filled states obtained at a sample bias of -1.5 V and empty states (b), obtained at a sample bias of +1.5 V. The stacking fault and the differences between corner and center adatoms are visible. After Avouris *et al.*[73]

8) A 260x300 Å image of the Ge (111) surface showing regions of c(2x8), (2x2), and c(4x2) symmetry. Two atomic steps are seen across the image obtained by tunneling into empty states at 1.0 V bias. From Becker *et al.*[62]

9) Topographic image showing epitaxial Si islands grown on Si(111) at 330 ° C. Notice the absence of islands near the step edge as well as the growth of second layers on top of small islands. The arrow indicates an island with a partially complete (3x3) structure. From Kohler *et al.*[119]

10) A filled state STM image of coexisting indium $\sqrt{31}$x$\sqrt{31}$ and $\sqrt{3}$x$\sqrt{3}$ overlayers on silicon (111). (Courtesy of A. Baski, J. Nogami and C. F. Quate, Stanford University.)

11) (a) STM topograph fo a 115x95 Å area of a Si(111)-(7x7) substrate with 0.25-ML of Pd. Pd is seen to nucleate only on the faulted half of the (7x7) unit cell. (b) DAS model indicating the location of the Pd- silicide cluster. (c) Cut through the long diagonal of the (7x7) unit cell. From Kohler *et al.*[173]

12) Half micron size image of Re(0001) covered with a saturation layer of S. The surface is composed of multitude of large (1000 Å width) and small (100 Å width) terraces separated by mono- and multiple- atom height steps.

13) Image of an emerging screw dislocation in a Re(0001) single crystal covered with a monolayer of S. The emergence point is the starting of a two-atom height step at

the center of the image. Later on the step splits into two monoatomic steps.

14) A graphitic layer of C on Pt(111) is shown in this 10 x 10 Å current image. The C layer was produced by heating the Pt crystal in UHV to high temperature (> 1300 K) and cooling to room temperature. The average C coverage according to Auger spectroscopy performed in situ is between one and two monolayers.

15) (a) 130x170 Å topographic image of the $2\sqrt{3}$x$2\sqrt{3}$ R30° structure formed by S on the Re(0001). The surface unit cell consists of S hexagonal units. A step separates two terraces and produces the blurred region of the image. Notice also numerous defects and domain boundaries. (b) Schematic model of the $2\sqrt{3}$x$2\sqrt{3}$ R30° lattice.

16) (a) STM current image of a 68 Å square $\begin{pmatrix} 3 & 1 \\ 1 & 3 \end{pmatrix}$ region (coverage 0.5 ML), showing diamond-like sulfur tetramers with their long diagonal pointing in the $[1\bar{1}00]$ direction. The long diagonal is the only mirror plane, as can be seen from the non-uniform intensity distribution within the tetramer.
(b) Schematic model of the $\begin{pmatrix} 3 & 1 \\ 1 & 3 \end{pmatrix}$ lattice.

17) (a) Three-dimensional view of a topographic image of the Rh(111)-(3x3)- C6H6 + 2CO. At bias voltages below 0.5 V, a nominally 3-fold structure with a depression at the center is observed. The lobes appear to be localized between rather than over the underlying metal atoms. From Ohtani *et al.*[81] (b)Schematic of the same structure as determined by LEED crystallography. From Van Hove *et al.*[234]

18) Current images from sputtered films of C on magnetic recording media. Top image shows a small domain of graphitic rings forming patches 10 to 15 Å in diameter. Carbon in surrounding regions (bottom image) forms irregular structures with hints of pentagonal rings and other arrangements. From Marchon *et al.*[231]

19) 200x200 Å topographic image of amorphous C clusters deposited on a graphite surface by plasma CVD. The graphite sample was located at the powered electrode.

The regular periodicity of the graphite substrate is visible between the amorphous clusters. The height of the C clusters is $\sim$ 15 Å. From Vandentop *et al.*[232]

**References**


1. G. Binnig, H. Rohrer, Ch. Gerber, and E. Weibel, *Physical Review Letters*, vol. 49, p. 57, 1982.
2. R. D. Young, J. Ward, and F. Scire, *Physical Review Letters*, vol. 27, p. 922, 1971.
3. J. A. Golovchenko, *Science*, vol. 232, p. 48, 1986.
4. P.K. Hansma and J. Tersoff, *Journal of Applied Physics*, vol. 61, p. 1, 1987.
5. G. Binnig and H. Rohrer, *Reviews of Modern Physics*, vol. 59, p. 615, 1987.
6. J. E. Demuth, U. K. Koehler, and R. J. Hamers, *Journal of Microscopy*, vol. 152, p. 299, 1988.
7. G. Binnig, C. F. Quate, and Ch. Gerber, *Physcial Review Letters*, vol. 56, p. 930, 1986.
8. T. R. Albrecht and C. F. Quate, *Journal of Applied Physics*, vol. 62, p. 2599, 1987.
9. R. G. Miller and P. J. Bryant, *Journal of Vacuum Science and Technology A*, vol. 7, p. 2879, 1989.
10. S. A. C. Gould, B. Drake, C. B. Prater, A. L. Weisenhorn, S. Manne, H. G. Hansma, P. K. Hansma, J. Masse, M. Longmire, V. Elings, B. Dixon Northern, B. Mukergee, C. M. Peterson, W. Stoeckenius, T. R. Albrecht, and C. F. Quate, *Journal of Vacuum Science and Technology A*, vol. 8, p. to be published, 1990.
11. C. B. Duke, in *Tunneling in Solids*, Academic Press, New York, 1969.
12. P. K. Hansma, ed., *Tunneling Spectroscopy: Capabilities, Applications and New Techniques,* Plenum Press, New York, 1982.
13. A. Messiah, *Quantum Mechanics,* pp. 369-410, John Wiley and Sons, New York, 1958.
14. J. G. Simmons, *Journal of Applied Physics*, vol. 34, p. 1973, 1963.
15. J. A. Stroscio, R. M. Feenstra, and A. P. Fein, *Physical Review Letters*, vol. 57, p. 2579, 1986.
16. J. Tersoff and D. R. Hamann, *Physical Review Letters*, vol. 50, p. 1998, 1983.
17. J. Tersoff and D. R. Hamann, *Physical Review B*, vol. 31, p. 805, 1985.
18. J. Tersoff, *Physical Review Letters*, vol. 57, p. 440, 1986.

19. J. Tersoff, *Physical Review B*, vol. 39, p. 1052, 1989.

20. N. D. Lang, *Physical Review Letters*, vol. 55, p. 230, 1985.

21. N. D. Lang, *IBM Journal of Research and Development*, vol. 30, p. 374, 1986.

22. N. D. Lang, *Physical Review Letters*, vol. 56, p. 1164, 1986.

23. N. D. Lang, *Physical Review Letters*, vol. 58, p. 45, 1987.

24. N. D. Lang, *Physical Review B*, vol. 34, p. 5947, 1986.

25. N. D. Lang, *Physical Review B*, vol. 37, p. 10395, 1988.

26. P. Bedrossian, Robert D. Meade, K. Mortensen, D. M. Chen, J. A. Golovchenko, and David Vanderbilt, *Physical Review Letters*, vol. 63, p. 1257, 1989.

27. I.-W. Lyo, Efthimios Kaxiras, and Ph. Avouris, *Physical Review Letters*, vol. 63, p. 1257, 1989.

28. R. M. Feenstra, J. A. Stroscio, J. Tersoff, and A. P. Fein, *Physical Review Letters*, vol. 58, p. 1192, 1987.

29. M. A. Van Hove, S. W. Wang, D. F. Ogletree, and G. A. Somorjai, *Advances in Quantum Chemistry*, vol. 20, p. 1, 1989.

30. D. J. Chadi, *Ultramicroscopy*, vol. 31, p. 1, 1989.

31. V. M. Hallmark, S. Chiang, J. F. Rabolt, J. D. Swalen, and R.J. Wilson, *Physical Review Letters*, vol. 59, p. 2329, 1988.

32. J. Wintterlin, J. Wiechers, H. Brune, T. Gritsch, H. Höfer, and J. Behm, *Physcial Review Letters*, vol. 62, p. 59, 1989.

33. Y. Kuk, P. J. Silverman, and H. Q. Nguyen, *Physical Review Letters*, vol. 59, p. 1452, 1987.

34. B. Marchon, P. Bernhardt, M.E. Bussell, G.A. Somorjai, M. Salmeron, and W. Siekhaus, *Physical Review Letters*, vol. 60, p. 1166, 1988.

35. D. F. Ogletree, C. Ocal, B. Marchon, M. B. Salmeron, G. A. Somorjai, T. P. Beebe, and W. Siekhaus, *Journal of Vacuum Science and Technology A*, vol. 8, p. 297, 1990.

36. S. Rousset, S. Gauthier, O. Siboulet, W. Sacks, M. Belin, and J. Klein, *Physical Review Letters*, vol. 63, p. 1265, 1989.

37. J. S. Villarubia and John J. Boland, *Physical Review Letters*, vol. 63, p. 306, 1989.

38. C. Julian Chen, "Origin of Atomic resolution on metal surfaces in scanning tunneling microscopy," *to be published*, 1990.

39. C. Julian Chen, "Theory of High Resolution Tunneling Microscopy: The Role of Non-Spherical Tip States," *to be published.*

40. C. Julian Chen, *Journal of Vacuum Science and Technology A*, vol. 6, p. 319, 1988.

41. Y. V. Sharvin, *Zh. Eksp. Teor. Fiz.*, vol. 48, p. 984, 1965.

42. A. G. M. Jansen, A. P. van Gelder, and P. Wyder, *Journal of Physics*, vol. C 13, p. 6073, 1980.

43. V. Kalmeyer and R. B. Laughlin, *Physical Review*, vol. B 35, p. 9805, 1987.

44. J. K. Gimzewski and R. Möller, *Physical Review B*, vol. 36, p. 1284, 1987.

45. S. Ciraci and Inder P. Batra, *Physical Review*, vol. B 36, p. 6194, 1987.

46. E. Tekman and S. Ciraci, *Physical Review*, vol. B 40, p. 10286, 1989.

47. S. Ciraci and E. Tekman, *Physical Review*, vol. B 40, p. 11969, 1989.

48. S. Ciraci, A. Baratoff, and Inder P. Batra, *Physical Review*, vol. B 41, p. 2763, 1990.

49. G. Boato, P. Cantini, and R. Tatarek, *Physical Review Letters*, vol. 40, p. 887, 1978.

50. J. M. Soler, A. M. Baró, N. Garcia, and H. Rohrer, *Physical Review Letters*, vol. 57, p. 444, 1986.

51. J.B. Pethica, *Physical Review Letters*, vol. 57, p. 3235, 1986.

52. H. Yamada, T. Fuji, and K. Nakayama, *Journal of Vacuum Science and Technology*, vol. A 6, p. 293, 1988.

53. C. M. Mate, R. Erlandsson, G. M. McClelland, and S. Chaing, *Surface Science*, vol. 208, p. 473, 1989.

54. H. J. Mamin, E. Ganz, D. W. Abraham, R. E. Thomson, and J. Clarke, *Physical Review*, vol. B 34, p. 9015, 1986.

55. M. B. Salmeron, D. F. Ogletree, C. Ocal, H.-C. Wang, G. Neubauer, W. Kolbe, and G. Meyers, *Journal of Vacuum Science and Technology A*, vol. 9 STM V proceedings, 1991 .

56. H. F. Hess, R. B. Robinson, R. C. Dynes, J. M. Valles, Jr., and J. V. Waszczak, *Physical Review Letters*, vol. 62, p. 214, 1989.

57. R. Möller, A. Esslinger, and B. Koslowski, *Journal of Vacuum Science and Technology A*, vol. 8, p. to be published, 1990.

58. J. H. Coombs, J. K. Gimzewski, B. Reihl, J. K. Sass, and R. R. Schlittler, *Journal of Microscopy*, vol. 152, p. 325, 1988.

59. G. Binnig, H. Rohrer, Ch. Gerber, and E. Weibel, *Physical Review Letters*, vol. 50, p. 120, 1983.

60. R. S. Becker, J. A. Golovchenko, D. R. Hamann, and B. S. Schwartzentruber, *Physical Review Letters*, vol. 55, p. 2032, 1985.

61. R. J. Hamers, R. M. Tromp, and J. E. Demuth, *Physical Review Letters*, vol. 56, p. 1972, 1986.

62. R. S. Becker, B. S. Schwartzentruber, J. S. Vickers, and T. Klitsner, *Physical Review B*, vol. 39, p. 1633, 1989.

63. A. Bryant, D. P. E. Smith, and C. F. Quate, *Applied Physics Letters*, vol. 48, p. 832, 1986.

64. G. Binnig, H. Rohrer, C. Gerber, and E. Weibel, *Surface Science*, vol. 131, p. L379, 1983.

65. H.-C. Wang, D. F. Ogletree, and M. B. Salmeron, *Journal of Vacuum Science and Technology A*, vol. 9 STM V proceedings, 1991 .

66. N. D. Lang, *Physical Review B*, vol. 36, p. 8173, 1987.

67. R. M. Feenstra and J. A. Stroscio, *Journal of Vacuum Science and Technology B*, vol. 5, p. 923, 1987.

68. M. Weimer, J. Kramer, and J. D. Baldeschwieler, *Physical Review B*, vol. 39, p. 5572, 1989.

69. Y. Kuk and P. J. Silverman, *Review of Scientific Instruments*, vol. 60, p. 165, 1989.

70. R. S. Becker, J. A. Golovchenko, and B. S. Schwartzentruber, *Physical Review Letters*, vol. 55, p. 987, 1985.

71. G. Binnig, K. H. Frank, H. Fuchs, N. Garciá, B. Reihl, H. Rohrer, F. Salvan, and A. R. Williams, *Physical Review Letters*, vol. 55, p. 991, 1985.

72. W. J. Kaiser and R. C. Jaklevic, *IBM Journal of Research and Development*, vol. 30, p. 411, 1986.

73. Ph. Avouris and R. Wolkow, *Physical Review B*, vol. 39, p. 5091, 1989.

74. J. A. Stroscio, R. M. Feenstra, and A. P. Fein, *Journal of Vacuum Science and Technology A*, vol. 5, p. 838, 1987.

75. Th. Berghaus, A. Brodde, H. Neddermeyer, and St. Tosch, *Surface Science*, vol. 193, p. 235, 1988.

76. Th. Berghaus, A. Brodde, H. Neddermeyer, and St. Tosch, *Journal of Vacuum Science and Technology A*, vol. 6, p. 483, 1988.

77. R. J. Wilson and S. Chiang, *Physical Review Letters*, vol. 59, p. 2329, 1987.

78. R. J. Wilson and S. Chiang, *Physical Review Letters*, vol. 58, p. 369, 1987.

79. E. J. van Loenen, J. E. Demuth, R. M. Tromp, and R. J. Hamers, *Physical Review Letters*, vol. 58, p. 373, 1987.

80. J. Nogami, Sang-il Park, and C. F. Quate, *Journal of Vacuum Science and Technology B*, vol. 6, p. 1479, 1988.

81. H. Ohtani, R.J. Wilson, S. Chiang, and C.M. Mate, *Physical Review Letters*, vol. 60, p. 2398, 1988.

82. R. E. Thomson, U. Walter, E. Ganz, J. Clarke, A. Zettel, P. Rauch, and F. J. DiSalvo, *Physical Review*, vol. B 38, p. 10734, 1988.

83. J. E. Demuth, U. K. Koehler, R. J. Hamers, and P. Kaplan, *Physical Review Letters*, vol. 62, p. 641, 1989.

84. J. E. Demuth, U. K. Koehler, and R. J. Hamers, *Journal of Vacuum Science and Technology A*, vol. 8, p. to be published, 1990.

85. M. G. Lagally, R. Kariotis, B. S. Schwartzentruber, and Y.-K. Mo, *Ultramicroscopy*, vol. 31, p. 87, 1989.

86. A. P. Fein, J. R. Kirtley, and R. M. Feenstra, *Review of Scientific Instruments*, vol. 58, p. 1806, 1987.

87. J. W. Lyding, S. Skala, J. S. Hubacek, R. Brockenbrough, and G. Gammie, *Review of Scientific Instruments*, vol. 59, p. 1897, 1988.

88. R. S. Robinson, *Journal of Microscopy*, vol. 152, p. 541, 1988.

89. C. C. Williams and H. K. Wickramasinghe, *Applied Physics Letters*, vol. 49, p. 1587, 1986.

90. U. Dührig, D. W. Pohl, and F. Rohner, *Journal of Applied Physics*, vol. 59, p. 3318, 1986.

91. D. W. Pohl, *IBM Journal of Research and Development*, vol. 30, p. 417, 1986.

92. O. Nishikawa, M. Tomitori, and A. Minakuchi, *Surface Science*, vol. 181, p. 210, 1987.

93. S. Okayama, M. Komuro, W. Mizutani, H. Tokumoto, M. Okano, K. Shimizu, Y. Kobayashi, F. Matsumoto, S. Wakiyama, M. Shigeno, F. Sakai, S. Fujiwara, O. Kitamura, M. Ono, and K. Kajimura, *Journal of Vacuum Science and Technology A*, vol. 6, p. 440, 1988.

94. Y. Kuk, P. J. Silverman, and H. Q. Nguyen, *Journal of Vacuum Science and Technology A*, vol. 6, p. 524, 1988.

95. T. Hashizumi, I. Kamiya, Y. Hasegawa, N. Sano, T. Sakurai, and H. W. Pickering, *Journal of Microscopy*, vol. 152, p. 347, 1988.

96. I. P. Batra, N. Garcia, H. Rohrer, H. Salemink, E. Stoll, and S. Ciraci, *Surface Science*, vol. 181, p. 126, 1987.

97. D. Tománek, S. G. Louie, H. J. Mamin, D. W. Abraham, R. E. Thomson, E. Ganz, and J. Clarke, *Physical Review B*, vol. 35, p. 7790, 1987.

98. R. J. Colton, S. M. Baker, R. J. Driscoll, M. G. Youngquist, J. D. Baldeschwieler, and W. J. Kaiser, *Journal of Vacuum Science and Technology*, vol. A 6, p. 349, 1988.

99. H. A. Mizes, Sang-il Park, and W. A. Harrison, *Physical Review B*, vol. 36, p. 4491, 1987.

100. E. Ganz, K. Sattler, and J. Clarke, *Journal of Vacuum Science and Technology*, vol. A 6, p. 419, 1988.

101. D. Sarid, T. Henson, L. S. Bell, and C. J. Sandroff, *Journal of Vacuum Science and Technology*, vol. A 6, p. 424, 1988.

102. J. S. Foster, J. E. Frommer, and P. C. Arnett, *Nature*, vol. 331, p. 324, 1988.

103. J. S. Foster and J. E. Frommer, *Nature*, vol. 333, p. 542, 1988.

104. J. K. Spong, H. A. Mizes, L. J. LaComb Jr, M. M Dovek, J. E. Frommer, and J. S. Foster, *Nature*, vol. 338, p. 137, 1989.

105. D. P. E. Smith, M. D. Kirk, and C. F. Quate, *Journal of Chemical Physics*, vol. 86, p. 6034, 1987.

106. A. M. Baro, R. Miranda, J. Alaman, N. Garcia, G. Binnig, H. Rohrer, Ch. Gerber, and J. L. Carrascosa, *Nature*, vol. 315, p. 253, 1985.

107. G. Travaglini, H. Rohrer, M. Amrein, and H. Gross, *Surface Science*, vol. 181, p. 380, 1987.

108. S. M. Lindsay, T. Thundat, and L. Nagahara, *J. Microscopy*, vol. 152, p. 213, 1989.

109. T. P. Beebe, T. E. Wilson, D. F. Ogletree, J. E. Katz, R. Balhorn, M. B. Salmeron, and W. Siekhaus, *Science*, vol. 243, p. 370, 1989.

110. M. B. Salmeron, T. P. Beebe, J. Odriozola, T. E. Wilson, D. F. Ogletree, and W. Siekhaus, *Journal of Vacuum Science and Technology A*, vol. 8, p. 635, 1990.

111. R. Gluckenberger, Thomas Hartmann, Winfried Wiegräbe, and W. Baumeister, "The Scanning Tunneling Microscope in Biology," in *STM Vol 2: Further Applications and Related Scanning Techniques*, ed. H.-J. Günterodt and R. Wiesendanger, Springer Verlag, Berlin, 1990.

112. A. Stemmer and A. Engel, *Ultramicroscopy*, vol. 30, p. 263, 1989.

113. C. Wang, B. Giambattista, C. G. Slough, R. V. Coleman, and M. A. Subarmanian, to be published.

114. C. G. Slough, W. W. McNairy, and R. V. Coleman, *Physical Review*, vol. B 34, p. 994, 1986.

115. R. S. Becker, J. A. Golovchenko, and B. S. Schwartzentruber, *Physical Review Letters*, vol. 54, p. 2678, 1985.

116. K. Takayanagi, Y. Tanishiro, M. Takahashi, and S. Takahashi, *Journal of Vacuum Science and Technology A*, vol. 3, p. 1502, 1985.

117. R. S. Becker, J. A. Golovchenko, and B. S. Schwartzentruber, *Physical Review B*, vol. 32, p. 8455, 1985.

118. R. S. Becker, J. A. Golovchenko, G. S. Higashi, and B. S. Schwartzentruber, *Physical Review Letters*, vol. 57, p. 1020, 1986.

119. U. K. Köhler, J. E. Demuth, and R. J. Hamers, *Journal of Vacuum Science and Technology A*, vol. 7, p. 2860, 1989.

120. J. E. Northrup, *Physical Review Letters*, vol. 57, p. 154, 1986.

121. J. E. Griffith, J. A. Kubby, P. E. Wierenga, R. S. Becker, and J. S. Vickers, *Journal of Vacuum Science and Technology A*, vol. 6, p. 493, 1988.

122. Th. Berghaus, A. Brodde, H. Neddermeyer, and St. Tosch, *Surface Science*, vol. 184, p. 273, 1987.

123. K. C. Pandey, *Physical Review Letters*, vol. 47, p. 1913, 1981.

124. R. M. Feenstra, W. A. Thompson, and A. P. Fein, *Physical Review Letters*, vol. 56, p. 608, 1986.

125. R. M. Feenstra, W. A. Thompson, and A. P. Fein, *Journal of Vacuum Science and Technology*, vol. 4, p. 1315, 1986.

126. R. M. Feenstra, J. A. Stroscio, and A. P. Fein, *Surface Science*, vol. 181, p. 295, 1987.

127. J. A. Stroscio, R. M. Feenstra, D. M. Newns, and A. P. Fein, *Journal of Vacuum Science and Technology A*, vol. 6, p. 499, 1988.

128. M. D. Pashley, K. W. Haberern, and W. Friday, *Journal of Vacuum Science and Technology A*, vol. 6, p. 488, 1988.

129. R. M. Tromp, R. J. Hamers, and J. E. Demuth, *Physical Review Letters*, vol. 55, p. 1303, 1985.

130. R. J. Hamers, R. M. Tromp, and J. E. Demuth, *Physical Review B*, vol. 34, p. 5343, 1986.

131. R. J. Hamers, Ph. Avouris, and F. Bozso, *Physical Review Letters*, vol. 59, p. 2071, 1987.

132. R. J. Hamers and U. K. Köhler, *Journal of Vacuum Science and Technology A*, vol. 7, p. 2854, 1989.

133. H. Niehus, U. K. Köler, M. Copel, and J. E. Demuth, *Journal of Microscopy*, vol. 152, p. 735, 1988.

134. J. A. Martin, D. E. Savage, W. Moritz, and M. G. Lagally, *Physical Review Letters*, vol. 56, p. 1936, 1986.

135. J. E. Griffith, J. A. Kubby, P. E. Wierenga, R. S. Becker, and J. S. Vickers, *Physical Review B*, vol. 36, p. 6079, 1987.

136. Th. Berghaus, A. Brodde, H. Neddermeyer, and St. Tosch, *Journal of Vacuum Science and Technology A*, vol. 6, p. 478, 1988.

137. A. J. Hoeven, D. Dijkkamp, E. J. Van Loenen, and P. J. G. M. Van Hooft, *Surface Science*, vol. 211, p. 165, 1989.

138. E. J. Van Loenen, D. Dijkkamp, and A. J. Hoeven, *Journal of Microscopy* , vol. 152, p. 487, 1988.

139. H. Neddermeyer and St. Tosch, *Physical Review B*, vol. 38, p. 5784, 1988.

140. H. Neddermeyer and St. Tosch, *Journal of Microscopy*, vol. 152, p. 149, 1988.

141. R. M. Feenstra and A. P. Fein, *Physical Review B*, vol. 32, p. 1394, 1985.

142. M. D. Pashley, K. W. Haberern, W. Friday, J. M. Woodall, and P. D. Kirchner, *Physical Review Letters*, vol. 60, p. 2176, 1988.

143. M. D. Pashley, K. W. Haberern, and J. M. Woodall, *Journal of Vacuum Science and Technology B*, vol. 6, p. 1468, 1988.

144. R. S. Becker, J. A. Golovchenko, E. G. McRae, and B. S. Schwartzentruber, *Physical Review Letters*, vol. 55, p. 2028, 1985.

145. R. M. Feenstra and J. A. Stroscio, *Physical Review Letters*, vol. 59, p. 2173, 1987.

146. P. E. Wierenga, J. A. Kubby, and J. E. Griffith, *Physical Review Letters*, vol. 59, p. 2169, 1987.

147. B. S. Schwartzentruber, Y.-K. Mo, M. B. Webb, and M. G. Lagally, *Journal of Vacuum Science and Technology A*, vol. 7, p. 2901, 1989.

148. R. J. Hamers, U. K. Köhler, and J. E. Demuth, *Ultramicroscopy*, vol. 31, p. 10, 1989.

149. A. J. Hoeven, J. M. Lenssinck, D. Dijkkamp, E. J. van Loenen, and J. Dieleman, *Physical Review Letters*, vol. 63, p. 1830, 1989.

150. Y.-K. Mo, B. S. Schwartzentruber, R. Kariotis, M. B. Webb, and M. G. Lagally, *Physical Review Letters*, vol. 63, p. 2393, 1989.

151. J. E. Northrup, *Physical Review Letters*, vol. 53, p. 683, 1984.

152. J. M. Nicholls, P. Mårtensson, G. V. Hanson, and J. E. Northrup, *Physical Review B*, vol. 32, p. 1333, 1985.

153. J. Nogami, Sang-il Park, and C. F. Quate, *Physical Review B*, vol. 36, p. 6221, 1987.

154. J. Nogami, Sang-il Park, and C. F. Quate, *Surface Science*, vol. 203, p. L631, 1988.

155. Sang-il Park, J. Nogami, and C. F. Quate, *Journal of Microscopy*, vol. 152, p. 727, 1988.

156. R. J. Hamers and J. E. Demuth, *Journal of Vacuum Science and Technology A*, vol. 6, p. 512, 1988.

157. R. J. Hamers, *Journal of Vacuum Science and Technology B*, vol. 6, p. 1462, 1988.

158. R. J. Hamers, *Physical Review B*, vol. 40, p. 1657, 1989.

159. J. Zegenhagen, J. R. Patel, Paul Freeland, D. M. Chen, J. A. Golovchenko, P. Bedrossian, and J. Northrup, *Physical Review B*, vol. 39, p. 1298, 1989.

160. R. J. Hamers and J. E. Demuth, *Physical Review Letters*, vol. 60, p. 2527, 1988.

161. Ph. Dumas, F. Thibaudau, and F. Salvan, *Journal of Microscopy*, vol. 152, p. 751, 1988.

162. F. Thibaudau, Ph. Dumas, Ph. Matheiz, A. Humbert, D. Satti, and F. Salvan, *Surface Science*, vol. 211/212, p. 748, 1988.

163. R. S. Becker, B. S. Schwartzentruber, J. S. Vickers, M. S. Hybertsen, and S. G. Louie, *Physical Review Letters*, vol. 60, p. 116, 1988.

164. J. R. Patel, J. A. Golovchenko, P. E. Freeland, and H.-J. Gossmann, *Physical Review B*, vol. 36, p. 7715, 1987.

165. M. Copel, R. M. Tromp, and U. K. Köhler, *Physical Review B*, vol. 37, p. 10756, 1988.

166. R. S. Becker, T. Klitsner, and J. S. Vickers, *Journal of Microscopy*, vol. 152, p. 157, 1988.

167. R. J. Wilson and S. Chiang, *Physical Review Letters*, vol. 58, p. 2575, 1987.

168. Ph. Dumas, A. Humbert, G. Mathieu, P. Mathiez, C. Mouttet, R. Rolland, F. Salvan, and F. Thibaudau, *Journal of Vacuum Science and Technology A*, vol. 6, p.

517, 1988.

169. St. Tosch and H. Neddermeyer, *Physical Review Letters*, vol. 61, p. 349, 1988.

170. St. Tosch and H. Neddermeyer, *Journal of Microscopy*, vol. 152, p. 415, 1988.

171. J. E. Demuth, E. J. van Loenen, R. M. Tromp, and R. J. Hamers, *Journal of Vacuum Science and Technology B*, vol. 6, p. 18, 1988.

172. A. Samsavar, E. S. Hirshhorn, F. M. Leibsle, and T.-C. Chiang, *Physical Review Letters*, vol. 63, p. 2830, 1989.

173. U. K. Köhler, J. E. Demuth, and R. J. Hamers, *Physical Review Letters*, vol. 60, p. 2499, 1988.

174. St. Tosch and H. Neddermeyer, *Surface Science*, vol. 211/212, p. 133, 1989.

175. R. J. Wilson, S. Chiang, and F. Salvan, *Physical Review B*, vol. 38, p. 12696, 1988.

176. W. J. Kaiser, L. D. Bell, M. H. Hecht, and F. J. Grunthaner, *Journal of Vacuum Science and Technology A*, vol. 6, p. 519, 1988.

177. Hiroshi Tokumoto, Kazushi Miki, Hiroshi Murakami, Naotake Morita, Hiroshi Bando, Akira Sakai, Shigeru Wakiyama, Masatoshi Ono, and Koji Kajimura, *Journal of Microscopy*, vol. 152, p. 743, 1988.

178. Ph. Avouris and R. Wolkow, *Physical Review Letters*, vol. 60, p. 1049, 1988.

179. R. Wolkow and Ph. Avouris, *Journal of Microscopy*, vol. 152, p. 167, 1988.

180. F. M. Leibsle, A. Samsavar, and T.-C. Chiang, *Physical Review B*, vol. 38, p. 5780, 1988.

181. J. A. Stroscio, R. M. Feenstra, and A. P. Fein, *Physical Review Letters*, vol. 58, p. 1688, 1987.

182. J. A. Stroscio, R. M. Feenstra, and A. P. Fein, *Physical Review B*, vol. 36, p. 7718, 1987.

183. J. A. Stroscio and R. M. Feenstra, *Journal of Vacuum Science and Technology B*, vol. 6, p. 1472, 1988.

184. R. M. Feenstra and P. Mårtenssen, *Physical Review Letters*, vol. 61, p. 447, 1988.

185. P. Mårtenssen and R. M. Feenstra, *Journal of Microscopy*, vol. 6, p. 761, 1988.

186. P. Mårtenssen and R. M. Feenstra, *Physical Review B*, vol. 39, p. 7744, 1989.

187. C. K. Shih, R. M. Feenstra, and P. Mårtensson, *Journal of Vacuum Science and Technology*, vol. A 8, p. 3379, 1990.

188. R. M. Feenstra, *Physical Review Letters*, vol. 63, p. 1412, 1989.

189. P. N. First, R. A. Dragoset, J. A. Stroscio, R. J. Celotta, and R. M. Feenstra, *Journal of Vacuum Science and Technology A*, vol. 7, p. 2868, 1989.

190. P. N. First, J. A. Stroscio, R. A. Dragoset, D. T. Pierce, and R. J. Celotta, *Physical Review Letters*, vol. 63, p. 1416, 1989.

191. B. Marchon, D. F. Ogletree, M. Salmeron, and W. Siekhaus, *Journal of Vacuum Science and Technology*, vol. A 6, p. 531, 1988.

192. C. E. D. Chidsey, D. N. Loiacono, T. Sleator, and S. Nakahara, *Surface Science*, vol. 200, p. 45, 1988.

193. D. J. Trevor, C. E. D. Chidsey, and D. N. Loiacono, *Physical Review Letters*, vol. 62, p. 929, 1989.

194. G. A. Somorjai, *Chemistry in Two Dimensions: Surfaces,* Cornell University Press, Ithaca, New York, 1981.

195. M. Salmeron, B. Marchon, S. Ferrer, and D. S. Kaufman, *Physical Review*, vol. B 34, p. 3036, 1987.

196. N. Cabrera, *Symposium on Properties of Surfaces,* Publication 340, American Society for Testing and Materials, Philadelphia, 1962.

197. C. Ocal, A. L. Vazquez de Parga, J. Alvarez, and S. Ferrer, *J. of Microscopy*, vol. 152, p. 697, 1989.

198. R. C. Jaklevic and L. Elie, *Physical Review Letters*, vol. 60, p. 120, 1988.

199. G. Binnig, H. Rohrer, Ch. Gerber, and E. Stoll, *144*, p. 321, 1984.

200. M. A. Van Hove, R. J. Koestner, P. C. Stair, J. P. Bibérian, L. L. Kesmodel, I. Bartos, and G. A. Somorjai, *Surface Science*, vol. 103, p. 218, 1981.

201. Y. Kuk, P. J. Silverman, and F. M. Chua, *Journal of Microscopy*, vol. 152, p. 449, 1988.

202. Y. Kuk and P. J. Silverman, *Applied Physics Letters*, vol. 48, p. 1597, 1986.

203. R. J. Behm, W. Hosler, E. Ritter, and G. Binnig, *Physical Review Letters*, vol. 56, p. 228, 1986.

204. Ch. Woll, S. Chiang, R. J. Wilson, and P. H. Lippel, *Physical Review*, vol. B 39, p. 7988, 1989.

205. J. V. Barth, H. Brune, G. Ertl, and R. J. Behm, to be published.

206. P. H. Lippel, R. J. Wilson, M. D. Miller, Ch. Woll, and S. Chiang, *Physical Review Letters*, vol. 62, p. 171, 1989.

207. M. M. Dovek, C. A. Lang, J. Nogami, and C. F. Quate, *Physical Review*, vol. B 40, p. 11 973, 1989.

208. A. Refik Kortan, R. S. Becker, F. A. Thiel, and H. S. Chen, *Physical Review Letters*, vol. 64, p. 200, 1990.

209. J. R. Kirtley, C. C. Tsuei, Sung I. Park, C. C. Chi, J. Rozen, and M. W. Shafer, *Physical Review*, vol. B 35, p. 7216, 1987.

210. S. Pan, K. W. Ng, and A. L. de Lozanne, *Physical Review*, vol. B 35, p. 7220, 1987.

211. M. D. Kirk, C. B. Eom, B. Oh, S. R. Spielman, M. R. Beasley, A. Kapitulnik, T. H. Geballe, and C. F. Quate, *Applied Physics Letters*, vol. 52, p. 2071, 1988.

212. C. K. Shih, R. M. Feenstra, J. R. Kirtley, and G. V. Chandrashekhar, *Physical Review*, vol. B 40, p. 2682, 1989.

213. X. Liang, Z. Zhang, Y. L. Wang, and C. M. Lieber, *Science*, vol. 248, p. 1211, 1990.

214. M. L. Norton, J. G. Mantovani, and R. J. Warmack, *Journal of Vacuum Science and Technology*, vol. A 7, p. 2898, 1989.

215. K. Sakamaki, K. Itoh, A. Fujishima, and Y. Gohshi, *Journal of Vacuum Science and Technology*, vol. A 8, p. 614, 1990.

216. F.-R. F. Fan and A. J. Bard, *Journal of Physical Chemistry*, vol. 94, p. 3761, 1990.

217. G. S. Rohrer, V. E. Henrich, and D. A. Bonnell, *Science*, vol. 250, p. 1239, 1990.

218. H.-C. Wang, D. F. Ogletree, and M. Salmeron, *Journal of Vacuum Science and Technology*, vol. A 9, p. 853, 1990.

219. G. S. Rohrer and D. A. Bonnell, *Journal of the American Ceramic Society*, vol. 73, p. 3026, 1990.

220. G. Doyen, D. Drakova, E. Kopatzki, and R. J. Behm, *Journal of Vacuum Science and Technology*, vol. A 6, p. 327, 1988.

221. A. M. Baro, G. Binnig, H. Rohrer, Ch. Gerber, E. Stoll, A. Baratoff, and F. Salvan, *52*, p. 1304, 1984.

222. F. M. Chua, Y. Kuk, and P. J. Silverman, *Physical Review Letters*, vol. 63, p. 386, 1989.

223. F. Jensen, F. Besenbacher, E. Laegsgaard, and I. Stensgaard, *preprint*, to be published 1990.

224. T. Gritsch, D. Coulman, R. J. Behm, G. Ertl, and Physical Review Letters, 63, p. 1086, 1989.

225. B. Marchon, M. E. Bussell, D. F. Ogletree, G. A. Somorjai, M. Salmeron, and W. Siekhaus, *Journal of Microscopy*, vol. 152, p. 427, 1989.

226. R. Q. Hwang, D. M. Zeglinski, A. Lopez Vazquez-de-Parga, D. F. Ogletree, G. A. Somorjai, and M. B. Salmeron, *Physical Review Letters*, (submitted).

227. D. F. Ogletree, R. Q. Hwang, D. M. Zeglinski, A. Lopez Vazquez-de-Parga, G. A. Somorjai, and M. B. Salmeron, *Journal of Vacuum Science and Technology A*, vol. 9 STM V proceedings, 1991 .

228. Bruce C. Schardt, Shueu-Lin Yau, and Frank Rinaldi, *Science*, vol. 243, p. 1050, 1989.

229. H. Ohtani, M. A. van Hove, G. A. Somorjai, and Journal of Chemical Physics, 92, p. 3974, 1988.

230. J. K. Gimzewski, E. Stoll, and R. R. Schlittler, *Surface Science*, vol. 181, p. 267, 1987.

231. B. Marchon, M. Salmeron, and W. Siekhaus, *Physical Review*, vol. B 39, p. 12 907, 1989.

232. G. J. Vandentop, P. A. P. Nascente, M. Kawasaki, D. F. Ogletree, G. A. Somorjai, and M. Salmeron, *Journal of Vacuum Science and Technology*, in press.

233. M. Salmeron, *unpublished results.*

234. M. A. Van Hove, R. F. Lin, G. A. Blackman, and G. A. Somorjai, *Acta Crystallographica B*, vol. 43, p. 368, 1987.

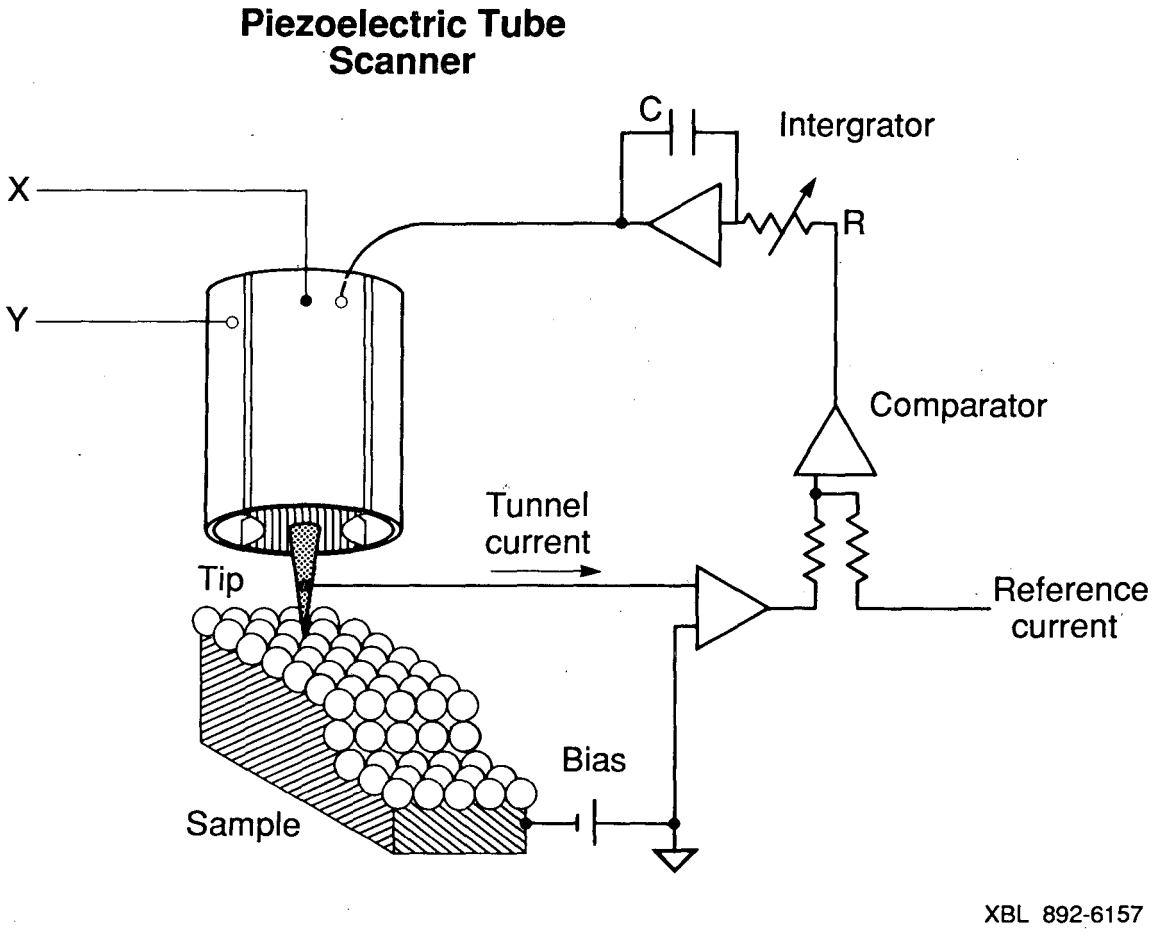
Piezoelectric Tube Scanner
C
Intergrator
X
R
Y
Comparator
Tunnel current
Tip
Reference current
Bias
Sample
XBL 892-6157

Figure 1

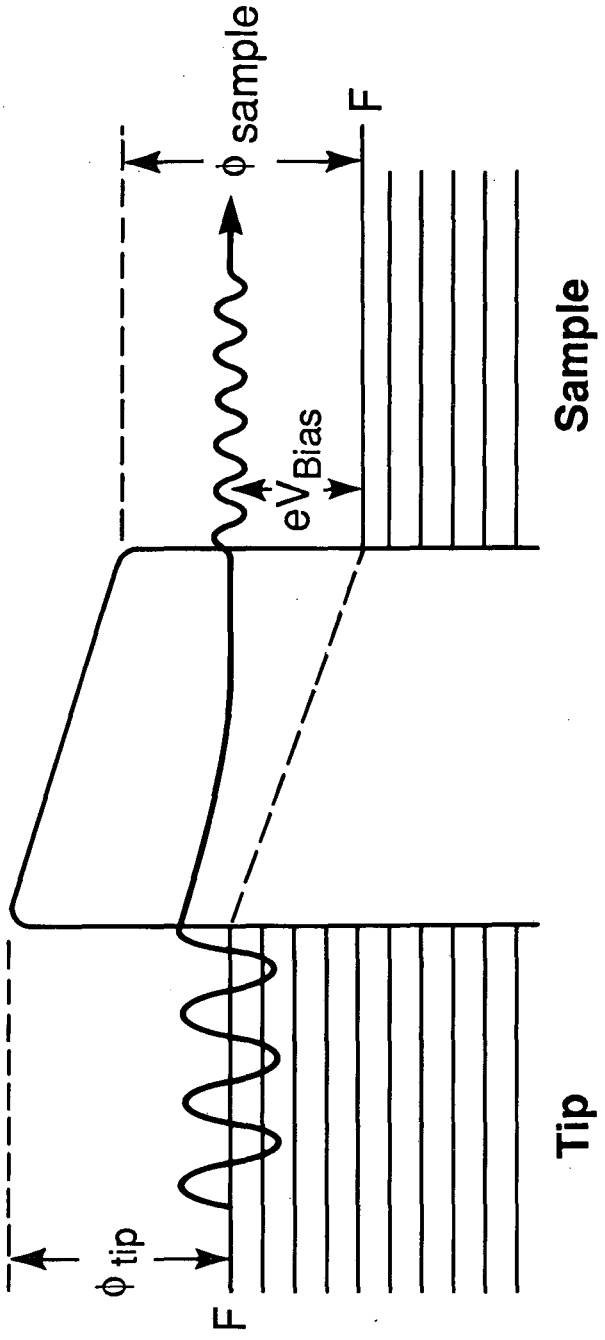


XBL 892-6155

Figure 2

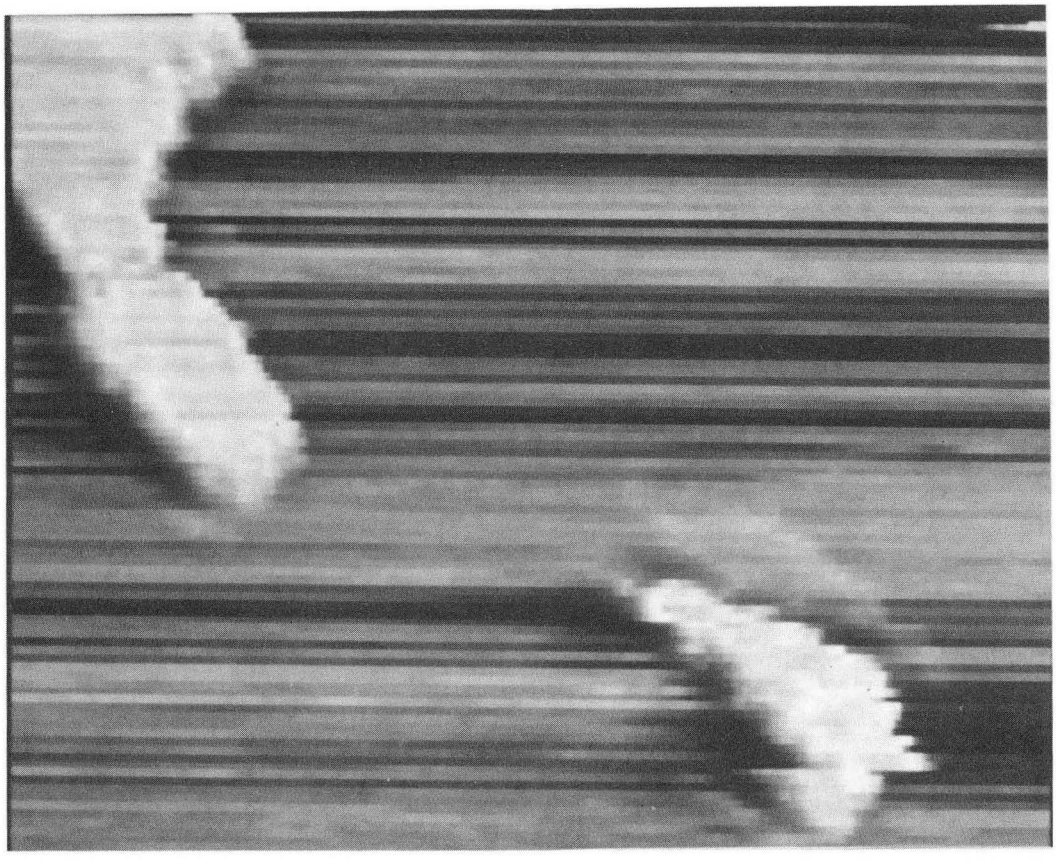

XBB 896-5168

Figure 3a

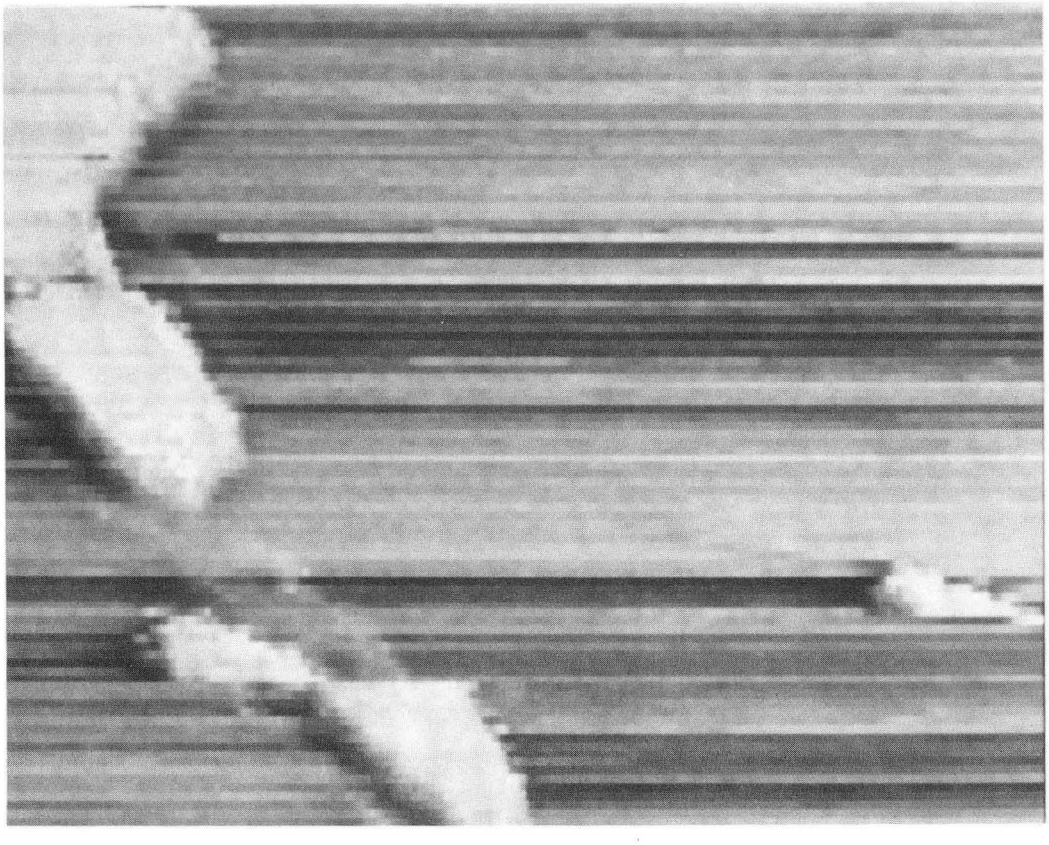

XBB 896-5169

Figure 3b

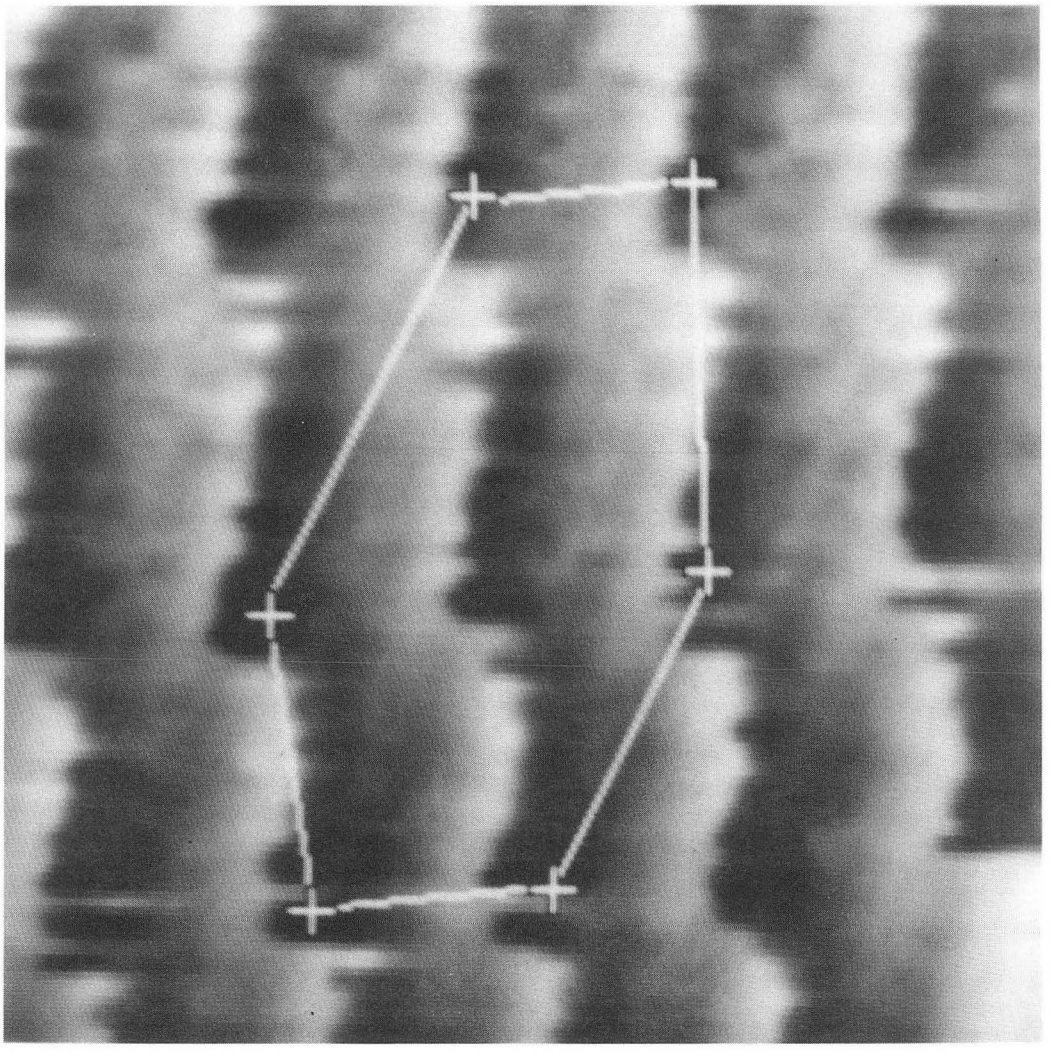

XBB 896 5171

Figure 4

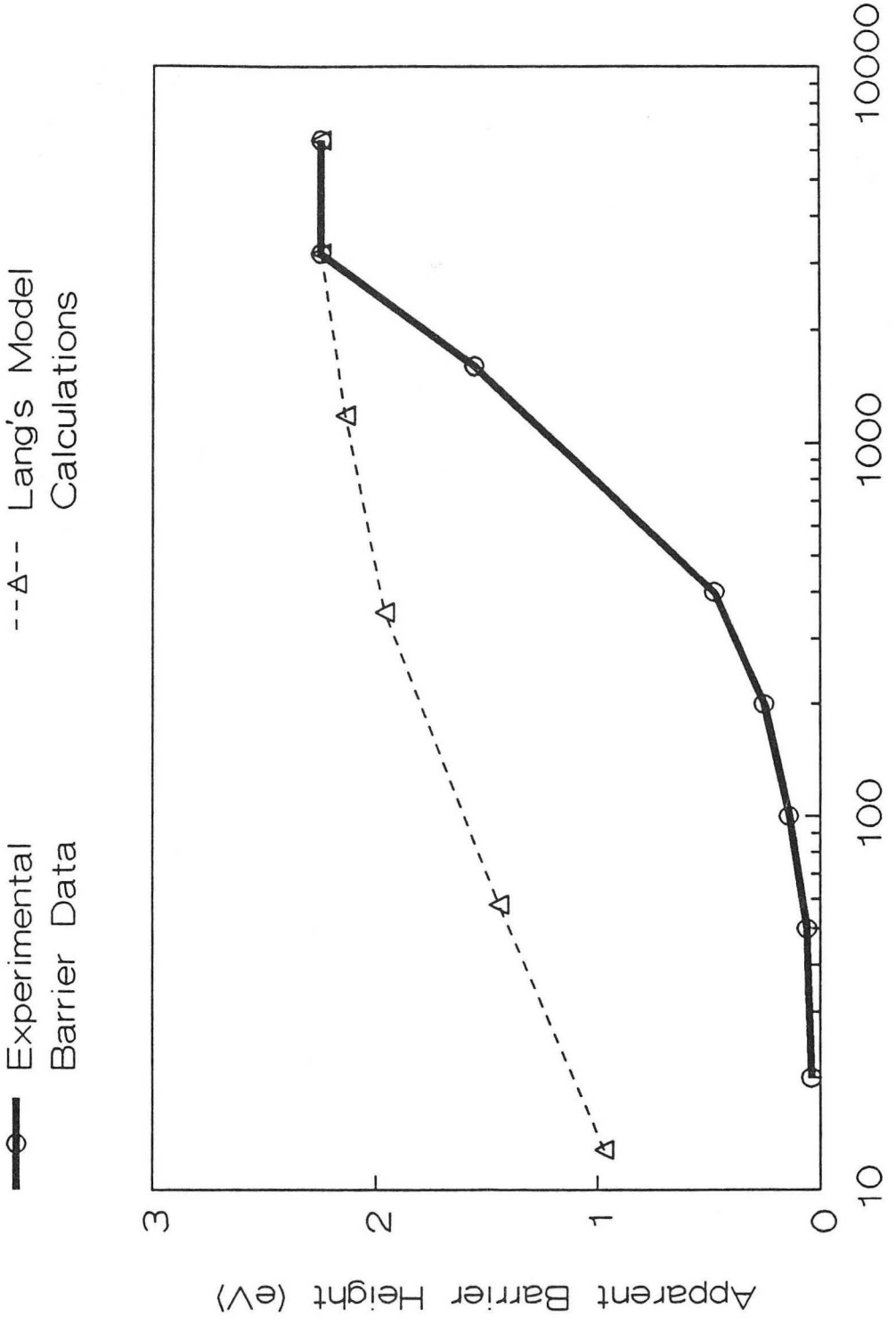


XBL 9010-3326

Figure 5

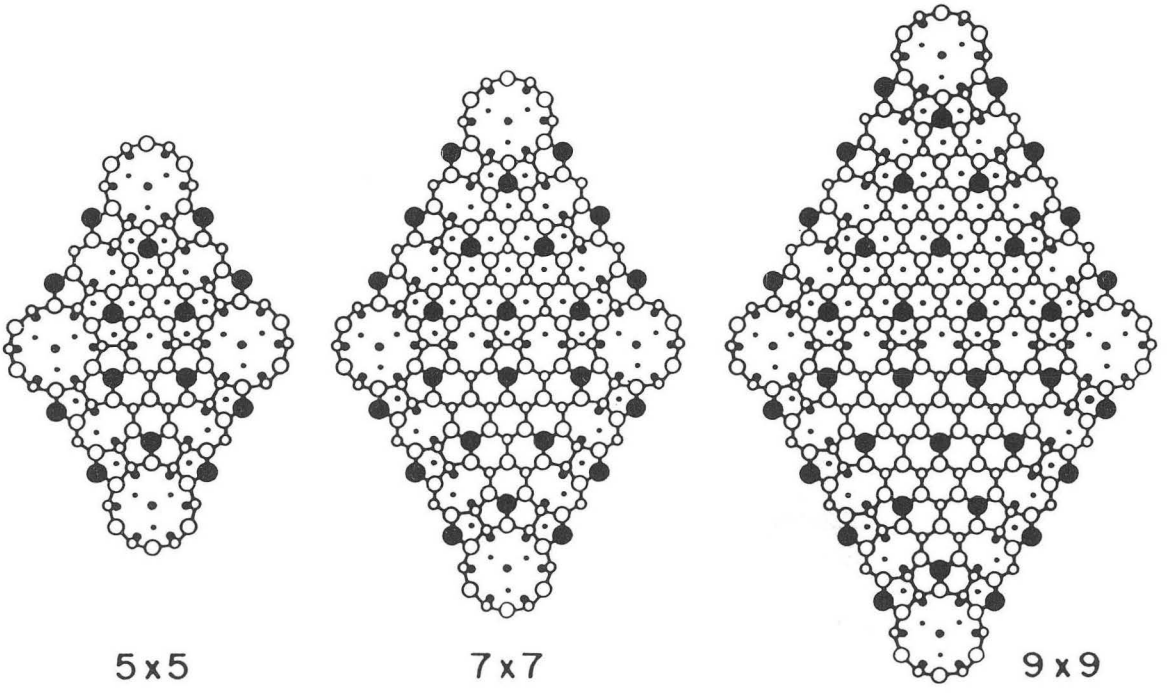


XBL 915-1077

Figure 6

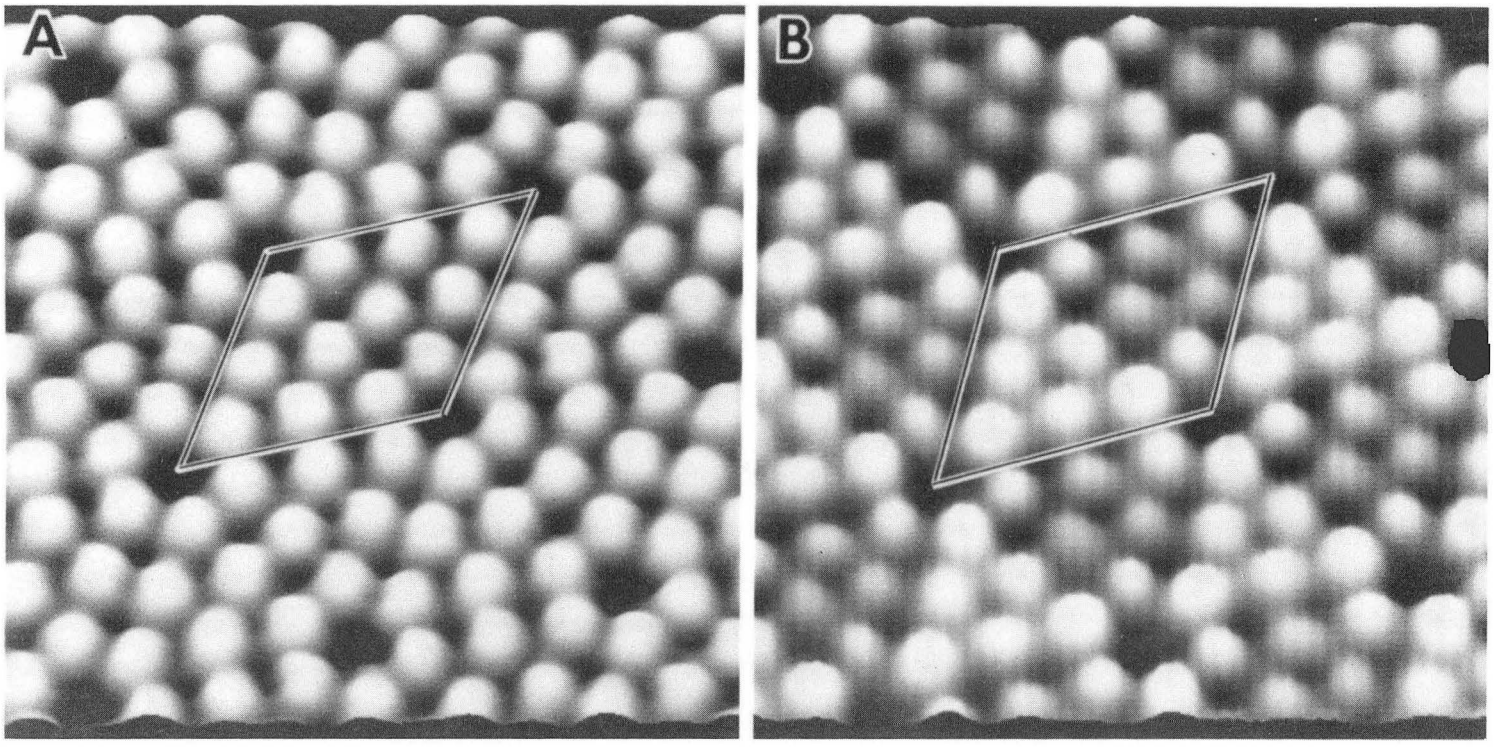


XBB 915-3958

Figure 7

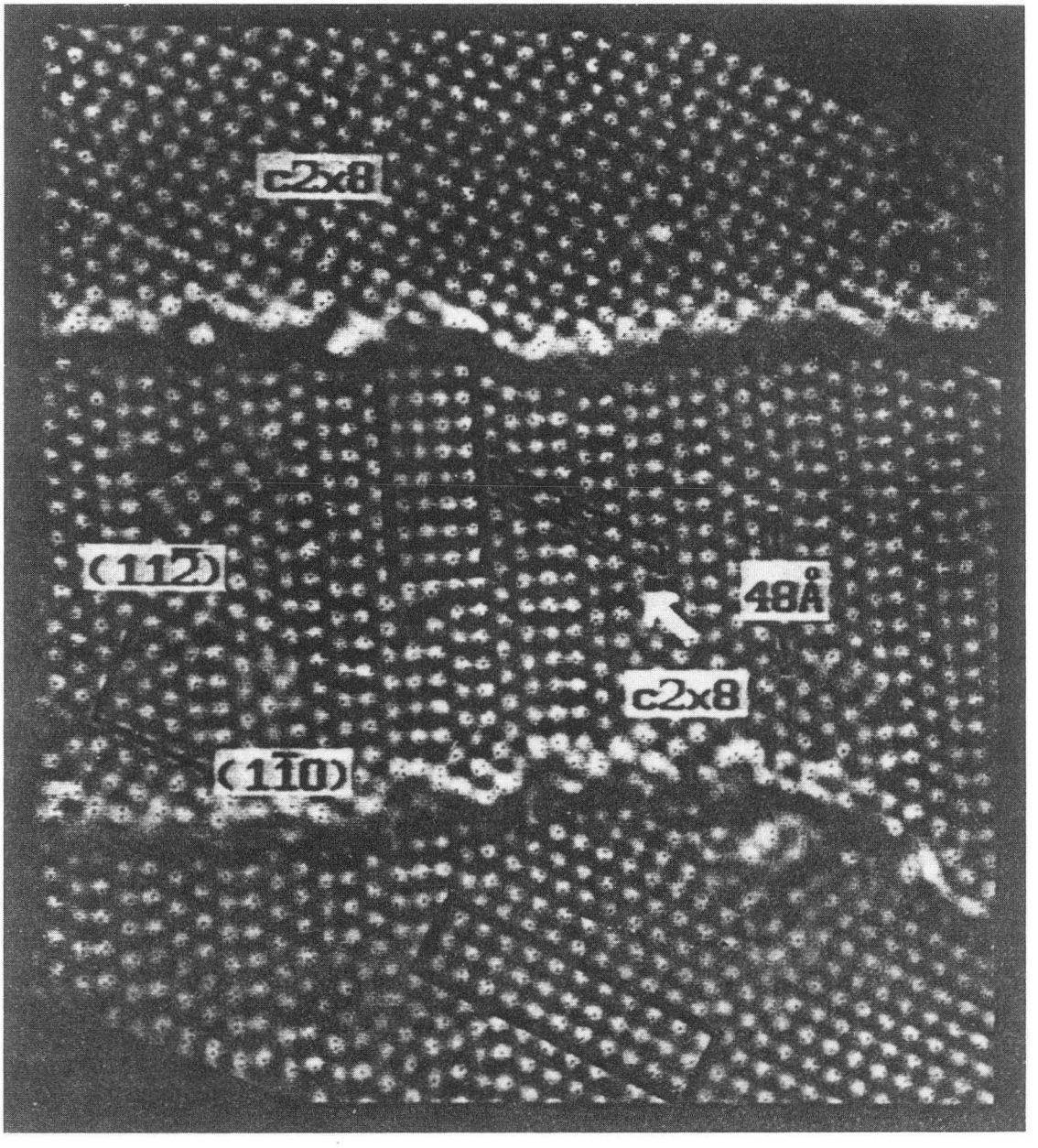


XBB 915-3959

Figure 8

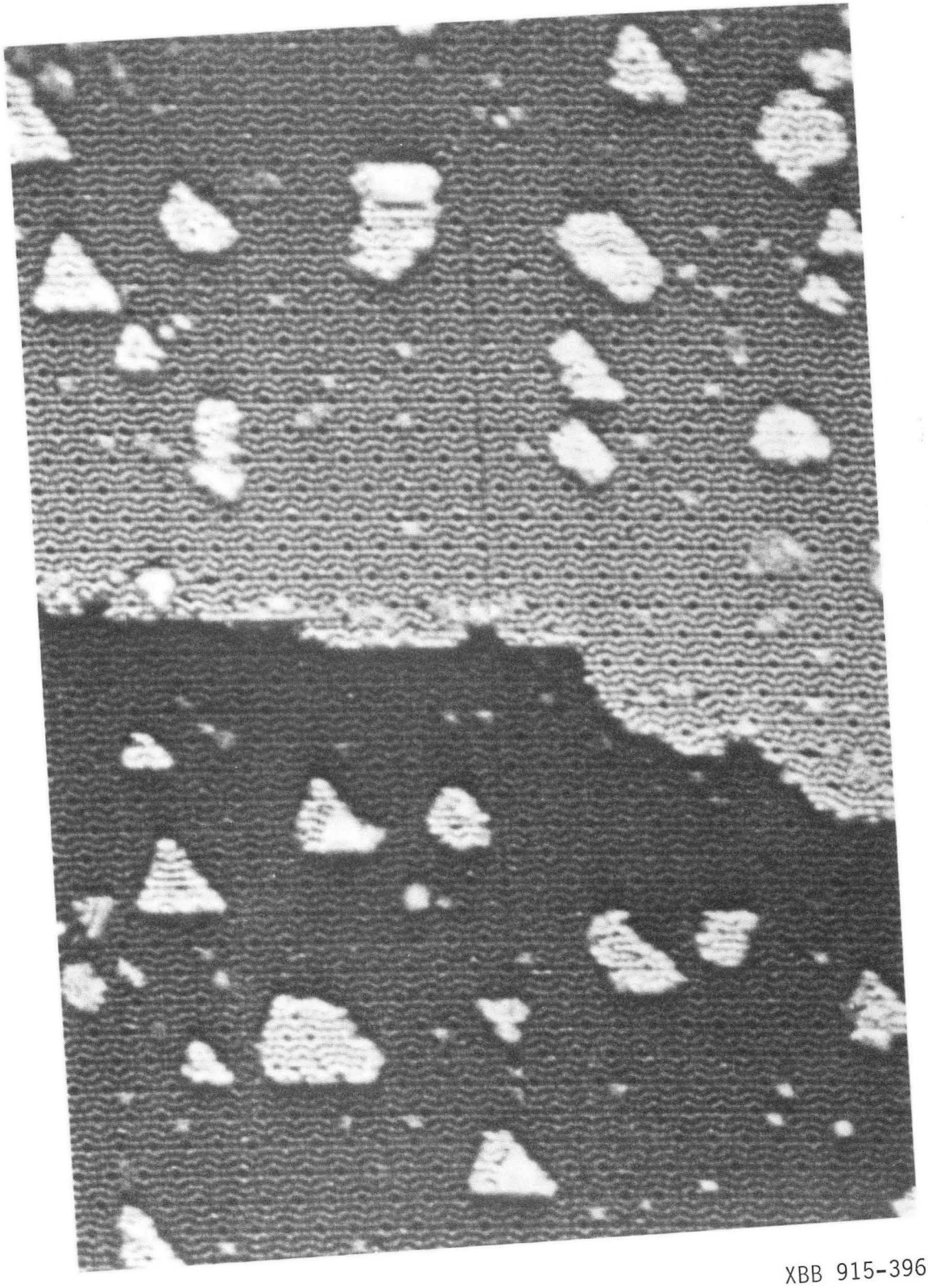

XBB 915-3960

Figure 9

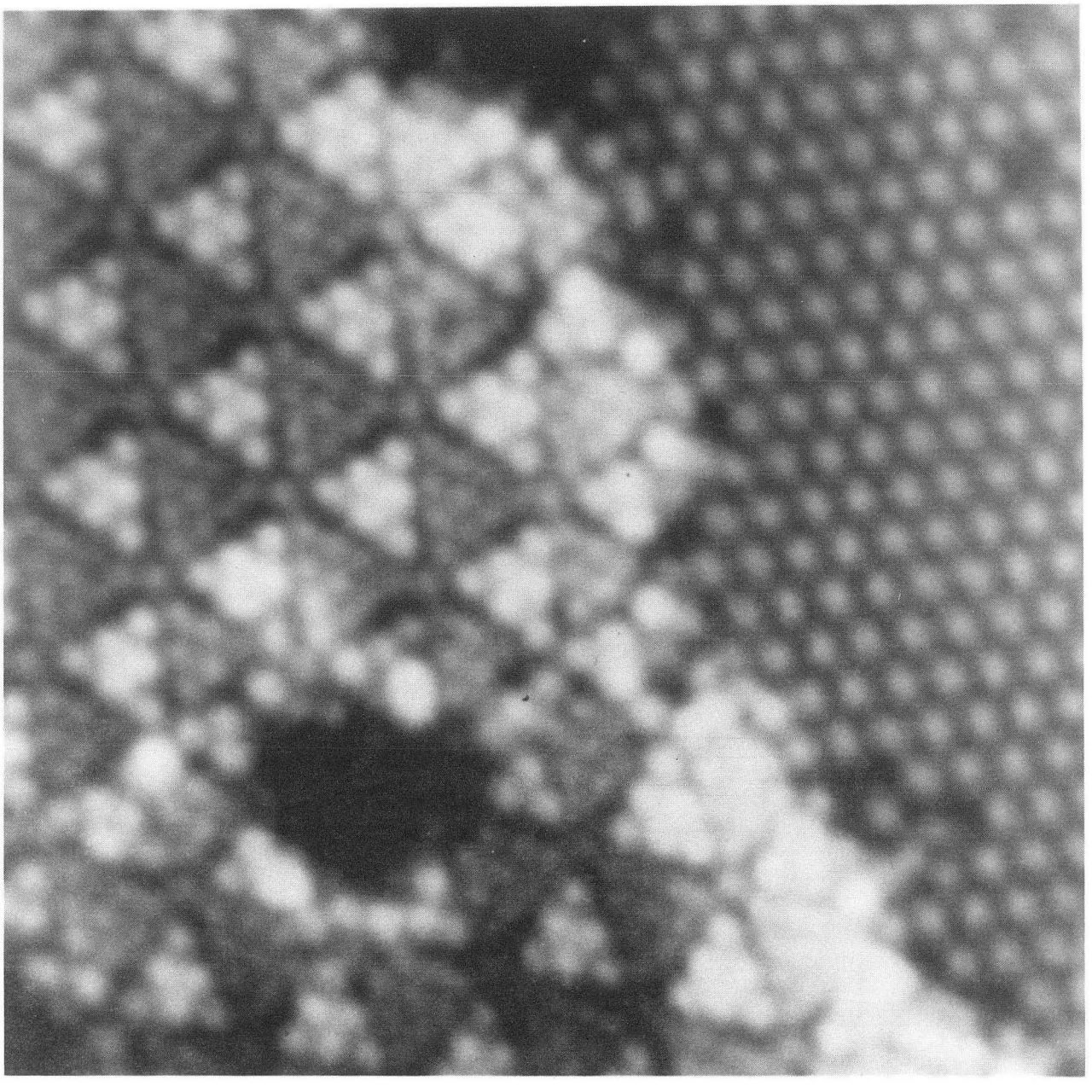

XBB 915-3961

Figure 10

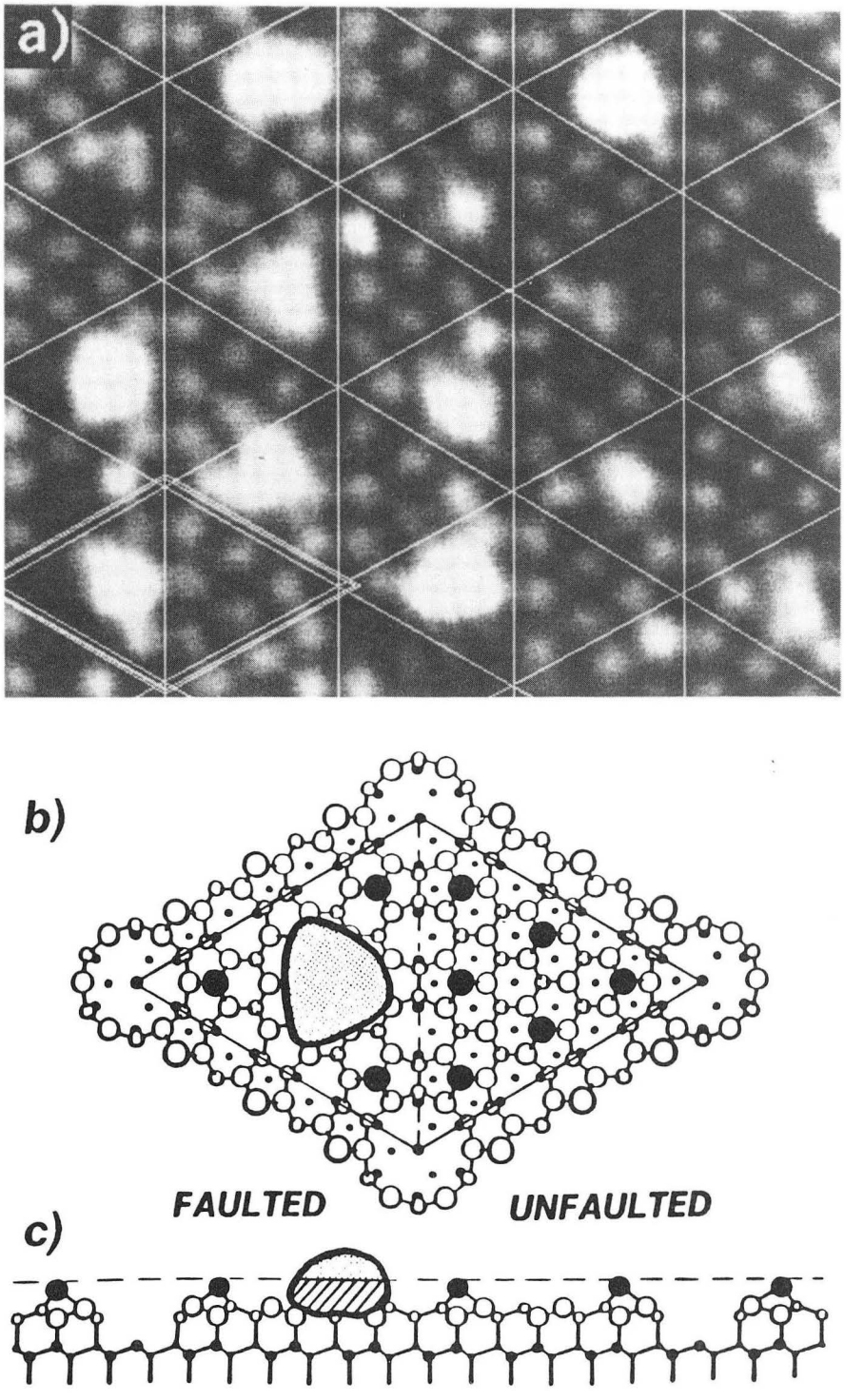


XBB 915-3962

Figure 11

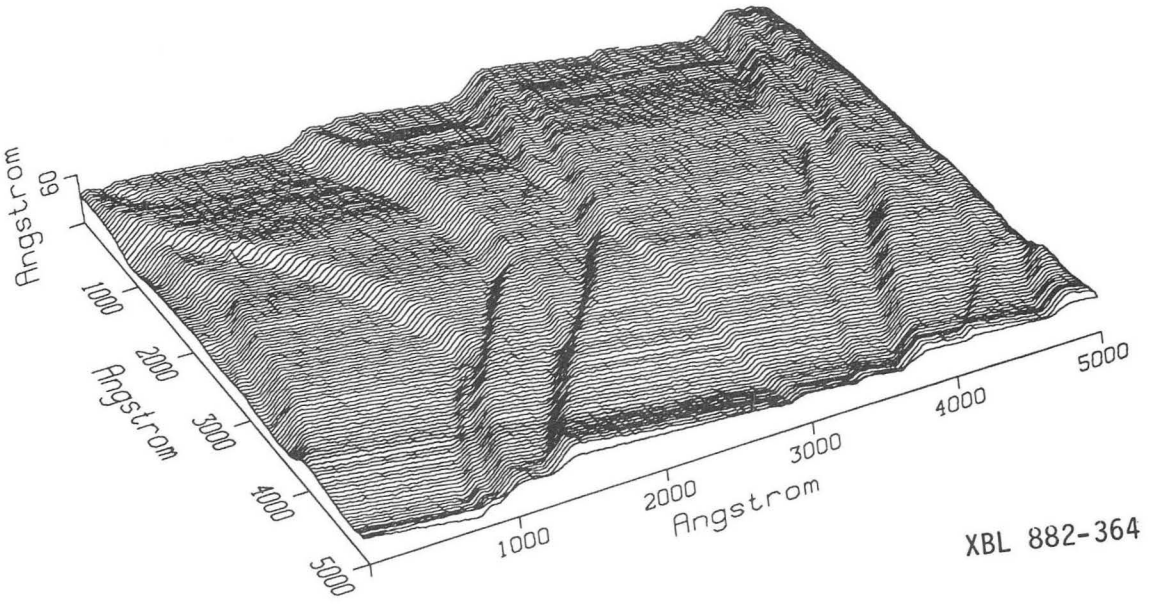
Angstrom
0
1000
2000
3000
4000
5000
Angstrom
1000
2000
3000
4000
5000
Angstrom
XBL 882-364

Figure 12

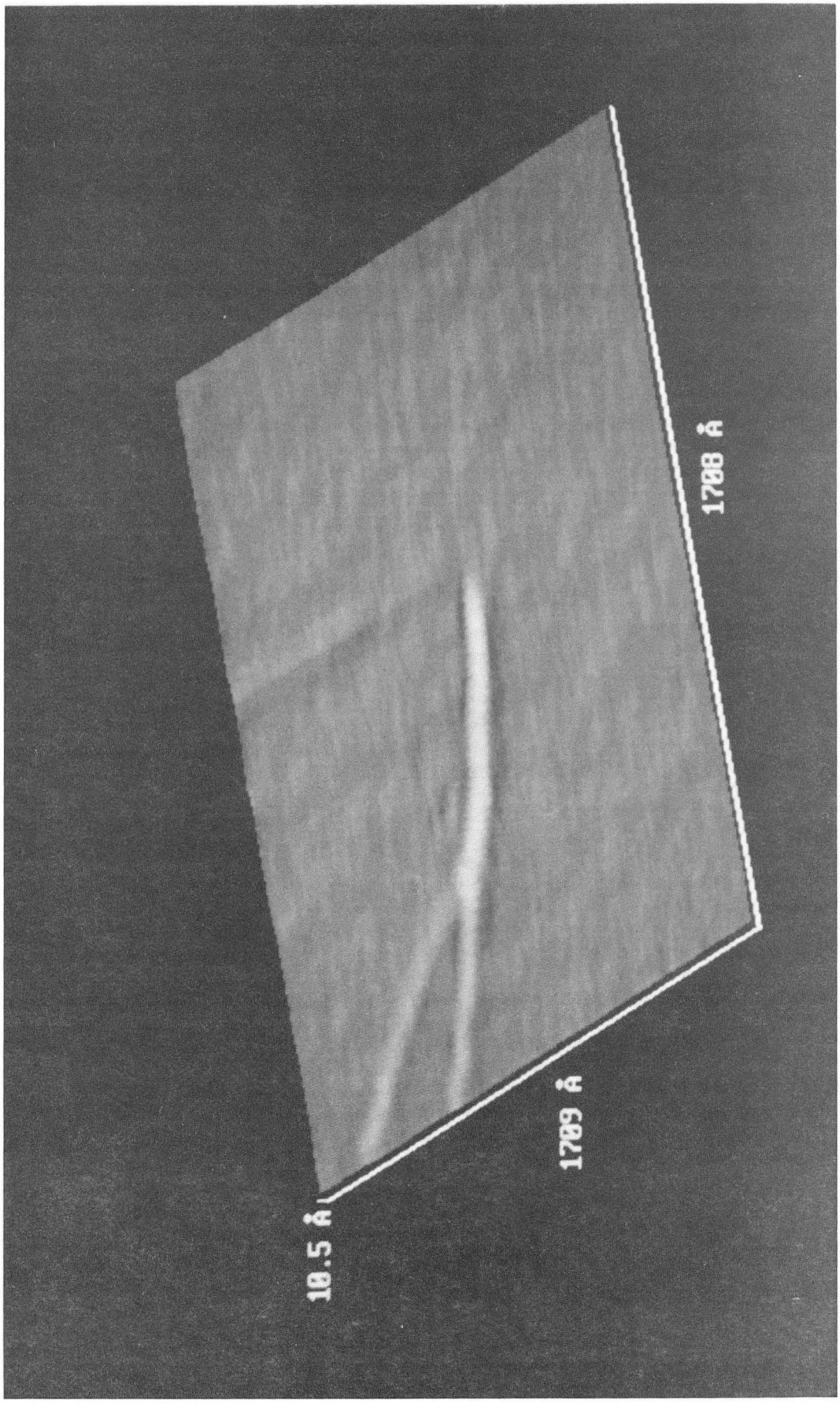


XBB 897 5400

Figure 13

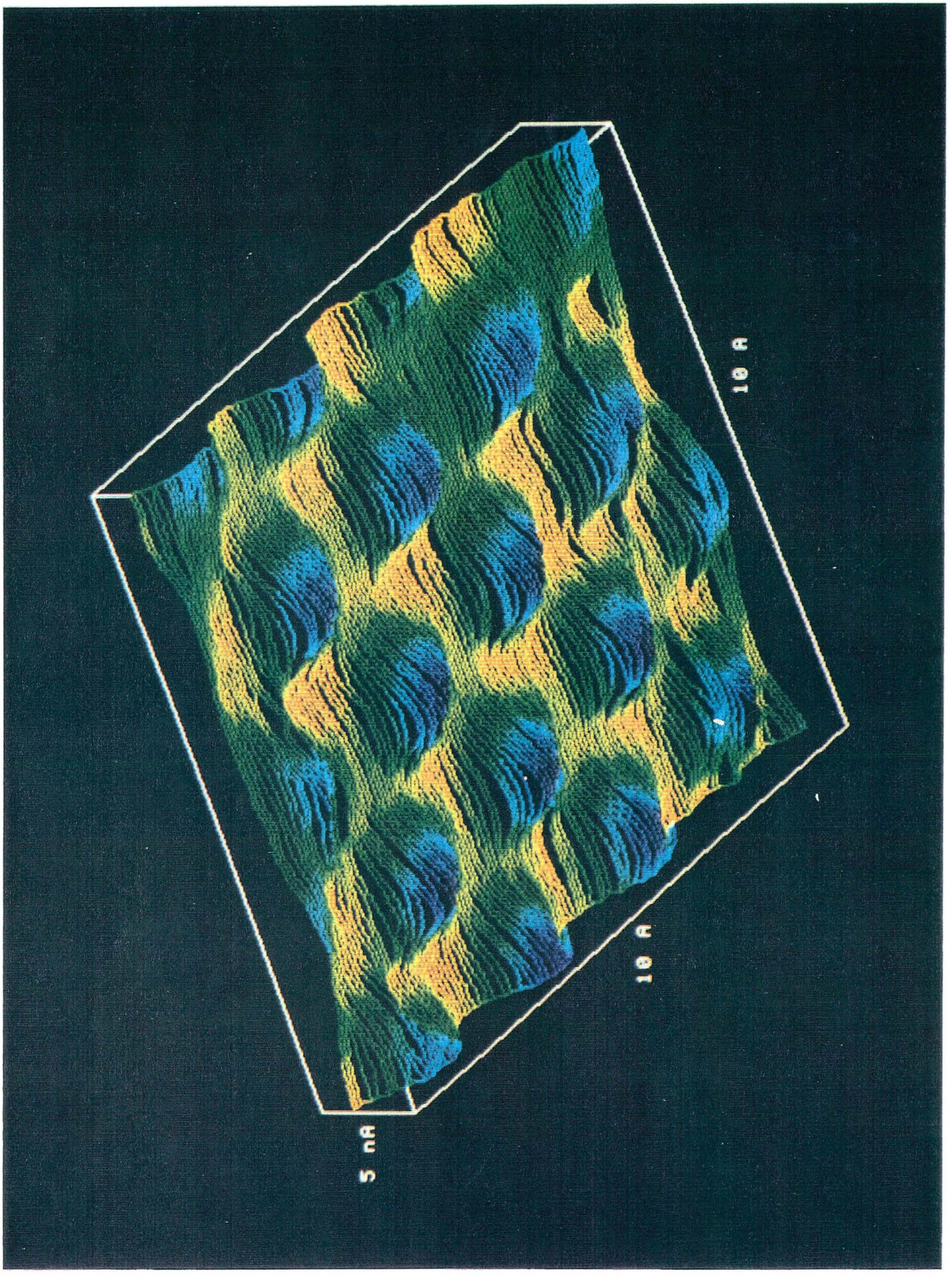


BBC 882-850

Figure 14

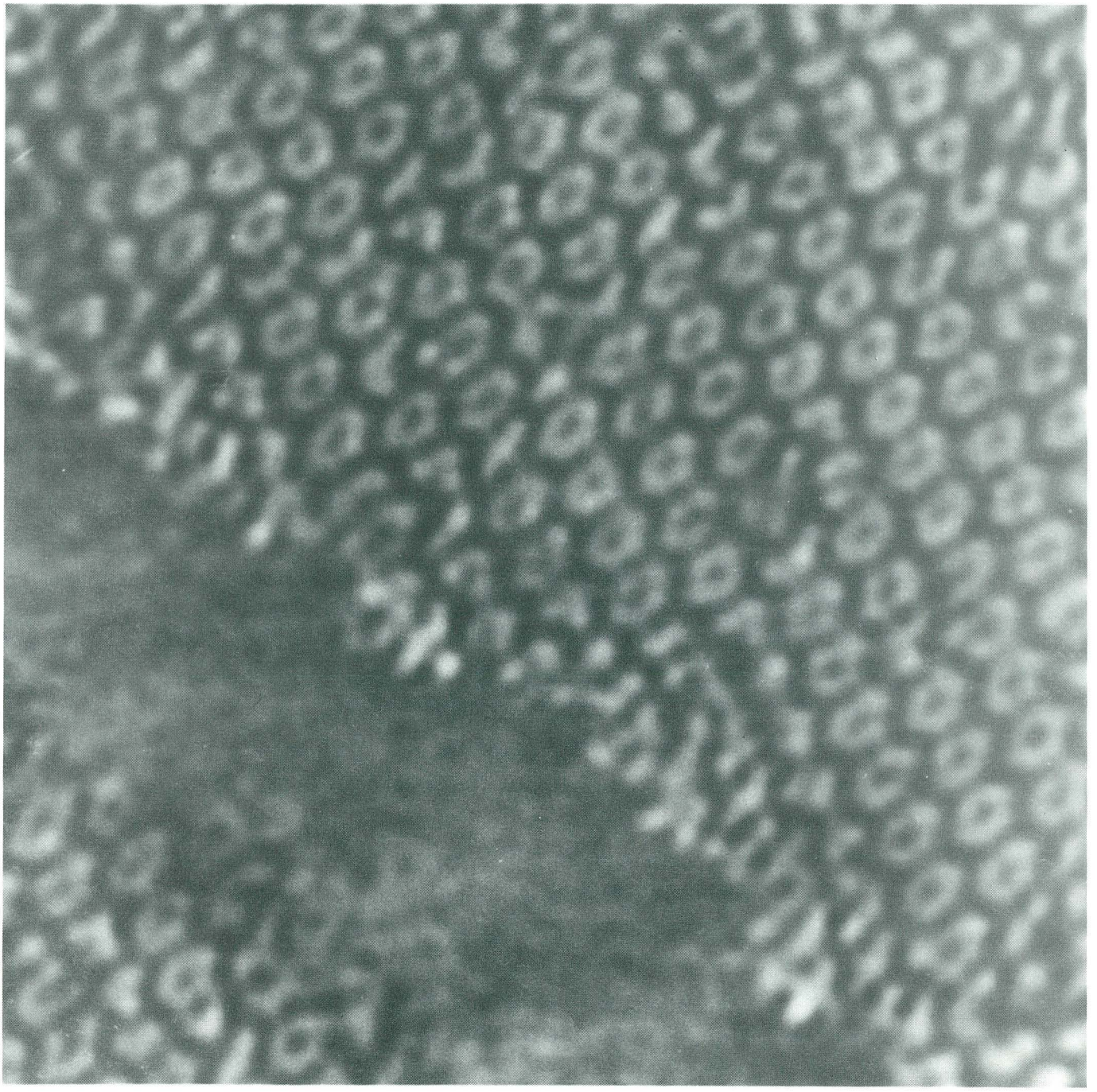

XBB 888-8469

Figure 15a

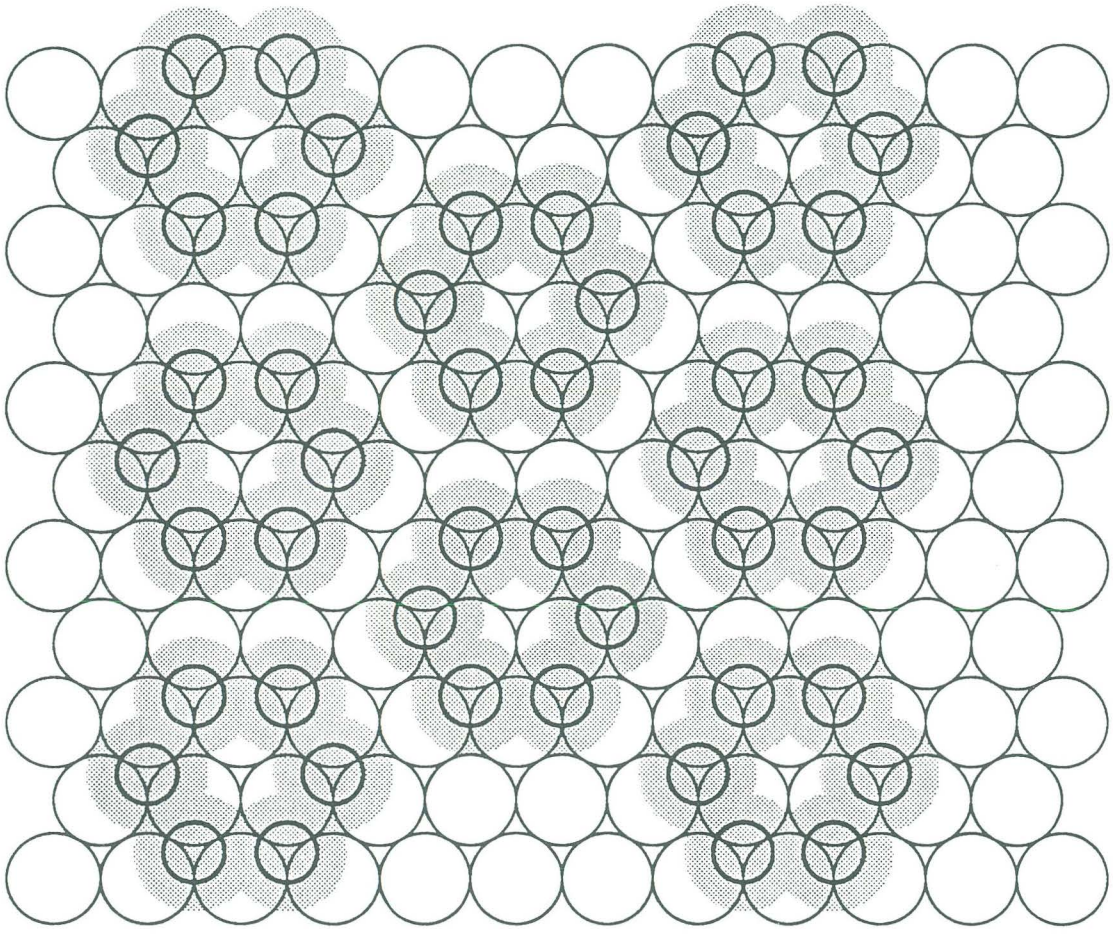

Sulfur $(2\sqrt{3} \times 2\sqrt{3})R30^{\circ}$ on Re(0001)

XBL 907-6447

Figure 15b

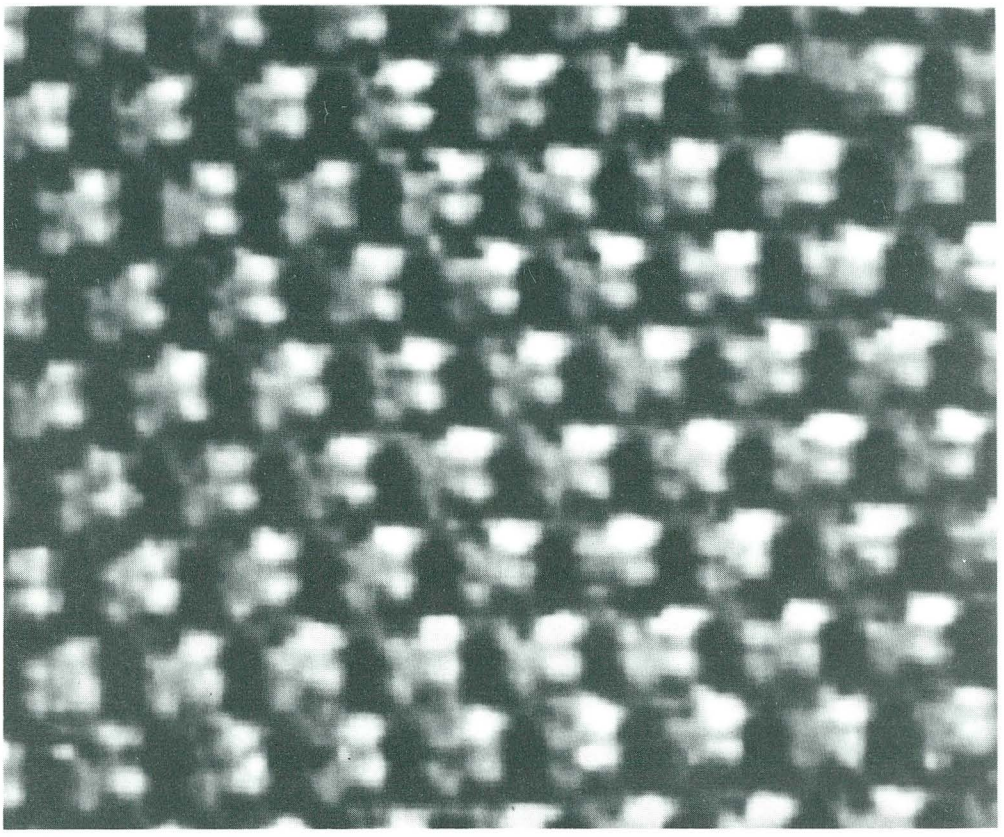

Figure 16a

XBB 907-5508

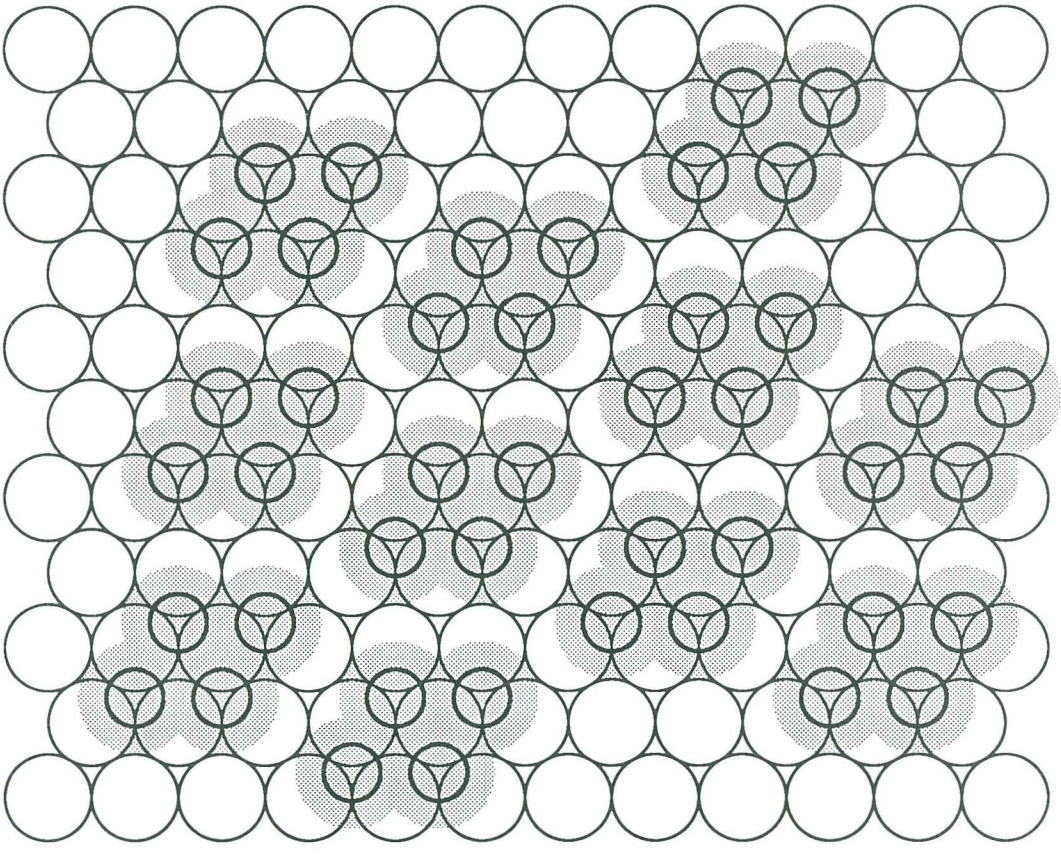


Figure 16b

XBL 907-6446

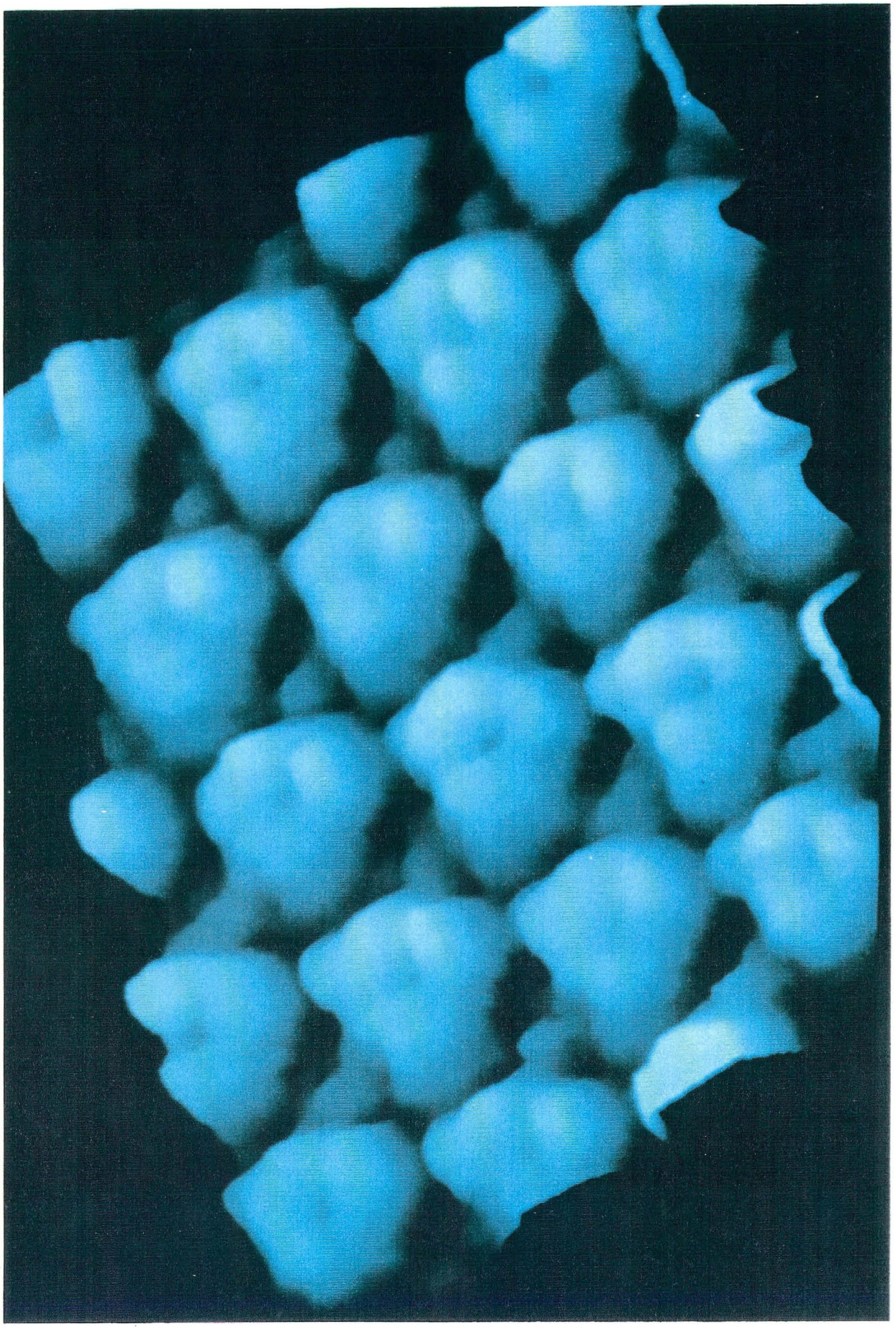

BBC 915-3964

Figure 17a

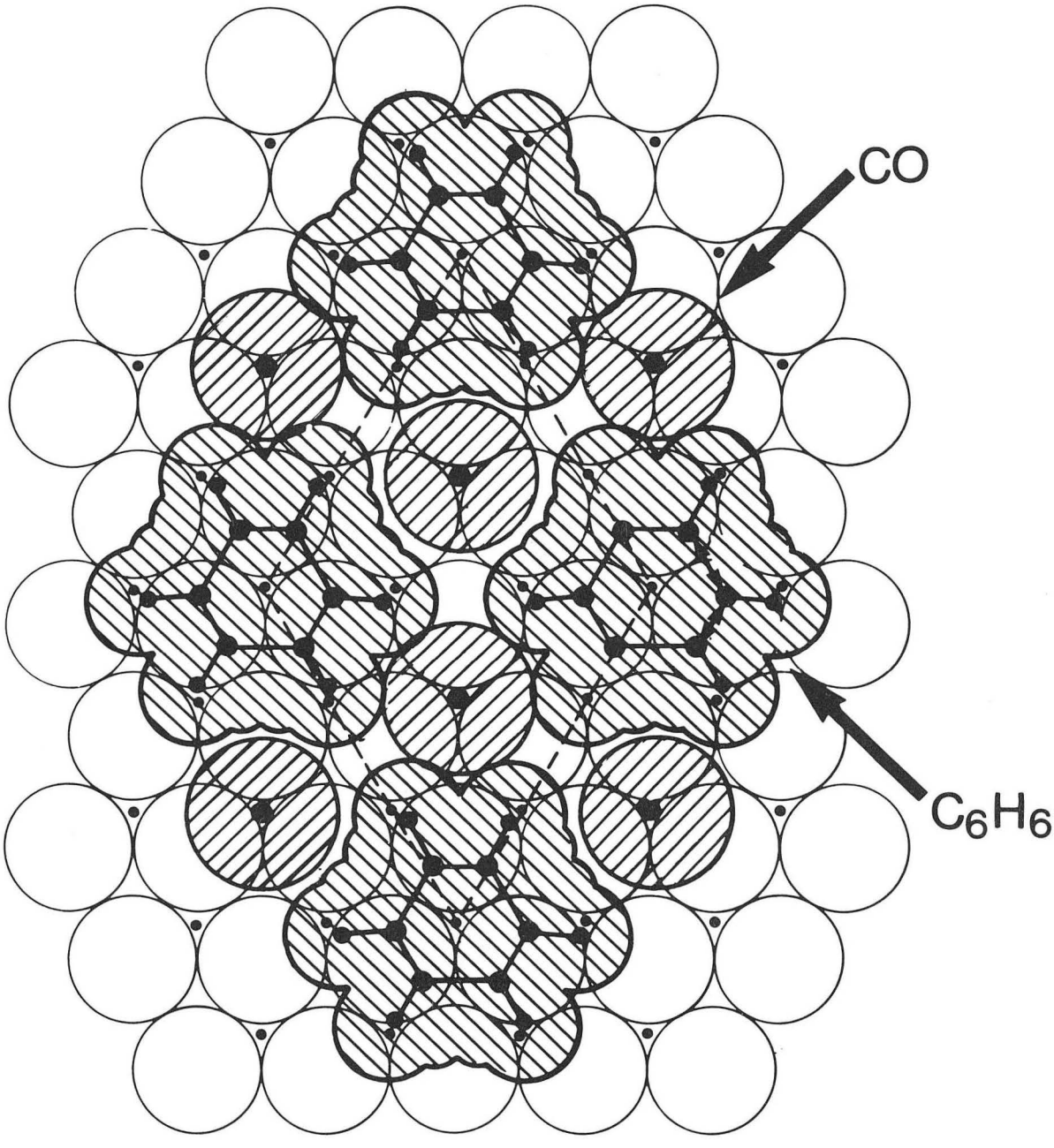


XBL 915-1078

Figure 17b

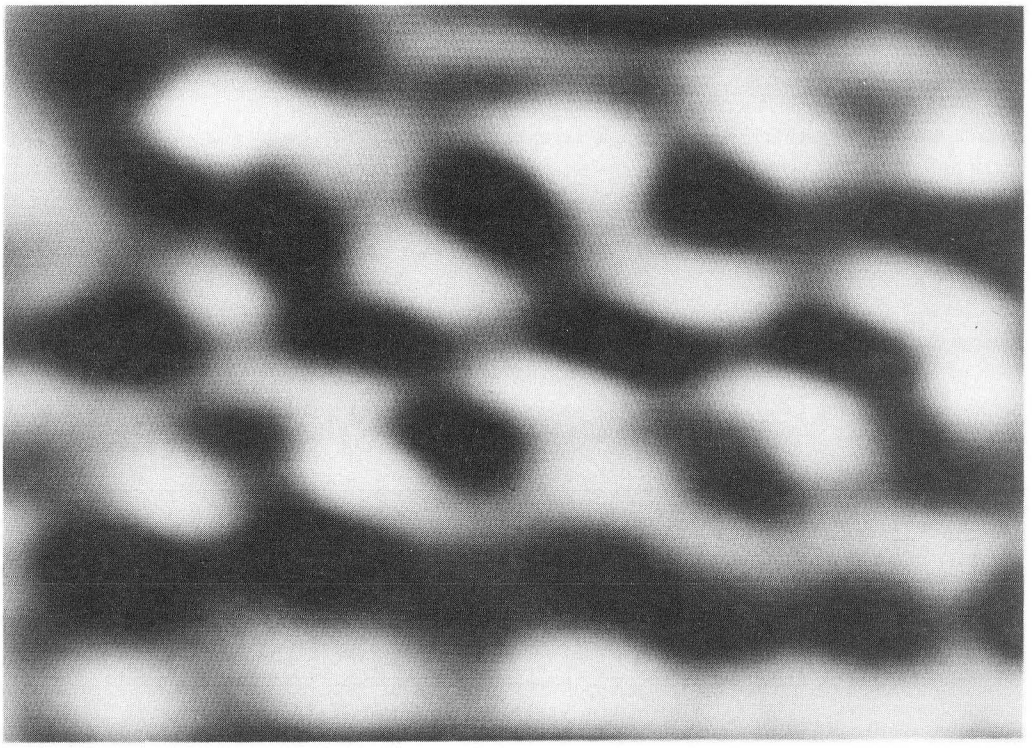

Figure 18 (top)

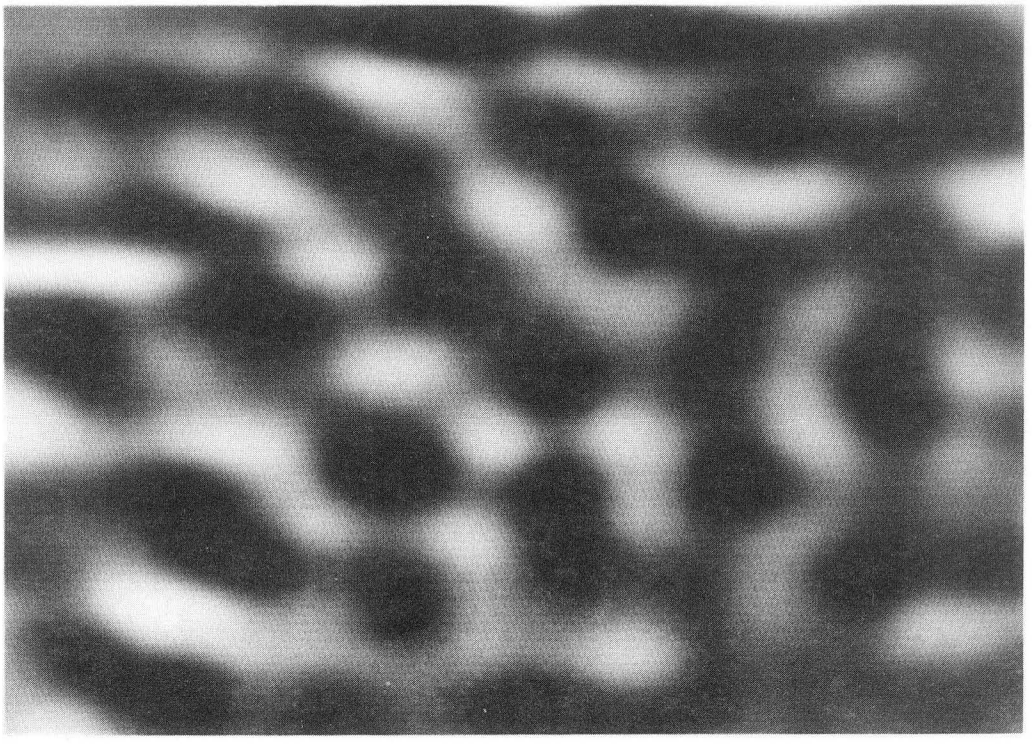

XBB 911-499

Figure 18 (bottom)

XBB 905-3950

Figure 19

*LAWRENCE BERKELEY LABORATORY*
*CENTER FOR ADVANCED MATERIALS*
*1 CYCLOTRON ROAD*
*BERKELEY, CALIFORNIA 94720*